DOCTORAATSPROEFSCHRIFT

2011 | School voor Levenswetenschappen

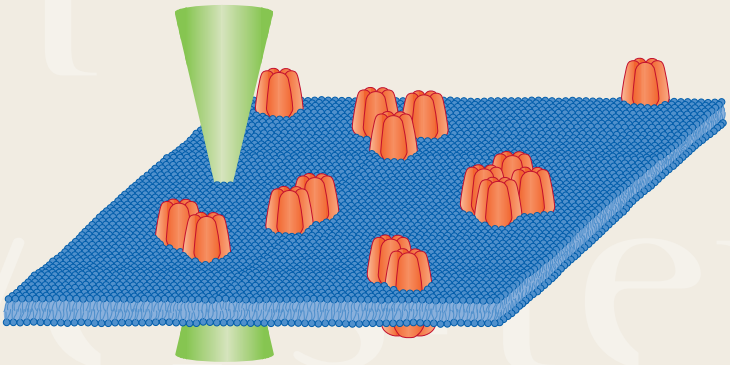

The dynamic behavior of the glycine receptor in the plasma membrane

An exploratory study by ensemble averaging microfluorimetric methods

Proefschrift voorgelegd tot het behalen van de graad van
Doctor in de Biomedische Wetenschappen, te verdedigen door:

Nick SMISDOM

Promotor: prof. dr. Marcel Ameloot
Copromotor: prof. dr. Jean-Michel Rigo

Maastricht University

universiteit hasselt

DOCTORAATSPROEFSCHRIFT

2011 | School voor Levenswetenschappen

The dynamic behavior of the glycine receptor in the plasma membrane

An exploratory study by ensemble averaging microfluorimetric methods

Proefschrift voorgelegd tot het behalen van de graad van
Doctor in de Biomedische Wetenschappen, te verdedigen door:

Nick SMISDOM

Promotor: prof. dr. Marcel Ameloot
Copromotor: prof. dr. Jean-Michel Rigo

Maastricht University

universiteit hasselt

D/2011/2451/30

Institute for the Promotion of Innovation through
Science and Technology in Flanders (IWT-Vlaanderen)

Members of the jury

prof. dr. I. LAMBRICHTS, *Chairman*	*Universiteit Hasselt, Diepenbeek, Belgium*
prof. dr. M. AMELOOT, *promotor*	*Universiteit Hasselt, Diepenbeek, Belgium*
prof. dr. J.-M. RIGO, *copromotor*	*Universiteit Hasselt, Diepenbeek, Belgium*
prof. dr. K. BRAECKMANS	*Universiteit Gent, Gent, Belgium*
prof. dr. B. BRÔNE	*Universiteit Hasselt, Diepenbeek, Belgium*
prof. dr. J. HOFKENS	*Katholieke Universiteit Leuven, Heverlee, Belgium*
prof. dr. N. KAHYA	*Rijksuniversiteit Groningen, Groningen, The Netherlands*
dr. M. VANDEVEN	*Universiteit Hasselt, Diepenbeek, Belgium*
prof. dr. M.A.M.J. van ZANDVOORT	*Universiteit Maastricht, Maastricht, The Netherlands*

Table of Contents

List of Figures

List of Tables

List of abbreviations

2D	two-dimensional
ACF	autocorrelation function
AOM	acousto-optical modulator
CCD	charge-coupled device
CCF	cross-correlation function
CLSM	confocal laser-scanning microscope
CNS	central nervous system
DC	dichroic mirror
DOL	degree of labeling
EMCCD	electron multiplying charge-coupled device
FCS	fluorescence correlation spectroscopy
FD	FITC-labeled dextran
FRAP	fluorescence recovery after photobleaching
GABA	gamma-aminobutyric acid
GDM	generalized disk model
GlyR	glycine receptor
ICS	image correlation spectroscopy
imFCS	imaging fluorescence correlation spectroscopy
ITIR-FCS	imaging total internal reflection fluorescence correlation spectroscopy
NA	numerical aperture
nAChR	nicotinic acetyl-choline receptor
NIF	number of independent fluctuations
PMT	photomultiplier tube
PSF	point-spread function
RICS	raster image correlation spectroscopy
ROI	region of interest
SACF	spatial autocorrelation function
SFCS	scanning fluorescence correlation spectroscopy
STACF	spatiotemporal autocorrelation function
STED	stimulated emission-depletion
TACF	temporal autocorrelation function
TICS	temporal image correlation spectroscopy
TIR	total internal reflection
TIRFM	total internal reflection fluorescence microscopy
TLE	temporal lobe epilepsy
TM	transmembrane domain
UDM	uniform disk model
WT	wild type

1 Introduction

The glycine receptor (GlyR) is present in the vertebral central nervous system (CNS), in the adult mainly in the brainstem and in the spinal cord.[74] It has an important role in fast inhibitory neuronal transmission. Clustering of GlyRs at the postsynaptic membrane is essential to obtain this efficient transmission. The genesis and regulation of this clustering have been subject of scientific research, revealing key players and aspects of the clustering dynamics. The use of fluorescence microscopy to study the receptor in live cells, in real time and at the single molecule level has contributed significantly to the current understanding of the synaptic scaffold.[2] The static model of the synaptic scaffold has gradually been replaced by a dynamic equilibrium between synaptic and extrasynaptic pools of receptors regulated by lateral diffusion in the membrane and transient anchoring by scaffolding molecules.[29]

The glycine receptor is also suggested to be involved in other processes. The GlyR α_3 subtype is involved in vision and processing of acoustic and nociceptive signals. Post-transcriptional processing of GlyR α_3 is associated with pathophysiological aspects of temporal lobe epilepsy (TLE). Two splice variants, GlyR α_3 *L* and *K*, exhibit a differential expression in the hippocampus of TLE patients. Interestingly, both isoforms display also a different clustering behavior: GlyR α_3 *L* is the clustering isoform, while GlyR α_3 *K* displays a diffuse staining. Due to the described relationship between receptor clustering and receptor desensitization kinetics,[70] clustering can modulate receptor functioning. Therefore, investigating the origin of this clustering might reveal a new regulation of signal transduction. The feasibility to study the aggregation and interaction of the receptors using ensemble microfluorimetric techniques is explored and results are compared with current literature.

1.1 Glycine receptor

The glycine receptor (GlyR) is together with the gamma-aminobutyric acid (GABA) receptor type A ($GABA_AR$) and type C ($GABA_CR$) responsible for mediating fast inhibitory neurotransmission in the mature central nervous system (CNS).[127] Those anion-permeable receptors belong to the Cys-loop family of ligand-gated ion channels. This is a group of structurally and functionally related ion channels responsible for fast synaptic transmission in the CNS. They all have a conserved 15-amino acid-spaced disulfide loop in their extracellular ligand-binding domain.[16] Other members of this family in mammals include the nicotinic acetyl-choline receptor (nAChR) and the cation-permeable serotonin type-3 receptor ($5\text{-}HT_3R$).

The architecture of the glycine receptor is discussed prior to the current view of receptor regulation in the membrane of living cells. A detailed discussion of GlyR's pharmacology and distribution throughout the CNS can be found elsewhere.[74,75,127]

1.1.1 Glycine receptor subunit stoichiometry

A functional GlyR comprises five subunits, as do the other members of the cys-loop family. Two classes of GlyR subunits exist: the α and β subunits. These α and β subunits, with a molecular mass of respectively 48 kDa and 58 kDa, share a 47% amino acid sequence homology.[40,41] The α subunits can be further subdivided into four types, ranging from α_1 to α_4, displaying an amino acid sequence homology between 80% and 90%.[1,40,66,79] In contrast to mice, humans lack the α_4 subunit because the human GlyR α_4 gene *GLRA4* is demonstrated to be a pseudo-gene.[114]

Each subunit comprises 4 transmembrane α helices and a large N-terminal extracellular domain holding the glycine binding pocket (*Figure 1.1*). This domain also holds the characteristic Cys-loop. The main difference between α and β subunits is the intracellular loop between TM 3 and TM 4.

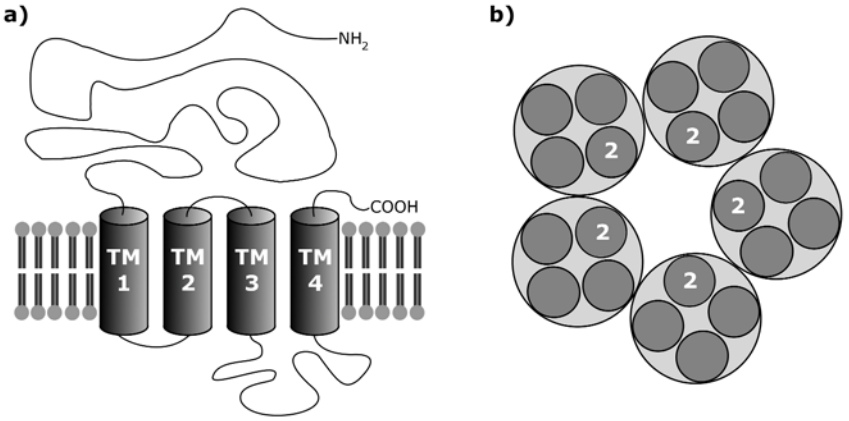

Figure 1.1: Schematic representation of the glycine receptor structure

(a) *General structure of a GlyR subunit showing the four transmembrane α helices and the large N-terminal domain holding the glycine binding pocket and the characteristic Cys-loop. Only in the β subunit, the large cytoplasmic loop between TM3 and TM4 holds the binding domain for gephryin which is responsible for the clustering of the receptor at the postsynaptic membrane. (b) A functional GlyR comprises five subunits, with TM2 of each subunit lining the pore.*

All α subunits have been shown, at least in heterologous expression systems, to form functional homomers.[75] Again in heterologous expression systems, it is also probable that all α subunits are capable of forming heteromers with other α subunits.[67,75] For their native counterparts, the lack of sufficient electrophysiological discriminatory capacity between the α subunits prohibits the identification of GlyRs composed of solely α subunits as homomers or heteromers.[75] The β subunit, in contrast, does not form homomeric functional GlyRs.[11] Moreover, defined amino acids in the highly conserved N-terminal regions prevent the homomeric assembly of β subunits at all.[42]

Although β subunits are unable to assemble into pentameric homomers, they can form heteromers with α subunits.[69,88,99] Furthermore, the $\alpha_1\beta$ hetero-pentamer is the most abundant GlyR in adults. αβ heteromers can be readily discriminated from α homomers since introduction of the β subunit leads to a reduced picrotoxin sensitivity and to a change in single channel conductance.[99] The β subunit modulates ligand binding in general.[43] The subunit stoichiometry of αβ hetero-pentamer is assumed to be 2α:3β arranged as β-α-β-α-β, but irrefutable evidence is lacking.[43,75]

1.1.2 Glycine receptor clustering

The bulk of glycinergic inhibitory transmission in the adult CNS is most likely mediated by heteromeric GlyRs $\alpha_1\beta$.[75] These GlyRs are clustered in the post-synaptic membrane to achieve a fast and efficient signal transduction. A developmental switch from α_2 homomeric GlyRs to heteromeric GlyRs $\alpha_1\beta$ between birth and the third postnatal week is revealed by mRNA and protein expression levels in rat.[6,77,126] This developmental switch has also been confirmed using electrophysiological techniques.[68,78,120]

The developmental switch implicates a mechanism that gives rise to the final post-synaptic clusters. One hypothesis involves GlyR α_2. The strong expression of GlyR α_2 together with the high intracellular chloride concentration of embryonic neurons have funded the hypothesis of an excitatory role for the GlyR α_2 during CNS development.[35,105] Under these conditions, binding of taurine to GlyR α_2 will lead to a depolarizing chloride efflux that might stimulate calcium influx that on its turn is required for the development of numerous neuronal specializations, including glycinergic synapses.[35,58]

In addition to their genesis, even more efforts are put in the understanding of the maintenance and regulation of mature clusters. A key actor in this clustering is gephyrin, a cytoplasmic anchoring protein of 98 kDa. Gephyrin is essential in GlyR clustering at synapses and acts only through interaction with the TM3-TM4 loop of the β subunit.[7,36,55,56,83] Consequently, GlyRs at mature synapses have to be $\alpha\beta$ heteromers. Recently, it has been demonstrated that gephyrin itself is tethered to the plasma via collybistin.[101] This complex on its turn is initiated through interaction with neuroligin-2.[98]

It has long been thought that synapses were regulated through cycling of receptor clusters between the plasma membrane and intracellular compartments. The interaction at the post-synaptic membrane between gephyrin, collybistin and neuroligin-2 indicates the complexity of the synapse and the regulation of its constitution. Furthermore, lateral diffusion properties modulate the regulation of GlyRs in response to change in neuronal activity.

Therefore, the new emerging view incorporates a dynamic regulation of the neurotransmitter receptor density at postsynaptic densities. Surface trafficking plays an important role in this diffusion-trapping model.[71] It enables a rapid

exchange between intra- and extrasynaptic compartments with transient stabilization of the receptor at synapses by interaction with the scaffold proteins.[2]

1.1.3 Glycine receptor α_3

The GlyR α_3 subunit is expressed to a lesser extent than the abundant GlyR α_1 subunit.[77] Nevertheless, this receptor isoform is found to participate in important functions like vision and inner ear signal transduction.[27,46] Furthermore, it has been shown that GlyR α_3 is also involved in spinal nociceptive signaling, more specifically in pain sensitization.[45]

GlyR α_3 is also expressed in the hippocampus, where post-transcriptional processing of its gene *GLRA3* transcript is associated with pathophysiological aspects of temporal lobe epilepsy (TLE).[30] The role of alternative splicing of the *GLRA3* transcript, giving rise to GlyR α_3 *L* and GlyR α_3 *K*, in TLE has also been investigated.[31] GlyR α_3 *L* comprises a large cytoplasmic loop between TM3 and TM4 with 15 amino acids extra compared to the smaller TM3-TM4 loop of GlyR α_3 *K* (*Figure 1.2*).[87] The longest splice variant has also significant slower receptor desensitization kinetics.[87]

In healthy people, GlyR α_3 *L* is the predominant variant.[31] In the hippocampus, most of them are located extra-synaptically. The small fraction that resides in a synapse are preferentially located at glutamatergic nerve endings.[31] In patients suffering from severe TLE, in contrast, GlyR α_3 *K* is upregulated at the expense of GlyR α_3 *L*.[31]

Interestingly, a remarkable difference exists between both splice variants concerning their aggregation state. While extra-synaptic GlyR α_3 *K* exhibits a diffuse distribution, distinct clusters are formed by its longer counterpart.[31] Moreover, evidence supports a gephyrin-independent cluster mechanism.[31] Due to the described relationship between receptor clustering and receptor desensitization kinetics,[70] clustering can modulate receptor functioning. Therefore, investigating the origin of this clustering might reveal a new regulation of signal transduction.

```
GlyR α3L MAHVRHFRTLVSGFYFWEAALLLSLVATKETDSAR--------------SRSAPMSPSDF 46
GlyR α3K MAHVRHFRTLVSGFYFWEAALLLSLVATKETDSAR--------------SRSAPMSPSDF 46
GlyR α1  ---MYSFNTL--RLYLWETIVFFSLAASKEAEAAR--------------SAPKPMSPSDF 41
GlyR β   MKFLLTTAFLI-LISLWVEEAYSKEKSSKKGKGKKKQYLCPSQQSAEDLARVPANSTSNI 59
            :     *   : :*       .  ::*: .. :                :   . *.*::

GlyR α3L LDKLMGRTSGYDARIRPNFKGPPVNVTCNIFINSFGSIAETTMDYRVNIFLRQKWNDPRL 106
GlyR α3K LDKLMGRTSGYDARIRPNFKGPPVNVTCNIFINSFGSIAETTMDYRVNIFLRQKWNDPRL 106
GlyR α1  LDKLMGRTSGYDARIRPNFKGPPVNVSCNIFINSFGSIAETTMDYRVNIFLRQQWNDPRL 101
GlyR β   LNRLL---VSYDPRIRPNFKGIPVDVVVNIFINSFGSIQETTMDYRVNIFLRQKWNDPRL 116
         *::*:    .**.******** **:*  ********** **************:******

GlyR α3L AY-SEYPD-DSLDLDPSMLDSIWKPDLFFANEKGANFHEVTTDNKLLRIFKNGNVLYSIR 164
GlyR α3K AY-SEYPD-DSLDLDPSMLDSIWKPDLFFANEKGANFHEVTTDNKLLRIFKNGNVLYSIR 164
GlyR α1  AY-NEYPD-DSLDLDPSMLDSIWKPDLFFANEKGAHFHEITTDNKLLRISRNGNVLYSIR 159
GlyR β   KLPSDFRGSDALTVDPTMYKCLWKPDLFFANEKSANFHDVTQENILLFIFRDGDVLVSMR 176
            .::  . *:* :**:*  ..:***********.*:**::* :* ** * ::*:** *:*
                 Cys-loop
GlyR α3L LTLTLSCPMDLKNFPMDVQTCIMQLESFGYTMNDLIFEWQDEAPVQVAEGLTLPQFLLKE 224
GlyR α3K LTLTLSCPMDLKNFPMDVQTCIMQLESFGYTMNDLIFEWQDEAPVQVAEGLTLPQFLLKE 224
GlyR α1  ITLTLACPMDLKNFPMDVQTCIMQLESFGYTMNDLIFEWQEQGAVQVADGLTLPQFILKE 219
GlyR β   LSITLSCPLDLTLFPMDTQRCKMQLESFGYTTDDLRFIWQSGDPVQL-EKIALPQFDIKK 235
         :::**:**:**. ****.* * ********* :** * **.  .**: : ::**** :*:
                                                  TM1
GlyR α3L EK-DLRYCTKHYN-TGKFTCIEVRFHLERQMGYYLIQMYIPSLLIVILSWVSFWINMDAA 282
GlyR α3K EK-DLRYCTKHYN-TGKFTCIEVRFHLERQMGYYLIQMYIPSLLIVILSWVSFWINMDAA 282
GlyR α1  EK-DLRYCTKHYN-TGKFTCIEARFHLERQMGYYLIQMYIPSLLIVILSWISFWINMDAA 277
GlyR β   EDIEYGNCTKYYKGTGYYTCVEVIFTLRRQVGFYMMGVYAPTLLIVVLSWLSFWINPDAS 295
         *. :   ***:*: ** :**:*. * *.**:*:*:: :* *:****:***:***** **:
                TM2                                TM3
GlyR α3L PARVALGITTVLTMTTQSSGSRASLPKVSYVKAIDIWMAVCLLFVFSALLEYAAVNFVSR 342
GlyR α3K PARVALGITTVLTMTTQSSGSRASLPKVSYVKAIDIWMAVCLLFVFSALLEYAAVNFVSR 342
GlyR α1  PARVGLGITTVLTMTTQSSGSRASLPKVSYVKAIDIWMAVCLLFVFSALLEYAAVNFVSR 337
GlyR β   AARVPLGIFSVLSLASECTTLAAELPKVSYVKALDVWLIACLLFGFASLVEYAVVQVMLN 355
         .*** *** :**:::::.:   *.*********:*:*: .**** *::*:***.*:.: .
                                                  difference L and K
GlyR α3L QHKELLRFR-----------------RKRKNK---------TEAFALEKFYRFSDMDDEV 376
GlyR α3K QHKELLRFR-----------------RKRKNK-------------------------DDEV 361
GlyR α1  QHKELLRFR-----------------RKRRHH---------KSPM-LNLF-----QEDEA 365
GlyR β   NPKRVEAEKARIAKAEQADGKGGNVAKKNTVNGTGTPVHISTLQVGETRCKKVCTSKSDL 415
         : *.:   :                  :*.  :                      ..:

GlyR α3L RESRFSF----------TAYGMGP-CLQAKDGMTPKGPN-----HPVQVMPKSPDEMRKV 420
GlyR α3K RESRFSF----------TAYGMGP-CLQAKDGMTPKGPN-----HPVQVMPKSPDEMRKV 405
GlyR α1  GEGRFNF----------SAYGMGPACLQAKDGISVKGANNSNTTNPPPAPSKSPEEMRKL 415
GlyR β   RSNDFSIVGSLPRDFELSNYDCYGKPIEVNNGLGKSQAKNN----------KKPPPAKPV 465
          .. *.:          : *.     ::.::*:  . .:           *.*   : :
                                TM4
GlyR α3L FIDRAKKIDTISRACFPLAFLIFNIFYWVIYKILRHEDIHQQQD 464
GlyR α3K FIDRAKKIDTISRACFPLAFLIFNIFYWVIYKILRHEDIHQQQD 449
GlyR α1  FIQRAKKIDKISRIGFPMAFLIFNMFYWIIYKIVRREDVHNQ-- 457
GlyR β   IPTAAKRIDLYARALFPFCFLFFNVIYWSIYL---------- 497
         :   **:**  :*  **:.**:**::** **
```

Figure 1.2: Multiple sequence alignment of selected GlyR subunits

The primary protein structures of four GlyR subunits are compared, comprising GlyR α_3 L (NP_006520), GlyR α_3 K (NP_001036008), GlyR α_1 (NP_001139512), and GlyR β (NP_000815). These sequences were aligned using ClustalW.[18] Stars (*) indicate identical amino acids, colons (:) indicate conserved amino acids and points (.) indicate semi-conserved amino acids. The 15 amino acid difference between the GlyR α3 splice variants is indicated by the red box. The sequence of the β subunit that holds the interaction site with gephyrin is highlighted in green. Transmembrane domains are marked by blue boxes while the characteristic Cys-loop is marked by a yellow box.

1.2 Principles of fluorescence and fluorescence microscopy

Many fields in biology including cell biology, genetics, and immunology – just to name but a few – have benefited from the use of fluorescence and still rely heavily on its use. The growing amount of applications throughout the last 70 years underpins the added value that fluorescence can offer to biology. Also the instrumental developments and new approaches have been crucial in bringing the fluorescence applications to a new level. In this respect, the first time that a fluorochrome, i.e. a fluorescent probe, was coupled to a biological antibody in 1941 is an important milestone in the history of fluorescence microscopy.[20,123] The resulting fluorescently labeled antibody combines the advantages of fluorescence with the specificity and sensitivity of a selected, biological antibody. The wide-spread use of fluorescently labeled antibodies nowadays highlights the success of this strategy.

Many other strategies to label a specific component exist, but prior to further elaboration on this aspect, the basics of fluorescence are explained.

1.2.1 Light: visible electromagnetic radiation

Electromagnetic radiation is formed by waves with electric and magnetic field components orthogonal to the direction of propagation and also orthogonal to each other. Each wave of the electromagnetic spectrum has its own unique wavelength (λ, nm) and frequency (ν, Hz). The broad spectrum includes amongst others frequencies used for radio transmission, mobile phone communication, wireless internet, microwaves and X-rays. A small band of this spectrum can be detected by the human eye. This band is called visible light and ranges from about 400 nm (blue; $1nm = 10^{-9}\,m$) to 700 nm (red). A rainbow is a good representation of this small range, going from blue, over green and yellow to red.

Irrespective of their origin and use, all electromagnetic waves travel at the speed of light ($c = 2.99792 \times 10^{8}\ m/s$ in vacuum), yielding the relationship:[138]

$$c = \lambda \nu \qquad (1.1)$$

Electromagnetic radiation has both wave and particle properties. The particle characteristic of electromagnetic radiation allows one to consider it as particles carrying discrete amounts of energy but no mass. For visible light, these energy quanta are called photons.[139] The energy that they hold increases with decreasing wavelength:

$$E = h\nu = h\frac{c}{\lambda} \tag{1.2}$$

where $h = 6.62618 \times 10^{-34}\, J \cdot s$ is Planck's constant. As a result, blue light has more energy than red light.

1.2.2 Fluorescence

Fluorescence is the process in which a fluorophore (also called fluorochrome) undergoes an electronic transition upon excitation and relaxes back to its ground state through emission of light. This is usually illustrated by a Jablonski energy diagram (*Figure 1.3*). This diagram shows different electronic states of the fluorophore. Prior to excitation, the ground state is represented by S_0, where *S* denotes the singlet state: all electrons of the fluorophore are spin-paired. The fluorophore can also reach singlet states with a higher energy level, termed excited singlet states (S_i, i = 1, 2, …). These excited singlet states are short living. Excited triplet states (T_i, i = 1, 2, …) in which the fluorophore holds a set of electrons that are spin-unpaired also exist and are relatively long living. At each of these states, the fluorophore can reside in a number of vibrational energy levels.

Fluorescence is essentially a three-stage process. In the first step, the fluorophore is excited from the ground state to a vibrational level of an excited singlet state through absorption of a photon within approximately $10^{-15}\, s$. This absorption only occurs when the energy of the incident photon matches the energy gap between the energy levels involved. As a result, the absorption spectrum of the fluorophore reflects its energy level distribution.

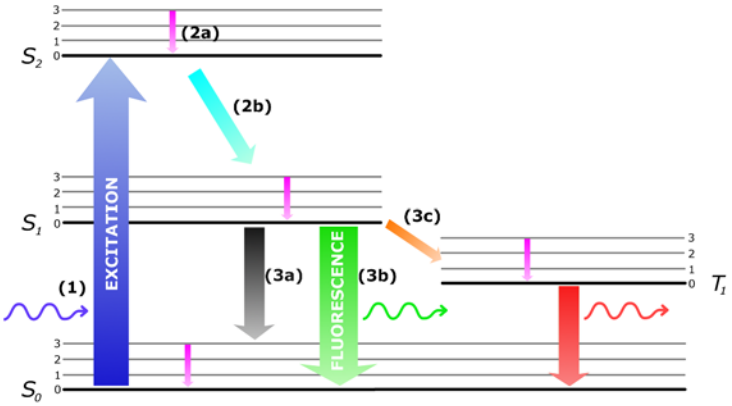

Figure 1.3: Jablonski energy diagram

The Jablonski energy diagram illustrates the three main processes that occur in the fluorescence process. Upon absorption of a photon (1), an electron in the ground singlet state (S_0) is promoted to an excited singlet state (S_1 or S_2). This step is quickly followed by radiationless vibrational relaxation (2a) and internal conversion (2b) to the lowest vibrational level of S_1. This lowest excited stated is eventually deactivated by radiationless internal conversion (3a), emission of a photon (fluorescence, 3b) or by intersystem-crossing to the triplet state T_1 (3c).

In the second stage, the unstable excited singlet state relaxes within about $10^{-12}\,s$ to the lowest vibrational level of the first excited singlet state S_1 by transferring energy to its environment through collisions. This vibrational relaxation needs to be complemented by the also non-radiative internal conversion for transit between excited singlet states.

Finally, the fluorophore relaxes from the first excited singlet state to a vibrational level of the ground state S_0. At this step, several competing processes exist: radiationless internal conversion, intersystem-crossing, radiationless energy transfer and fluorescence. The fluorescence pathway is the emission of a photon with an amount of energy that equals the gap between the first excited singlet state and a vibrational level of the ground state S_0. Since energy is dissipated in stage 2, the emitted photon has less energy than the absorbed photon. According to Eq. (1.2), the emitted photon has a longer wavelength than its absorbed counterpart. This difference in wavelength is called the *Stokes' shift*, named after Sir George Gabriel Stokes.[122] The efficiency of this fluorescence process is described by the fluorescence quantum yield q, i.e. the ratio of the emitted photons to the absorbed photons. The time scale of the

fluorescence process, often in the nanosecond range, is fluorophore-specific and can be characterized by a specific decay time, called the lifetime of the fluorophore.

A competing relaxation pathway is singlet-triplet intersystem-crossing, in which a transition from an excited singlet state to a triplet state takes place. This intersystem-crossing is followed by vibrational relaxation to the lowest vibrational level of the triplet state T_1, finally leading to phosphorescence upon relaxation to S_1. During this process, also a photon is emitted, but due to the larger energy dissipation in this pathway, this photon has a longer wavelength than the light originating from the fluorescence. The lifetime of T_1 can be orders of magnitude larger than the fluorescence lifetime.

1.2.3 Fluorophores

Studying a protein in the cell membrane of a biological cell using fluorescence techniques requires that the protein of interest can fluoresce. Few proteins, however, are fluorescent by nature. This intrinsic fluorescence of proteins originates from aromatic amino acids (tryptophan, tyrosine, and phenylalanine) incorporated in their primary structure. Together with a small group of other cellular components including the enzyme cofactor NADH and flavins, these proteins cause the autofluorescence of cells.

Proteins that do not exhibit an endogenous fluorescence need to be labeled by a fluorescent molecule. A common strategy is to use a fluorescently labeled antibody directed against the protein of interest. This strategy has an important drawback when investigating intracellular proteins in live cells. This problem is overcome by the introduction of fluorescent proteins. These genetically encoded fluorescent tags have can be used to construct fusion proteins comprising both the protein of interest as well as the fluorescent protein. Since both partners are proteins, they can be made by the biological cell itself. In this way, also labeling of internal proteins became possible, even in cells during live imaging.

1.2.4 Fluorescence microscopy

The Stokes' shift enables the separation of the emission light from the excitation light. An epi-fluorescence microscope achieves this separation by means of a dichroic mirror (DC) (*Figure 1.4*). In general, the DC reflects the excitation light, while it is transparent for the emission light. The contrast is further enhanced by introduction of an excitation and emission filter. In this way, only emission light can reach the detector. For a regular widefield epi-fluorescence microscope, the detector usually is a charge-coupled device (CCD camera).

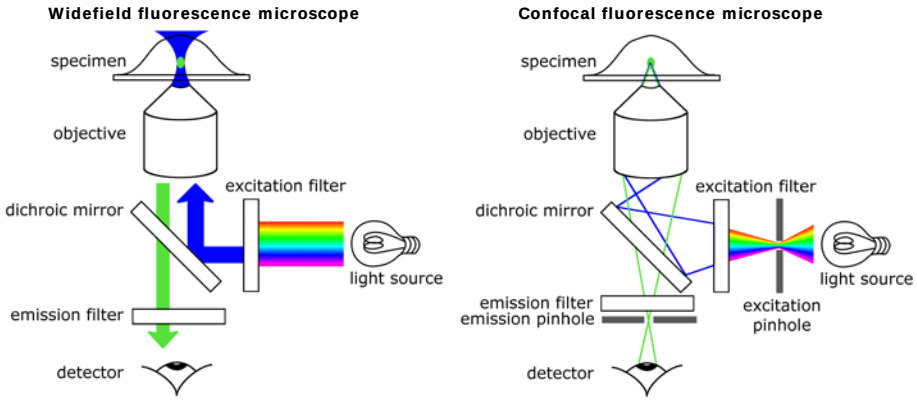

Figure 1.4: Comparison of a widefield and a confocal epi-fluorescence microscope

Through insertion of a pinhole in the confocal plane at the excitation and the emission side, a confocal microscope is obtained. This configuration has the advantages of eliminating all light that arises outside the focal plane in the sample. In this way the signal-to-noise ratio is dramatically improved. A laser is often used as a light source and the a photomultiplier tube (PMT) as a detector. The image is generated by scanning across the sample and recording pixel by pixel, hence the name confocal laser-scanning microscope (CLSM).

1.3 Aim of the study and achievements

The aggregation state of the GlyR has been shown to influence the receptor desensitization kinetics. In order to study effectors of the aggregation state of GlyR α_3, this aggregation state should be accurately determined. Furthermore, interaction with other sub-membranous proteins might lead to a decrease of the receptor's mobility. Therefore, the feasibility to study the aggregation and interaction of the receptors using ensemble microfluorimetric techniques was explored and results were compared with current literature about other receptor subtypes. Some of the applied techniques were extensively studied and adjusted or optimized where required.

The first technique applied was Fluorescence Recovery After Photobleaching (FRAP). This technique employs the recovery of the fluorescence intensity within a specified region after a short bleach phase to obtain the diffusion coefficient and the fraction of mobile receptors. A new method was introduced to select a reference area to render the technique less sensitive for the lateral heterogeneity in the plasma membrane of a living cell. Furthermore, a new approach was derived to estimate the variance of each recovery curve. This cancels the need to perform identical measurements to obtain this variance. This new approach was integrated with a simultaneous (global) analysis of the recovery curves, in which recovery curves are no longer analyzed individually but collectively.

The power of this new approach has been demonstrated by application of the generalized disk model. This new theoretical model, derived by prof. K. Braeckmans, brings the finite resolution of the optical microscope into account, both during bleaching as well as during image recording. This allows for the accurate analysis of bleach regions smaller than four times the point-spread function. This new model requires knowledge of both the detection and the bleach point-spread function. A global analysis of a data set comprising bleach regions spanning various sizes allows to determine this parameter together with the other parameters. Thereby calibration measurements can be omitted.

The other techniques that were applied are all related to Fluorescence correlation spectroscopy (FCS). Therefore, the basic principles of FCS were discussed first. This technique utilizes the normalized autocorrelation function

(ACF) of spontaneous, thermodynamic fluctuations that arise through diffusion of fluorescent particles to determine both the diffusion and concentration of these particles. Three related techniques utilize images and therefore they are termed image correlation spectroscopy (ICS), raster ICS (RICS), temporal ICS (TICS). ICS is the oldest of those three techniques and does not yield information on the dynamics of the receptors. However, it does allow to estimate the aggregation state of the receptor by comparing several test conditions. The only requirement is that the receptors are fixed or can be considered to be fixed during image acquisition.

RICS entails a similar analysis method as ICS, but this technique no longer assumes that the receptors are fixed. Furthermore, RICS requires the use of a confocal laser-scanning microscope (CLSM). In this way each image contains not only spatial but also temporal information that can be used to study the receptor dynamics. To improve the accuracy of RICS measurements, spatial ACFs of several images can be averaged. In comparison to FCS, RICS has the advantage that an image of the biological cell is generated. Because RICS is a relatively new technique, this method was first validated by mean of 3D isotropic diffusion of fluorescent beads.

TICS, the last technique applied, also allows to measure receptor dynamics. In contrast to RICS, the time course of fluctuations between individual images are used. TICS measurements are essentially many FCS experiments in parallel. This greatly reduces the required experiment time. Furthermore, TICS could also be used to return information on the immobile fraction based on the offset of the ACF. However, also other factors might contribute to this effect. Finally, the effect of bleaching during image acquisition on TICS results is investigated. It has been demonstrated that not only the rate of bleaching but also the overall loss of fluorescence is an important determinant.

These techniques were utilized to study the aggregation and mobility of GlyR α_3 *K* and *L*. Analysis of GlyR α_3 *K* using FRAP, RICS and TICS resulted all in a diffusion coefficient between 0.11 and 0.16 $\mu m^2/s$. These values are five times higher than values reported for GlyR α_1. This difference can largely be explained by a difference in temperature at which the experiments occurred. Frap analysis of GlyR α_3 *K* also indicates that the majority of these receptors are mobile. As a result, only a small fraction of the receptors are bound or apparently immobile

at the time scale of the measurements. Based on TICS measurements, it can be concluded that at least two subpopulations are present. Unfortunately, the experimental conditions do not allow to accurately study this slower population.

FRAP, RICS and TICS were also applied to GlyR α_3 *L*. Results obtained with FRAP could not be used due to the low density of the fluorescent particles, probably receptor clusters. The other techniques were successfully applied which resulted in a diffusion coefficient of at least a decade smaller that results obtained for GlyR α_3 *K*. Also for GlyR α_3 *L* two populations were detected by TICS.

The difference in diffusion coefficients between GlyR α_3 *K* and *L* could be explained by aggregation of GlyR α_3 *L*, by interaction of GlyR α_3 *L* with sub-membranous proteins, or by combination of both. ICS analysis of the receptors indicated that each aggregate of GlyR α_3 *L* comprised at least eight receptors. In conclusion, the difference in diffusion coefficients can at least in part be explained by aggregation of GlyR α_3 *L*. The cause of this aggregation, either inherent to the receptor or by interaction with other proteins, remains undetermined. To investigate the driving force of aggregation of GlyR α_3 *L*, one needs to compare the control situations with test conditions in which the putative interactions are prevented or disturbed.

Fluorescence Recovery After Photobleaching

2

Part of this chapter has been published as:

Smisdom N., Braeckmans K., Deschout H., vandeVen M., Rigo J.-M., De Smedt S.C., and Ameloot M. (**2011**) "***Fluorescence recovery after photobleaching on the confocal laser-scanning microscope: generalized model without restriction on the size of the photobleached disk***" J. Biomed. Opt. 16(4): 046021-8 [DOI:*10.1117/1.3569620*].

Fluorescence recovery after photobleaching (FRAP, also named fluorescence photobleaching recovery FPR) is a well-known microfluorimetric technique for measuring translational diffusion of fluorescently labeled molecules on a micrometer scale.[3] Application of FRAP to lateral diffusion in the plasma membrane of living cell requires extra attention. Potential pitfalls concerning this matter are discussed and a new approach using variance estimation, global analysis and a new theory are presented.

In addition to diffusion measurements, FRAP can also be used to study binding-kinetics e.g. protein binding to chromatin,[97] but this aspect is not covered below.

2.1 Introduction

The principle of FRAP is rather straightforward and did not change since its introduction in 1976.[3,4,28,90,140] Fluorescent molecules in a defined area (region of interest, ROI) are quickly and irreversibly bleached by irradiation with light of high intensity. These photobleached molecules will subsequently be replaced by diffusion of intact fluorescent molecules from the surroundings. The resulting gradual recovery of the fluorescence over time in the defined area (*Figure 2.1*), observed by using excitation light of low intensity, holds information on the diffusion process. Subsequent analysis of the fluorescence recovery data using a suitable FRAP model yields the translational diffusion coefficient D and the fractional amount of recovery M.

M is a measure for the fluorescence that is exchanged during the recovery. The fluorescence that is not exchanged during recovery can be explained as representing molecules that cannot be exchanged because they cannot move or move very slow. This fraction, calculated as 1- M, is called the immobile fraction. The mobile fraction M can be calculated by:

$$M = \frac{F_\infty - F(0)}{F_o - F(0)} \qquad (2.3)$$

where F_o is the pre-bleach intensity, $F(0)$ is the intensity immediately after bleaching, and F_∞ is the final recovered fluorescence intensity.

Originally, FRAP was performed on a regular fluorescence widefield microscope equipped with a stationary laser beam. This beam was used both for bleaching and read out of the fluorescence intensity. Nowadays, a CLSM is used for FRAP experiments, stimulated by its widespread use in life science laboratories. The combination of raster scanning and fast modulation of the laser beam intensity enables a CLSM to bleach and monitor arbitrary regions of interest (ROI) and makes it an easily accessible FRAP tool.[12]

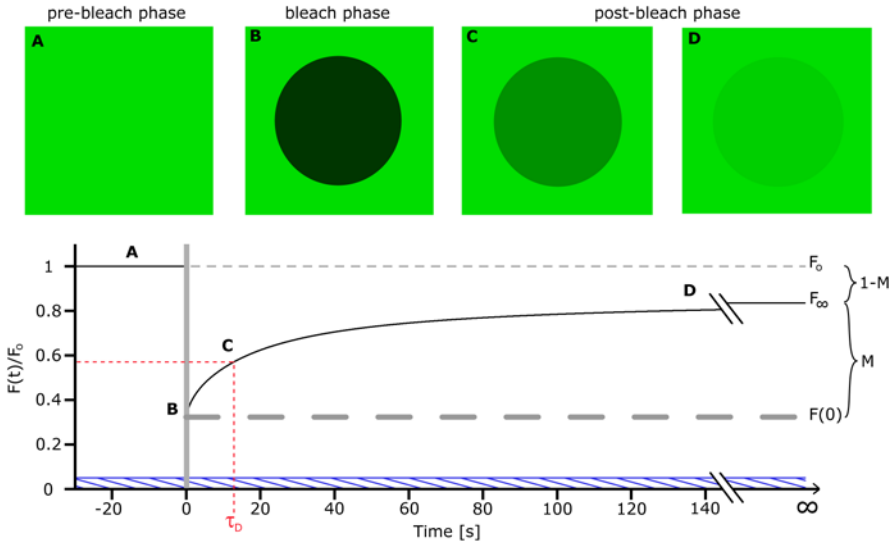

Figure 2.1: General aspects of a FRAP recovery curve

An exemplar, normalized recovery curve is shown together with illustrative cartoons. After determination of the pre-bleach intensity F_o (A), the fluorescence in the region of interest is partially bleached, reducing the intensity to $F(0)$ (B). This phase is used as time zero. Diffusion of the mobile proteins will lead to a recovery of the fluorescence in the post-bleach phase (C and D). F_∞ is the fluorescence intensity obtained at very long time. The relative amount of recovered fluorescence is a measure for the mobile fraction M, while the immobile fraction can be calculated by $1\text{-}M$. τ_D is the characteristic diffusion time (approximately 50% recovery). The blue hatched region indicates any background fluorescence.

2.2 FRAP data processing

Analysis of a FRAP experiment carried out on a CLSM consists of two steps. The first step involves the computation of a normalized recovery curve from the acquired time series of images. This obtained curve is subsequently fit to the appropriate theoretical model in the second step, yielding D and M.

The raw recovery curve $F_r(t)$ is extracted from the recorded stack of images by calculating the average pixel intensity within the bleach ROI for each frame. Ideally, normalizing $F_r(t)$ to its mean pre-bleach intensity $F_{r,o}$ would be sufficient. This single normalization, however, does not correct for artifacts that result from bleaching during data acquisition nor does it bring into account the background contribution. To cope with these effects, a double normalization is

suggested.[96,97] In this approach, two extra regions are extracted from the time series of images: one reference region $\mathcal{R}$ and one background region $\mathcal{B}$.

Region $\mathcal{R}$ is used to correct for instrumental fluctuations and bleaching during acquisition. This region should fulfill two requirements. First, it should hold a region for which a constant intensity can be inferred. In this way, any deviation from its initial intensity can be attributed to experimental limitations. And secondly, $\mathcal{R}$ should be representative for the bleach ROI, i.e. it should experience identical conditions as the bleach ROI, except for the FRAP bleaching. Furthermore, also the sample dynamics in $\mathcal{R}$ have to be identical to those in the bleach ROI.

The background region $\mathcal{B}$ has to comprise a region devoid of any intensity contribution derived from the fluorescent species.[97] The remaining intensity can be of instrumental (e.g. digital intensity offset, excitation light scattering) or biological origin (autofluorescence).

Using the average intensities derived from the three ROIs, the double normalization can be performed as:

$$\frac{F(t)}{F_o} = \frac{F_r(t) - \mathcal{B}(t)}{F_o\left[\mathcal{R}(t) - \mathcal{B}(t)\right]} \tag{2.4}$$

where the corrected mean pre-bleach intensity F_o is calculated as:

$$F_o = \left\langle \frac{F_{r,o}(t) - \mathcal{B}(t)}{\mathcal{R}(t) - \mathcal{B}(t)} \right\rangle \quad , \quad t < 0 \tag{2.5}$$

The angular brackets denote a time averaging of the pre-bleach intensity.

Although the extraction and calculation of the recovery curve seems to be straightforward, an extra difficulty arises when studying the diffusion or proteins in the plasma membrane of live cells. To correct for instrumental fluctuations and membrane undulations, a reference region needs to be selected. The most prevalent approach is to select a region sufficiently far from the bleach ROI (*Figure 2.2 a*). Due to the spatial heterogeneity of cells, the intensity of each part of the cell membrane appears not to have an identical time course. This becomes evident when comparing the results from the recovery curves obtained

with distinct reference ROIs. These results can easily differ one order of magnitude.

In an attempt to rationalize the selection of the reference region, a method was created that generates a mask of the cell and that excludes the bleach ROI and a sufficiently perimeter around it (*Figure 2.2 b*). Although this approach brings a lot more cell membrane into account, the resulting recovery curve often suffers from severe fluctuations.

Finally, a third method was developed, which is partially based on the method to select the reference region when studying nuclear proteins.[97] In contrast to the other techniques, the bleach ROI together with its perimeter now constitute the reference ROI (*Figure 2.2 c*). For a sufficiently large perimeter, the fluorescence intensity after bleaching can be assumed to be constant. For data points before and right after bleaching, this reference ROI is modified by selecting only a rim of the perimeter. The resulting approach allows to extract the recovery curve independent from the user's impression. Furthermore, since only the region in the vicinity of the bleach ROI is used, the reference ROI can be expected to better mimic the bleach ROI.

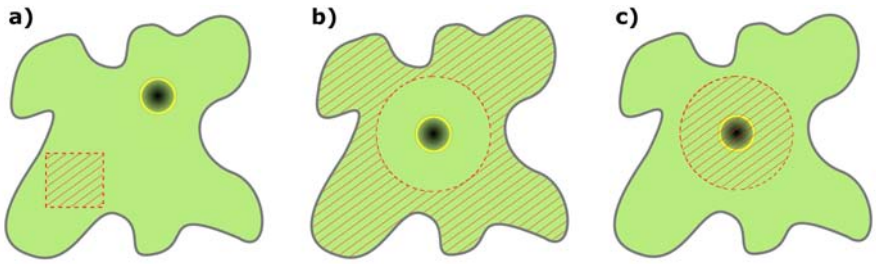

Figure 2.2: Schematic illustration of the selection of the reference ROI

a) Selection of the reference region by manually selecting the ROI at sufficient distance from the bleach ROI. b) Using a mask to select the reference ROI, also sufficiently far from the bleach ROI. c) selecting a region that comprises the bleach ROI and its perimeter in which the fluorescence can be assumed to be constant after bleaching occurred.

2.3 Estimation of weights

During the non-linear least squares fit of the data to a theoretical model, weights can be assigned to each data point to indicate its uncertainty. The uncertainty or variance of each data point, which is the inverse of the weights, can be obtained by repeating the FRAP experiment under identical conditions. In this way, the variance can easily be calculated per data point. However, when using biological cells it is not evident to exactly repeat an experiment. For example, the mobile fraction of a protein can be spatially heterogeneous. This extra source of variation will lead to incorrect weights. Ideally, one should be able to predict the weights of a recovery curve without having to rely on repetitions.

Each recovery curve in a FRAP experiment has its origin in a region of pixels from the time series of images acquired during recovery. Therefore, it should be possible to estimates the variance of each data point of the final recovery curve by starting from the variance of these individual pixels. The final estimated variances can subsequently be obtained by taking into account the propagation of errors through all applied mathematical operations.

2.3.1 Variance of individual pixels

Each pixel intensity can be considered to stem from a population with average intensity k and variance σ_k^2. The latter is of interest since it is the start for the recovery curve variance estimation. The pixel intensity population can be thought of as being obtained during imaging of an homogeneous solution. k can then be expressed as a function of the brightness ε of the fluorescent species, the average number N of fluorescent molecules in the observation volume and on an optional constant background intensity k_0:[26]

$$k = \varepsilon N + k_0 \qquad (2.6)$$

ε is defined as the number of photons detected per second per molecule and depends on the species' molecular absorption cross-section and its fluorescence quantum yield, but also on experimental conditions such as laser intensity and the detector sensitivity.

σ_k^2 will subsequently result from a combination of the variance due to the occupation number (σ_N^2) and the variance due to the detection (σ_d^2):

$$\sigma_k^2 = \sigma_N^2 + \sigma_d^2 \tag{2.7}$$

Variance due to the occupation number N is a common concept in *Fluorescence correlation spectroscopy* (*see p.49*) and depends on the square of the particle brightness ε:[22]

$$\sigma_N^2 = \varepsilon^2 N \tag{2.8}$$

The variance due to detection noise is for a detector operating in photon counting mode equal to the average signal:[26]

$$\sigma_d^2 = \varepsilon N + k_0 \tag{2.9}$$

This is also called shot noise. However, standard commercial CLSMs are often not equipped with photon counting detection. For a CLSM operating in analog detection mode, the current generated by the photomultiplier is proportional to the number of photons that are detected by the cathode once the dark current has been subtracted. Therefore, a scale factor S is introduced, which is the average conversion factor between one detected photon and the number of digital levels obtained after digitalization of the analog signal.[22] The number of digital levels is also determined by the gain in the analog to digital conversion and the selected digital offset $\mathcal{O}$ added to the signal. The average k can be expressed as:

$$k = S\left(\varepsilon N + k_0\right) + \mathcal{O} \tag{2.10}$$

The variance due to the occupation number can subsequently be calculated as:

$$\sigma_N^2 = S^2 \varepsilon^2 N \tag{2.11}$$

For the detection noise, an extra term is introduced to represent the read out noise due to the analogue to digital conversion:[22]

$$\sigma_d^2 = S^2\left(\varepsilon N + k_0\right) + \sigma_0^2 \tag{2.12}$$

The pixel variance can finally be expressed in terms of the average pixel value k by substituting Eq. (2.10), Eq. (2.11) and Eq. (2.12) into Eq. (2.7):

$$\begin{aligned}\sigma_k^2 &= S^2\varepsilon^2 N + S^2\left(\varepsilon N + k_0\right) + \sigma_0^2 \\ &= S\left(1+\varepsilon\right)k - S\left(1+\varepsilon\right)\left(k_0 + \mathcal{O}\right) + S^2 k_0 + \sigma_0^2 \\ &= ak - b\end{aligned} \tag{2.13}$$

This linear relationship allows to predict the variance of a pixel distribution with average k. For real systems, the slope and intercept of the pixel intensity mean-variance relationship can be determined by recording images of a dilution series of a homogeneous solution of the fluorescent species with identical instrumental settings as will be used in the final experiment.[22] The average and variance from regions of the resulting images can be calculated and plotted as variance as a function of the average. The slope and intercept of a linear fit through the data points will yield the slope and intercept of interest.

Unfortunately, this approach is not evident for biological samples where the concentration cannot be varied so easily. When $S >> \varepsilon$, the slope and intercept can be obtained by recording a series of images from homogeneous regions inside the sample using various laser intensities but identical detection settings as the final experiment. An identical analysis as described above for the dilution approach will yield the required parameters. An easier approach is to record a source of steady illumination, e.g. excitation light reflection, at various intensities and process the images in a similar way.[22]

2.3.2 Variance of recovery curve data points

$F_r(t)$ is extracted from the recorded stack of images by calculating the average pixel intensity within the bleach ROI frame by frame:

$$F_r(t) = \frac{\sum_{i=1}^{n_F} f_i(t)}{n_F} \tag{2.14}$$

where $f_i(t)$ is the i^{th} pixel intensity in the bleach ROI at time t and n_F is the total number of pixels inside the bleach ROI. Using the slope a and intercept b of the linear relationship between the average and variance of a pixel population, the variance of $F_r(t)$ can be calculated as:

$$\sigma^2_{F_r(t)} = \frac{aF_r(t)+b}{n_F} \tag{2.15}$$

The average and variance of the reference region $\mathcal{R}$, $\mathcal{R}(t)$ and $\sigma^2_{\mathcal{R}(t)}$, and background region $\mathcal{B}$, $\mathcal{B}(t)$ and $\sigma^2_{\mathcal{B}(t)}$, can be calculated analogously. Subtraction of the average background intensity and correction for any fluctuation in the reference intensity will lead to $F(t)$ and its variance $\sigma^2_{F(t)}$:

$$F'(t) = \frac{F_r(t)-\mathcal{B}(t)}{\mathcal{R}(t)-\mathcal{B}(t)} \tag{2.16}$$

$$\begin{aligned}\sigma^2_{F'(t)} = &\left[\frac{\sigma^2_{F_r(t)}+\sigma^2_{\mathcal{B}(t)}}{\left(F_r(t)-\mathcal{B}(t)\right)^2}+\frac{\sigma^2_{\mathcal{R}(t)}+\sigma^2_{\mathcal{B}(t)}}{\left(\mathcal{R}(t)-\mathcal{B}(t)\right)^2}\right]F'(t)^2 \\ &-2\frac{\sigma^2_{\mathcal{B}(t)}}{\left(F_r(t)-\mathcal{B}(t)\right)\left(\mathcal{R}(t)-\mathcal{B}(t)\right)}F'(t)^2\end{aligned} \tag{2.17}$$

Finally, $F'(t)$ needs to be normalized towards the average, corrected prebleach intensity F_o to obtain $F(t)$. F_o and its variance $\sigma^2_{F_o}$ can be calculated as:

$$F_o = \frac{\sum F'(t<0)}{n_{F'(t<0)}} \tag{2.18}$$

$$\sigma^2_{F_o} = \frac{\sum \sigma^2_{F'(t<0)}}{n^2_{F'(t<0)}} \tag{2.19}$$

The normalization itself can be calculated as

$$F(t) = \frac{F'(t)}{F_o} \tag{2.20}$$

$$\sigma^2_{F(t)} = \left[\frac{\sigma^2_{F'(t)}}{F'(t)^2}+\frac{\sigma^2_{F_o}}{{F_o}^2}\right]F(t)^2 \tag{2.21}$$

2.4 New generalized model and global analysis

In contrast to its fundamental principle, the instrumental implementation of FRAP changed over time. The regular fluorescence widefield microscope with a stationary laser beam for bleaching is often replaced by a confocal laser scanning microscope (CLSM). Commercial availability, user-friendliness, and optimized optical performance have led to the widespread use of these CLSMs in life science laboratories. The combination of raster scanning and fast modulation of the laser beam intensity enables a CLSM to bleach and monitor arbitrary regions and makes it an easily accessible FRAP tool.[12]

Together with this technical evolution new FRAP models are created for quantitative diffusion analysis. The models for non-scanning microscopes and two-dimensional (2D) diffusion[3,72,117] are replaced by CLSM-dedicated models. Most of these models, however, are either limited to 2D diffusion,[64] or apply a numerical approach with associated complexity.[10,65,91,129] One of the first FRAP models for analyzing CLSM FRAP data by using a simple closed-form equation, was based on the photobleaching of a uniform disk that is much larger than the effective resolution of the bleaching beam. We will refer to this model as the uniform disk model (UDM).[12] As demonstrated by Braeckmans *et al.*, the assumed bleach profile with sharp boundaries is no longer obtained when using smaller bleach regions (region of interest, ROI) due to the finite resolution of the bleaching beam. In this context, small or intermediate ROIs are defined as having a radius smaller than five times the resolution of the bleaching beam.[12] Diffusion coefficients obtained with these small ROIs will significantly underestimate the actual diffusion values when analyzed by the UDM.

Some applications require small or intermediate sized ROIs or do not allow for large ROIs at all. A clear example can be found in biological cells, which are limited in size by nature. Also investigation of anomalous diffusion of proteins requires the use of a range of ROI sizes.[5,48,108] Here we present a new, closed-form generalized FRAP disk model (GDM) which does not impose restrictions on the size of the circular bleached area. This is achieved through modification of the UDM by bringing into account both the bleaching resolution as well as the confocal imaging resolution. A procedure with simultaneous analysis of recovery curves derived from bleach regions of various sizes, i.e. a global analysis of the

resulting multidimensional data surface, is introduced for increased accuracy and a calibration free approach. A new method to estimate the variance of FRAP data was introduced to allow for proper weighting in this global analysis approach by nonlinear least squares. By a detailed experimental validation, we demonstrate that a wide range of diffusion coefficients can be accurately retrieved independent of the size of the bleached disk.

2.4.1 *Theoretical framework*

Subsequent theory is derived by Prof. dr. K. Braeckmans and is presented here for the sake of completeness.

2.4.1.a Effect of the finite width of the scanning laser beam on the bleached region

The derivation below of the GDM is valid for 2D diffusion in an infinite plane XY and single photon photobleaching and imaging. For this situation, it is shown by Braeckmans *et al*.[12] that the concentration C_b of fluorophores after irreversible photobleaching of a 2D geometry $B(r)$ with rotational symmetry around the Z-axis by a scanning beam can be described by:

$$C_b(r) = C_0 e^{-\frac{\sigma q}{v\Delta y}K(r)} \tag{2.22}$$

where C_0 is the homogeneous initial fluorophore concentration, v the line scanning speed, Δy the distance between consecutive scanning lines, σ the cross-section for single photon absorption, and q the quantum efficiency for single photon photobleaching. The bleaching geometry $K(r)$ that results from scanning the bleaching geometry $B(r)$ with the effective bleaching intensity distribution $I_b(r)$ of the scanning beam, can be calculated from the convolution product of $B(r)$ and I_b (*Figure 2.3*) according to:

$$\begin{aligned} K(r) &= B(r) \otimes I_b(r) \\ &= \int_{r'=0}^{+\infty} \int_{\theta'=0}^{2\pi} r' B(r') I_b\left(\sqrt{r^2 + r'^2 - 2rr'\cos\theta'}, t\right) d\theta' dr' \end{aligned} \tag{2.23}$$

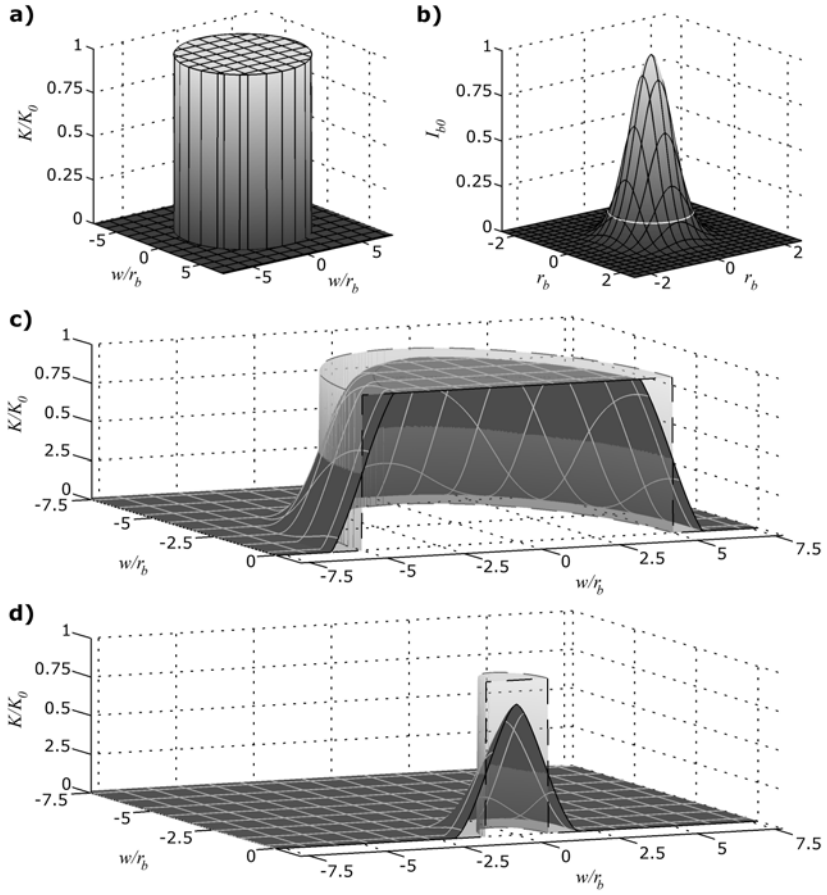

Figure 2.3: Graphical representation of the actual problem

(a) Three-dimensional illustration of $B(r)$ representing the ideal circular bleach geometry with sharp edges. In reality, this geometry is bleached by a scanning, focused laser beam with an effective bleaching intensity distribution $I_b(r)$ shown in (b). The white circle indicates the e^{-2} intensity level at which its radius equals r_b. The resulting bleach intensity distribution $K(r)$ is consequently the convolution product of $B(r)$ and $I_b(r)$. One half of $K(r)$ is shown for a radius w of 5 times r_b (c) and 1 time r_b (d). The gray shaded cylinder with dashed lines indicates the corresponding $B(r)$.

The effective bleaching intensity distribution $I_b(r)$ should not be confused with the intensity distribution of the illuminating laser beam. It was shown before that the effective photobleaching distribution is a complex function of the laser intensity distribution, the fluorophore photochemistry, the photon flux and the

physicochemical local environment.[13,14,80] Nor does $I_b(r)$ equal the imaging point-spread function (PSF) of a CLSM. The latter is the product of the illumination PSF at the excitation side and the detection PSF at the emission side,[51] while during the bleaching process only the excitation side matters.

The bleaching intensity distribution is approximated by a 2D Gaussian characterized by the effective bleaching resolution r_b:

$$I_b(r) = I_{b0} e^{-2\frac{r^2}{r_b^2}} \tag{2.24}$$

The convolution in Eq. (2.23) implies a modulation of $B(r)$ with the effective bleaching intensity distribution whose effect on the recovery process will increase as the dimensions of $B(r)$ approach r_b.

In order to obtain a closed-form solution further on for the recovery process, only a small amount of photobleaching is assumed, i.e. $\frac{\sigma q}{v\Delta y} K(r) << 1$, such that Eq. (2.22) can be linearized. Under this approximation, Eq. (1) can be expressed in terms of photobleached molecules C_b^* at time $t = 0$ as:

$$C_b^*(r) = C_0 - C_b(r) = C_0 \frac{\sigma q}{v\Delta y} K(r) \tag{2.25}$$

Combining Eq. (4) together with Eq. (2) and Eq. (3) yields:

$$\begin{aligned} C_b^*(r) &= \frac{\sigma q}{v\Delta y} I_{b0} C_0 e^{-2\frac{r^2}{r_b^2}} \int_{r'=0}^{+\infty} r' B(r') e^{-2\frac{r'^2}{r_b^2}} dr' \int_{\theta'=0}^{2\pi} e^{\frac{4rr'\cos\theta'}{r_b^2}} d\theta' \\ &= 2\pi \frac{\sigma q}{v\Delta y} I_{b0} C_0 e^{-2\frac{r^2}{r_b^2}} \int_{r'=0}^{+\infty} r' B(r') \mathrm{I}_0\left(\frac{4rr'}{r_b^2}\right) e^{-2\frac{r'^2}{r_b^2}} dr' \end{aligned} \tag{2.26}$$

where I_0 is the modified Bessel function of the 0th order. In order to obtain the recovery of fluorescence after bleaching, Fick's second law of diffusion has to be solved for the initial condition in Eq. (2.26). A solution can be easily found by noting that this expression resembles closely the general solution of the diffusion equation in cylindrical coordinates for a radially symmetric initial distribution $f^*(r)$ of bleached molecules and for a diffusion constant *D*:

$$C_{bf}^{*}\left(r,t\right)=\frac{e^{-\frac{r^2}{4Dt}}}{2Dt}\int_{r'=0}^{+\infty}r'\,f^{*}\left(r'\right)e^{-\frac{r'^2}{4Dt}}\mathrm{I}_0\left(\frac{rr'}{2Dt}\right)dr' \qquad (2.27)$$

where $C_{bf}^{*}\left(r,t\right)$ denotes the concentration of the bleached molecules arising from the initial distribution $f^{*}\left(r\right)$.

If now an initial concentration $f^{*}\left(r\right)$ and time $t=t_0$ can be found for which $C_{bf}^{*}\left(r,t_0\right)$ becomes identical to $C_b^{*}\left(r\right)$, the solution for Eq. (2.27) can be used and the intended closed-form solution can be obtained. This situation is met for $t=\frac{r_b^2}{8D}$, since it can be shown that $C_{bf}^{*}\left(r,\frac{r_b^2}{8D}\right)=C_b^{*}\left(r\right)$ for an initial concentration

$$f^{*}\left(r\right)=C_0\frac{\sigma q}{v\Delta y}\frac{\pi}{2}I_{b0}r_b^2B\left(r\right) \qquad (2.28)$$

as can be verified by substitution in Eq. (2.27). This initial concentration $f^{*}\left(r\right)$ in Eq. (2.28) can be considered to originate from bleaching a geometry $B\left(r\right)$ with a beam of infinite radial resolution $I_{b\delta}\left(r\right)=I_{b\delta0}\delta\left(r\right)$, where $\delta(r)$ is the Delta-Dirac function. This can be seen as follows. Assuming the bleaching process to be linear, one obtains in analogy with Eq. (2.25):

$$\begin{aligned}C_{b\delta}^{*}\left(r\right)&=C_0\frac{\sigma q}{v\Delta y}B\left(r\right)\otimes I_{b\delta}\left(r\right)\\&=C_0\frac{\sigma q}{v\Delta y}B\left(r\right)I_{b\delta0}\end{aligned} \qquad (2.28)$$

By comparing Eq. (2.28) and Eq. (2.28) we find that $I_{b\delta0}=I_{b0}\frac{\pi}{2}r_b^2$ and Eq. (2.28) becomes

$$f^{*}\left(r\right)=C_0\frac{\sigma q}{v\Delta y}I_{b\delta0}B\left(r\right)=C_0K_0B\left(r\right) \qquad (2.29)$$

where K_0 is the photobleaching parameter that determines the bleaching depth as used in the uniform disk model.[12]

In conclusion, the concentration distribution $C_b^*(r)$ as obtained by bleaching the geometry $B(r)$ with a laser beam of finite resolution characterized by r_b is the same distribution as obtained by diffusion from an initial concentration $C_0 K_0 B(r)$ after a time $t_0 = \frac{r_b^2}{8D}$ has elapsed. In other words, immediately after the bleaching phase, the bleached region with its shallow slopes created by a scanning laser beam can be regarded as originating from the perfect uniform disk with sharp boundaries through a diffusion process which started a time $t_0 = \frac{r_b^2}{8D}$ earlier. Introduction of the time shift $t \to t + \frac{r_b^2}{8D}$ in the UDM is sufficient to bring the finite width of the bleaching scanning laser beam into account.

2.4.1.b *Effect of finite total detection resolution on the time evolution of FRAP*

As the photobleached disk can now be of any size, the overall detection resolution r_d of the CLSM cannot be neglected anymore for very small or intermediate disks. This requires a revision of the uniform disk formula as described by Braeckmans *et al.*[12] The original UDM formula for 2-D diffusion is given here for the convenience of the reader:

$$\frac{F'(w,t)}{F_0'(w)} = 1 + \left(e^{-K_0} - 1\right)\left[1 - e^{-\xi}\left(\mathrm{I}_0(\xi) + \mathrm{I}_1(\xi)\right)\right] \qquad (2.30)$$

where $\xi = \frac{w^2}{2Dt}$, $F'(w,t)$ is the integrated fluorescence over the photobleached disk with radius w at time t after the bleaching period as observed by the CLSM, $F_0'(w)$ is the initial integrated fluorescence level within the ROI before bleaching, and I_0 and I_1 are the modified Bessel functions of 0th and 1st order, respectively. It has to be noted that r_b is neglected in the UDM model which is valid for large ROIs.

Nevertheless, the UDM can be easily extended to take r_d into account (calculations not shown here) leading to $\xi = \frac{w^2}{\frac{r_d^2}{4} + 2Dt}$ in Eq. (2.30). Note that for a large disk ($w >> r_d$) this indeed reduces to the familiar uniform disk formula.

Taken together, linearizing the photobleaching process, introducing the time shift as discussed above and taking the total imaging PSF into account, finally leads to the expression:

$$\frac{F(w,t)}{F_0(w)} = 1 - K_0\left[1 - e^{-\xi}\left(\mathrm{I}_0(\xi) + \mathrm{I}_1(\xi)\right)\right] \qquad (2.31)$$

where $\xi = \frac{w^2}{\frac{r_d^2}{4} + 2D\left(t + \frac{r_b^2}{8D}\right)} = \frac{w^2}{2Dt + R}$ with $R = \frac{r_d^2 + r_b^2}{4}$ and where $F(w,t)$ is the integrated fluorescence over the photobleached disk with radius w at time t, $F_0(w)$ is the initial value of $F(w,t)$ before bleaching. Eq. (2.31) will be referred to as the GDM since it is the generalization of the classic UDM taking into account the effective resolution of the bleaching beam and the microscope imaging resolution.

Common assumptions between GDM and UDM are initially uniformly distributed fluorescence molecules, an isotropic diffusion process in an infinite medium, absence of flow, a sufficiently short bleaching phase so as to neglect diffusion during bleaching and 2-D diffusion.[12] The latter assumption is satisfied for low NA lenses (which cause a cylindrical bleach profile) or lenses of high NA when the sample thickness is small compared to the axial resolution of the lens, as is e.g. the case for biological cell membranes.

Finally we note that the presence of an immobile fraction of molecules *M* can be taken into account by substituting the expression in Eq. (2.31) into the right hand side of:

$$F(w,t) = M\frac{F(w,t)}{F_0(w)} + (1-M)\frac{F(w,0)}{F_0(w)} \qquad (2.32)$$

2.4.2 Materials and Methods

2.4.2.a FRAP equipment

FRAP experiments were performed on two independent CLSMs. The first microscope (*setup A*) was an MRC1024 UV (Bio-Rad, Hemel Hempstead, UK) equipped with a custom-built FRAP module and a 4 W Ar-ion laser (model Stabilite 2017; Spectra-Physics, Darmstadt, Germany).[12,13] A 10× objective lens (CFI Plan Apochromat; Nikon, Badhoevedorp, The Netherlands) with a numerical aperture (NA) of 0.45 was used. The back aperture of this lens was only partially filled, resulting in a lower effective NA of ~0.2 and an r_d value of 1.0 µm as determined from subresolution beads.[13]

The second confocal setup (*setup B*) was an LSM 510 META (Carl Zeiss, Jena, Germany) installed on an Axiovert 200 M motorized frame (Carl Zeiss, Jena, Germany). It was equipped with a 30 mW Ar-ion laser and a 10× objective lens (Plan-Neofluar; Zeiss, Jena, Germany) with a NA of 0.3. The overall detection resolution r_d was 0.9 µm, as determined using sub-resolution beads. For both setups, a laser power of 0.5 to 1 mW at the sample was used for photobleaching.

2.4.2.b Sample preparation

FRAP measurements were performed on solutions of FITC-labeled dextran (FD) molecules (Sigma-Aldrich, Bornem, Belgium) with a molecular weight of 2000 kDa or 464 kDa. These compounds will be referred to as FD2000 and FD500, respectively. All stock solutions were prepared in HEPES buffered solution at pH 7.4. To increase the viscosity, solutions with 40% and 56% (w/w) sucrose (VWR Prolabo, Leuven, Belgium) were prepared from the FD stock solutions. The final fluorescence signal scaled linearly with the concentration as verified experimentally on each setup individually.

For FRAP experiments, 5 µl of the solution was sandwiched between a microscope slide and cover glass with Secure-Seal stickers (Sigma, Bornem, Belgium) of 120 µm thickness in between. This avoids any detectable flow inside the solutions while maintaining a 3D volume.

2.4.2.c FRAP protocol

All measurements were performed at room temperature. A fresh homogeneous region of the sample of interest was brought into focus before the start of each FRAP experiment. The execution of the experiments was controlled through the automated microscope bleach control software. The resulting stack of images represented a time-series recording with three consecutive phases (*Figure 2.4*). The first phase was marked by a set of one to five images showing the sample before bleaching. In the second phase, the user-defined circular ROI was bleached. The duration of the bleach phase did not exceed 1/10th of the characteristic recovery time τ_D,[84] where τ_D is defined as:

$$\tau_D = \frac{w^2}{4D} \tag{2.33}$$

Only one bleach iteration was allowed for all ROIs. Depending on the experiment, the nominal ROI radius as set in the control software ranged from 1.0 µm to 15.2 µm.

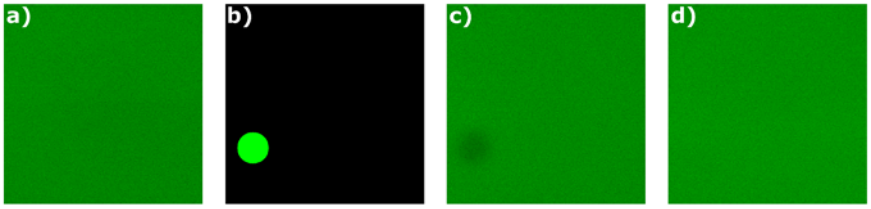

Figure 2.4: Three typical phases in a time series of a FRAP experiment.
(a) The fluorescence intensity is first recorded before bleaching. (b) The selected region of interest (indicated in green) is bleached. Only setup A registers the fluorescence intensities during this phase. (c) and (d) are respectively the first (directly after bleaching) and the last image of a series of post-bleach images monitoring the recovery of the bleached region.

Only the *setup A* registered fluorescence intensities during bleaching, resulting in one image showing the disk at the time of bleaching (hereafter called bleach image). All subsequent images showed the recovery of the fluorescence after the bleach-phase. This is the post-bleach phase. The time-interval between the images and the total acquisition time were selected so that when scaled to the recovery time τ_D a similar distribution of data points for all ROI sizes was obtained. Typically a time series of 50 images was recorded with a time of $\tau_D/3$

between the images as a trade-off between obtaining sufficient sampling of the recovery phase and limiting photobleaching due to imaging.

2.4.2.d Recovery curve extraction and variance estimation

All data extraction was performed in MATLAB (The MathWorks BV, Eindhoven, The Netherlands) using custom written routines. First, the coordinates of the circular bleach ROI were determined. For *setup A*, the center of the bleach disk was determined using a center-of-mass algorithm using the bleach image. For *setup B* this information was obtained from the metadata of the image sequence using a home-written routine.

Secondly, all pixels within the ROI were integrated frame by frame. A background region was selected at a distance of at least 4 times the radius of the bleach ROI. The recovery curve was corrected for changes in fluorescence intensity (e.g. by photobleaching during imaging or laser fluctuations) by normalizing the ROI fluorescence intensity by the background intensity. Finally, the recovery values were normalized to the mean pre-bleach intensity according to Eq. (2.31).

To allow weighted least-squares fitting of the experimental data to the theoretical model, the weight of each data point of this normalized recovery curve was the inverse of the estimated variance, taking into account all applied mathematical operations. Key to this variance estimation is the variance of the individual pixels, which was determined using the observed linear relationship between the unnormalized average pixel intensity and variance of homogeneous regions as described by Dalal *et al.* (*Figure 2.5 a*).[22] The average and variance of selected homogeneous regions from the recorded time series were calculated and resulting average-variance pairs with identical experimental settings were pooled across the data set to determine this linear relationship. Application of the propagation of errors subsequently when integrating over the number of pixels inside the ROI and considering other correction and normalization steps results in distinct variances associated with large and small ROIs (*Figure 2.5* b and c). A more elaborate description of this method can be found in *Estimation of weights* at page *23*.

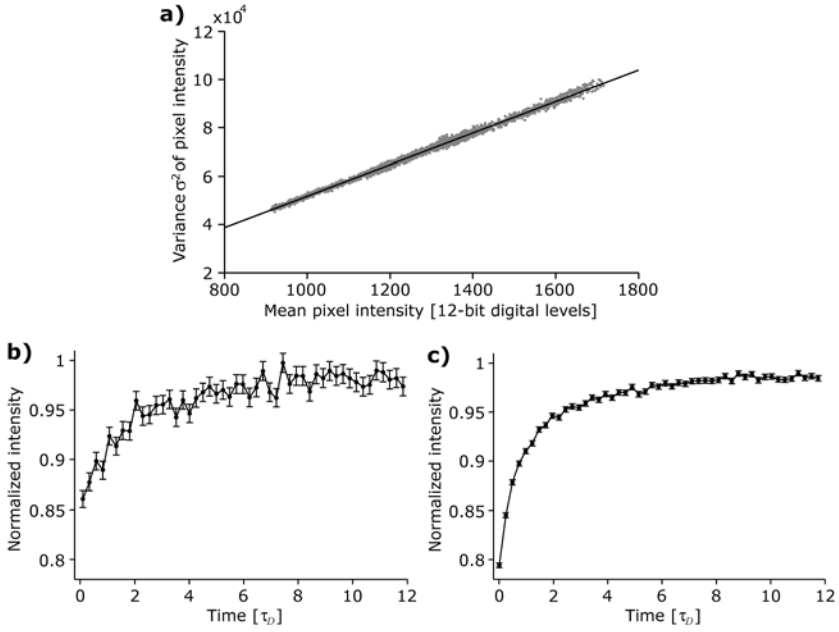

Figure 2.5: Variance estimation of recovery curve data points

Experimental relationship between the average pixel intensity (in digital levels) and the associated variance is shown in (a) for a given set of experimental parameters of setup B and a solution of FD500 in 40% (w/w) sucrose. Each average-variance pair is obtained from a homogeneous region from FRAP time series. (b,c) Two representative experimental, normalized recovery curves are shown. These curves were obtained using an ROI with a radius of (b) 1.9 µm and (c) 15.2 µm. Error bars indicate the estimated standard deviations. Time is expressed in units of τ_D to display both curves on an identical scale.

2.4.2.e Analysis of recovery curves

Each set of recovery curves was analyzed in two distinct ways. In the first approach, further referred to as single curve analysis, each curve was separately analyzed utilizing the calibrated resolution parameters r_b and r_d. In the second approach, two global analyses of all recovery data were performed. These global analyses respectively utilized and ignored the calibrated values of the resolution parameters to investigate the feasibility of recovering the combined resolution parameter R [cfr. Eq. (2.31)] exclusively from the recovery data themselves.

In the single curve analysis, each experimental recovery curve was fit to the UDM[12] [Eq. (2.30)] and to the new GDM [Eq. (2.31)], both adjusted for a

mobile fraction *M* through Eq. (2.32), using a weighted non-linear least-squares optimization minimizing

$$\chi^2 = \sum_{i=1}^{N} \beta_i \left(y_{i_{fit}} - y_{i_{data}} \right)^2 \qquad (2.34)$$

where N is the number of points in the fit and β_i is the inverse of the estimated variance of the i^{th} point. These weights were used to obtain statistically justified χ^2 values. Standard deviations on the recovered parameter values were obtained using a modification of the MATLAB routine *nlparci*.

For *setup A*, the photobleaching resolution r_b for both models was set to 2.5 µm: 2 µm as determined from lineFRAP experiments[14] increased with 0.5 µm to account for the 2 pixel rise time of the acousto-optical modulator (AOM). For *setup B*, r_b was set to 1.9 µm: 1.4 µm calibrated using lineFRAP (FD500 in 56% (w/w) sucrose, data not shown) increased with 0.5 µm analogously to *setup A*.

For the GDM, r_d was set to 1.0 µm and 0.9 µm for *setup A* and *B*, respectively. The mobile fraction *M* was set freely adjustable for consistency check: for the FITC-dextran solutions *M* should approximate one. Results were grouped per ROI radius by calculating the weighted average values of the obtained parameter values.

For simultaneous analysis of a set of recovery curves, home-written routines were used. These routines make use of a non-linear least-squares optimization algorithm. Parameters can be linked across recovery curves, i.e. made global, such that their values are equal for all selected recovery curves. Several sets of initial guesses were used to verify the true global minimum.

The obtained results were compared with the values obtained using the Stokes-Einstein equation

$$D = \frac{kT}{6\pi\eta r_H} \qquad (2.35)$$

where r_H is the hydrodynamic radius of the diffusing molecules, k the Boltzmann constant, η the dynamic viscosity and *T* the absolute temperature. The hydrodynamic radius of the FDs was calculated according to the relationship

reported by Braeckmans et al.[12] The dynamic viscosity η was obtained from the literature.[137]

2.4.3 Results

2.4.3.a Comparison of uniform disk model with new generalized disk model: single curve analysis

FD2000 solutions were used for *setup A* and FD500 solutions for *setup B*. The viscosity of the solutions was increased using different amounts of sucrose (40% and 56% (w/w)) to cover a range of diffusion coefficients (0.205 to 2.22 $\mu m^2/s$). For a given viscosity FRAP experiments were carried out on the same sample using photobleaching disks of varying radii. Hence, it was expected that all experiments would yield identical results.

Each experiment was analyzed by single curve analysis using the classic UDM and the new GDM. Representative results are shown in Figure 2.6. For all FRAP experiments analyzed, the mobile fraction *M* was close to 1 for both models, as expected from the model system used in these experiments. For *setup A* with r_b =2.5 µm, it could be expected that for the UDM the calculated D values are independent of the radius for radii >10 µm, i.e. 4-5 times the effective photobleaching resolution. For smaller radii, D values recovered using the UDM were expected to gradually decrease because of the underestimation of the effective ROI size. For the smallest disk size, the UDM underestimates the expected diffusion coefficient by a factor of 2. On *setup B* an entirely similar trend was observed, demonstrating that the deviations are not instrument related [*Figure 2.6 b*].

Analysis of the same data sets with the GDM nicely resulted in diffusion values that are independent of the size of the disk (within the experimental error). We note that small bleaching depths were used, $K_0 < 0.3$, consistent with the linearization in Eq. (2.25). Thus, the underestimation of the effective radius of the ROI in the UDM was appropriately compensated by the new model. For large ROIs, the D values of the UDM asymptotically approach the values of the GDM, as can be expected.

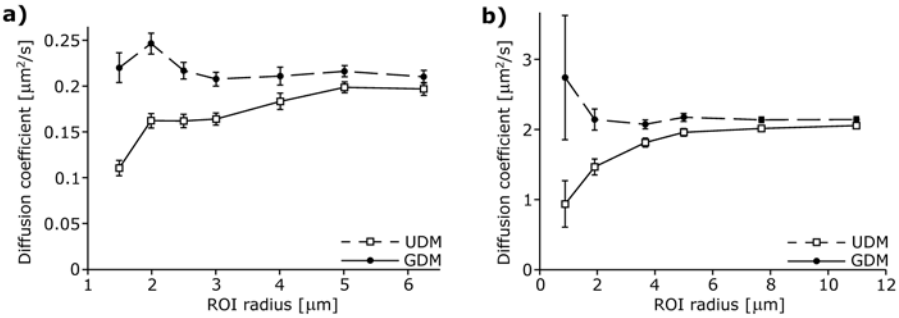

Figure 2.6: Comparison of the UDM and the GDM.

Comparison of the UDM (empty squares) and the GDM (filled bullets). Representative data sets are shown for setup A with FD2000 (a) and for setup B with FD500 (b) dissolved in respectively 56% and 40% (w/w) sucrose. Results are grouped per ROI radius using weighted averages of the obtained diffusion coefficient D. Number of recovery curves per ROI radius varied between 5 and 10. The UDM returned a diffusion coefficient that decreased with decreasing ROI radius, reaching a maximum underestimation at the smallest ROI size. Error bars are shown as standard deviations.

2.4.3.b Comparison of uniform disk model with new generalized disk model: global analysis

Since all recovery curves in a data set are derived from the same sample, they are all characterized by the same diffusion coefficient D. This is often implemented in the data analysis by averaging over all measurements, either at the level of the recovery curves themselves or at the level of the measured D values. In the current paper, a third implementation is used: a simultaneous analysis with the parameter D linked across all related recovery curves, i.e. a single, global parameter for D shared by all recovery curves. Other parameters like the bleaching depth and the mobile fraction can be kept local, i.e. these fitting parameters are specific for each individual recovery curve. This approach allows for differences in these parameters between recovery curves.

All data sets were analyzed using this global analysis applying both UDM and GDM. Similar as in the single curve analysis, the latter model made use of the calibrated resolution factor R by incorporating it as a fixed, i.e. non-adjustable parameter. For all data sets globally analyzed, D recovered using the UDM was consistently smaller as compared to the GDM that better approached the theoretical expected value (*Table 2.1*). The uncertainties on these recovered values are similar for both models. The underestimation of D by the UDM,

however, was smaller than observed using solely the smallest ROI size in the single curve analysis. In other words, inclusion of large ROI sizes moderates the underestimation of D, as can be expected.

Table 2.1: Comparison of global analysis results for UDM and GDM

Global analysis of FITC-dextran experiments for UDM and GDM at room temperature. Uncertainties are reported as standard deviations.

			Diffusion coefficient [$\mu m^2/s$]			
					GDM	
Setup	MW FD [kDa]	Sucrose/HEPES [% (w/w)]	Expected	UDM	R fixed*	R freely adjustable
A	2000	40	1.07	1.03± 0.01	1.08 ± 0.01	1.10 ± 0.02
A	2000	56	0.205	0.179 ± 0.003	0.216 ± 0.003	0.207 ± 0.005
B	500	40	2.22	2.11 ± 0.03	2.39 ± 0.03	2.26 ± 0.05
B	500	56	0.427	0.371 ± 0.008	0.423 ± 0.008	0.42 ± 0.02

* *Setup A*: R = 1.8 μm^2
Setup B: R = 1.1 μm^2

Single curve analysis of FRAP data using the GDM requires *a priori* knowledge of r_d and r_b, which are combined in the parameter R. This means that R is kept constant and identical in the individual analysis of all related recovery curves. However, in a simultaneous analysis of related recovery curves arising from different ROI sizes, the common value of the parameter R can be determined by linking R over the related curves, i.e. there is a single parameter *R* in the optimization routine. Best results are obtained when R is linked across as many ROI sizes as possible.

This approach does yield D values close to the expected values (Table 2.1). Compared to the approach that applies a fixed R, the recovered values of D are identical within the experimental error and their uncertainties nearly double but remain of the same order of magnitude. In other words, even without making use of *a priori* information on R, the correct D can be obtained when a range of ROI sizes is considered.

Since r_d is known, the r_b values can be calculated from the fitted R values. For all data sets analyzed, a physically relevant r_b value approaching the calibrated value is obtained (*Table 2.2*).

Table 2.2: Comparison of r_b obtained in global analysis with calibrated values

Comparison of the calibrated bleach resolution r_b with the recovered value from the global analyses using the obtained R and the calibrated value of r_d.

Setup	MW FD [kDa]	Sucrose [% (w/w)]	Calibrated values			Recovered values	
			r_d [μm]	r_b [μm]	R [μm^2]	R [μm^2]	r_b [μm]
A	2000	40	1.0	2.5	1.8	2.4 ± 0.3	2.9 ± 0.4
A	2000	56	1.0	2.5	1.8	1.4 ± 0.2	2.1 ± 0.3
B	500	40	0.9	1.9	1.1	0.8 ± 0.2	1.6 ± 0.4
B	500	56	0.9	1.9	1.1	1.1 ± 0.3	1.9 ± 0.5

2.4.3.c *Importance of R per ROI size*

The correction factor R is more important with decreasing ROI radius (*vide supra*).To experimentally confirm this statement, the accuracy by which R can be determined per ROI size is investigated. R should be obtained with higher accuracy from small ROI radius as compared to their larger counterparts. This was investigated by linking D over all recovery curves and by linking R within experiments of the same ROI size. The recovered values of R displayed a variability amongst the different ROI sizes without significant differences (*Figure 2.7*). It was obvious that the uncertainty on R increased with increasing ROI radius, thereby corroborating the theory.

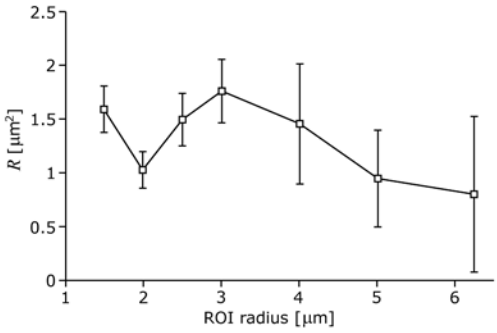

Figure 2.7: Resolution factor R as a function of ROI radius

The resolution factor R was calculated as a function or the ROI radius. Measurements were recorded with setup A and FD2000 dissolved in 56% (w/w) sucrose in HEPES buffer. Error bars represent standard deviations.

2.4.3.d *Effect of omitting the large ROIs in the global analysis*

Analysis including recovery curves from all ROI sizes led to a reliable result. Experimental conditions, however, do not always allow for large ROIs in case of

small samples. Therefore, it was necessary to investigate the performance of the new GDM with freely adjustable R when only these smaller sizes are considered. A global analysis was repeatedly performed starting with only the two smallest ROI sizes and progressively including larger ROI sizes. *Figure 2.8* displays the results of two representative data sets obtained with FD2000 in 40% (a) and 56% (b) (w/w) sucrose using *setup A* and analyzed by the presented method.

Applying this strategy using UDM, it comes as no surprise that the obtained values for D using only small ROIs severely deviate from the expected value (*Figure 2.8*). When also larger ROIs were included, D increased but never reached the expected value. With the GDM and a fixed value of R, on the other hand, the correct value of D could be found already with only 2 to 3 small ROI sizes at the expense of a larger uncertainty on the fitted parameters (*Figure 2.8*). This conclusion was similar amongst all data sets, indicating that small ROIs are sufficient to accurately determine D.

A similar analysis was performed using GDM but with a linked R across the data as a free fitting parameter. This approach yielded better D values than the UDM. In comparison with GDM with a fixed *R*, somewhat more variation in the recovered D values could be observed. Nevertheless, even without any prior knowledge of R, the GDM clearly outperforms the UDM.

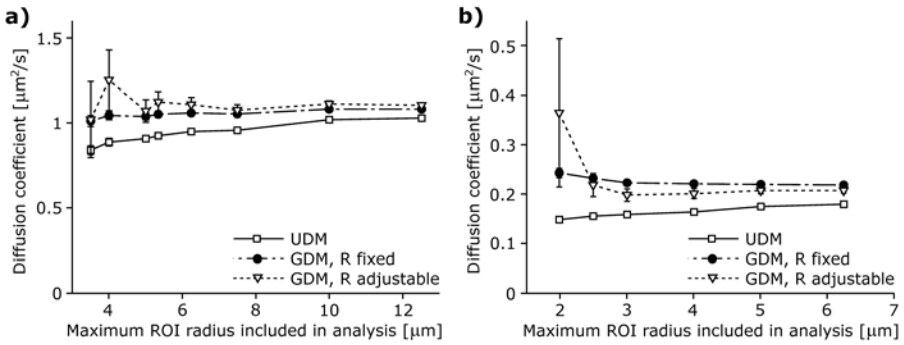

Figure 2.8: Global analysis results as a function of maximum ROI radius

Related data sets were repeatedly analyzed using global analysis while progressively including larger ROIs. D was linked across all included recovery curves. Representative data sets are shown obtained with FD2000 in (a) 40% and (b) 56% w/w sucrose/HEPES buffer using setup A. Error bars representing the standard deviations are shown if larger than the symbol size.

2.4.4 Discussion

The measured diffusion coefficient D of a system with free diffusion should not vary upon changing the radius of the bleach ROI. As shown by Braeckmans *et al.*[12] and also illustrated by the results in this study, this is not the case for small or intermediate sized ROIs when analyzed by the UDM. Since these small or intermediate sized ROIs are sometimes required for diffusion measurements in small samples,[5,48,108] a new model was developed. The resulting generalized disk model presented in this paper renders D essentially insensitive to the ROI radius, as is clearly demonstrated by the single curve analysis of recovery curves for each ROI size. This enables the use of these small and intermediate ROI sizes to obtain accurate D values on any CLSM.

Absence of recovery during photobleaching enables the full description of the resulting concentration profile immediately after bleaching by solely the radius of the ROI and the effective photobleaching resolution r_b. Together with the finite total detection resolution r_d, *a priori* knowledge of r_b is essential for the GDM using single curve analyses. While r_d can be determined by straightforward recording of sub-resolution beads, the calibration measurement required for determination of r_b is more laborious and difficult to obtain accurately since it depends on the type of fluorophore, photon flux and local chemical environment. Using a reference solution of known D, r_b can be estimated in a separate calibration measurement by means of lineFRAP.[14] However, this calibration does not include the rise time of the AOM and the calibrated r_b might still be underestimated. Therefore, it is suggested to use the GDM in combination with the global fitting procedure since this allows to extract the R value from FRAP experiments performed at various ROI sizes. Linking R across only a few small ROI sizes is sufficient to obtain a reliable result. For the experiments considered in this work about three ROI sizes were sufficient. Besides the estimation of R from the optimization, global analysis offers a second important advantage. The lower signal-to-noise ratio associated with smaller ROI sizes, together with a limited photobleaching depth required for the GDM, might decrease the accuracy of single curve fit analyses. Global analysis of all recovery curves, in contrast, is

still capable of returning relevant parameters, despite of a low signal-to-noise ratio.[8]

2.4.5 Conclusion

A new generalized disk model is introduced in a closed-form expression for analysis of FRAP recovery curves obtained at any ROI size. Using a simultaneous analysis of recovery curves obtained with a variety of ROI sizes, even in the absence of large ROIs, the diffusion coefficient D can reliably be obtained without prior calibration of the resolution parameters. The possibility to use a large range of ROI sizes not only offers the possibility of more flexible diffusion measurements, but is also expected to be valuable for more complicated measurements such as detecting spatial heterogeneities in the membrane organization or receptor distribution in the plasma membrane of live cells[5,108,111] and to investigate the connectivity between different domains in heterogeneous (bio)materials.[73]

Image Correlation Spectroscopy and Dynamic Variations

3

Parts of this chapter have been published as:

Gielen E.*, Smisdom N.*, De Clercq B., Vandeven M., Gijsbers R., Debyser Z., Rigo J. M., Hofkens J., Engelborghs Y., and Ameloot M. (**2008**) "***Diffusion of myelin oligodendrocyte glycoprotein in living OLN-93 cells investigated by raster-scanning image correlation spectroscopy (RICS)***" J. Fluoresc. 18(5): 813-9 [DOI:*10.1007/s10895-007-0308-8*].

Gielen E.*, Smisdom N.*, vandeVen M., De Clercq B., Gratton E., Digman M., Rigo J.-M., Hofkens J., Engelborghs Y., Ameloot, M. (**2009**) "***Measuring Diffusion of Lipid-like Probes in Artificial and Natural Membranes by Raster Image Correlation Spectroscopy (RICS): Use of a Commercial Laser-Scanning Microscope with Analog Detection***" Langmuir 25(9): 5209-18 [DOI:*10.1021/La8040538*].

* Gielen E. and Smisdom N. contributed equally to this work

Image correlation spectroscopy (ICS) and its dynamic variations constitute a group of techniques ideally suited for the study of membranous proteins. The time scales (ms to s) and sensitivity (0.5 to 100 proteins/µm²) offered by these techniques together with the commercial availability of CLSMs and TIRF-microscopes are important determinants in the establishment of ICS techniques.[21,61] They allow the study of various aspects of proteins in their native environment, including their distribution (surface density and aggregation state),[94] diffusion,[59] flow,[47] and interactions.

The group of ICS techniques have two important characteristics in common. First, they all start from an image or a stack of images and, secondly, they exploit the intensity fluctuations present within or between consecutive images. To understand the concept of fluctuations as a source of information, the closely related and historically preceding fluorescence correlation spectroscopy (FCS) technique is introduced first. FCS could be considered as a special case of the ICS family where the image resolution is limited to a single pixel. However, the success and merits gathered by FCS in the past 39 years[104] compel great respect for this technique. Therefore, it is best practice to regard the ICS family as descendants or extensions of FCS. The use of imaging FCS (imFCS) further highlights the close relationship between both.[50,109]

After this short introduction to FCS and the underlying principle of fluctuation correlation spectroscopy, a detailed discussion of selected ICS techniques follows, highlighting their advantages and weaknesses. The influence of experimental parameters is mapped and effective solutions are presented when available.

3.1 Fluorescence correlation spectroscopy

Fluorescence correlation spectroscopy (FCS) is defined as a technique that exploits the temporal fluctuations in a fluorescence signal obtained from a stationary observation volume to describe the processes giving rise to these fluctuations.[121] This description holds two essential points that need further elaboration to enable a good knowledge of FCS. First, one needs to understand how the fluctuations arise, and secondly, once these fluctuations are observed, it is essential to translate them into valuable information about their causal processes.

After this introduction to FCS fundamentals, special attention is paid to the case of FCS in the presence of multiple fluorescent species. A more elaborate review of FCS and its applications can be found elsewhere.[104,121]

3.1.1 Fluorescence intensity fluctuations

FCS uses fluctuations to describe dynamical processes, but one has to realize that it is not the only technique that analyzes stochastic fluctuations. In fact, fluctuation spectroscopy is a collection of techniques rather than a particular field of study.[76,132]

To observe the fluctuations of interest, FCS utilizes a small, open observation volume defined by a stationary excitation laser beam focused through a microscope objective (*Figure 3.1 a*). The average concentration within this sample volume is set by the surrounding reservoir, while fluctuations around this average are determined by the kinetics of local chemical reactions, diffusion or flow or a combination of these processes (*Figure 3.1 b-d*).[76,128] The time course of these fluctuations as well as their repetition rate hold information on the underlying mechanisms, which is exploited in FCS.

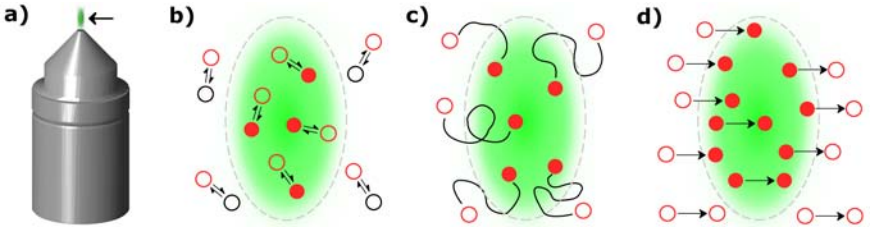

Figure 3.1: Origin of fluctuations in FCS

a) A microscope objective is used to focus a laser beam to create a diffraction-limited, open observation volume (arrow). In a system at equilibrium, the fluctuations observed in the fluorescence intensity from this femtoliter observation volume can arise from two types of processes. The first type, illustrated in b), involves a change in fluorescence yield of the molecules, e.g. dramatic increase of fluorescence yield of ethidium upon binding to a DNA strand. The second type arises when the fluorescence molecules move through the open observation volume. Typical examples are diffusion (c) and flow (d). A combination of both types can exist. The gray ellipse represents the observation volume outline.

The particles in the sample volume are monitored by means of fluorescence. Thus any molecule that is by itself fluorescent, or that can be tagged with one or several fluorochromes, is a putative candidate for FCS. The fluorescence signal is confined to the excitation beam, resulting in a small observation volume. Using confocal optics, this effective observed volume can be reduced further, leaving a diffraction-limited volume of a few femtoliters holding only a limited number of fluorescent molecules. The fluctuations in the fluorescence intensity signal observed from this volume reflect those of the number of fluorescent entities in this volume.[128] In general, all processes that lead to fluctuations in the fluorescence signal can be probed by FCS including chemical reactions leading to a change in fluorescence yield, rotational diffusion, triplet states, translational diffusion, and flow.[32,121] Also changes in the fluorescence intensity originating from technical limitations, like a limited laser stability – although less problematic with new generation lasers –, will be detected and should therefore be avoided at all costs.[121]

Essential to FCS is the magnitude of the observation volume. A small volume allows the reduction of the average number of molecules being simultaneously observed, which is in favor of fluctuation analysis. A small average number of particles will lead to larger relative fluctuations as compared to a large average number (*Figure 3.2*). For example, when a particle enters a volume holding only one particle, the signal will increase by 100%, while if the same particle enters a

volume holding 100 particles, the signal will increase by only 1%. The exact relationship between the magnitude of the fluctuations and the average number is discussed later on (*Autocorrelation function at p. 54*).

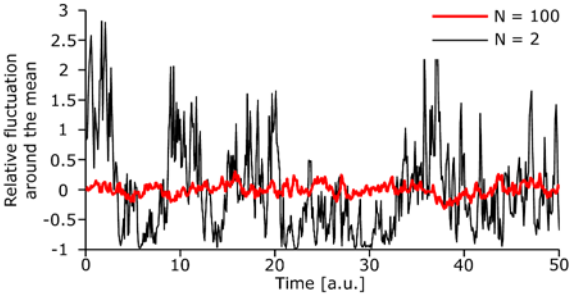

Figure 3.2: Effect of average number on relative fluctuation magnitude

a) A short time series of the relative fluctuation around the mean is plotted for an average number N of 2 and 100 molecules per observation volume. The large difference in magnitude is obvious, favoring lower numbers, i.e. lower concentrations and/or smaller observation volumes, for fluctuation spectroscopy.

Although FCS utilizes an observation volume, the movement of proteins in the plasma membrane of biological cells is restricted to the plane of the cell membrane. Its thickness (about 5 nm) is negligible compared to the axial waist of the observation volume. Consequently, when the plane of the plasma membrane is oriented perpendicular to the incident laser beam, the three-dimensional volume can essentially be replaced by a two-dimensional area, i.e. a radial cross-section of the volume (*Figure 3.3*). Within the scope of this thesis, only protein diffusion within the cell membrane is considered. Therefore, the expressions for 2D diffusion are emphasized in subsequent sections. This reduction of dimensionality is accompanied by a reduction of mathematical complexity while the fundamentals of FCS remain the same.

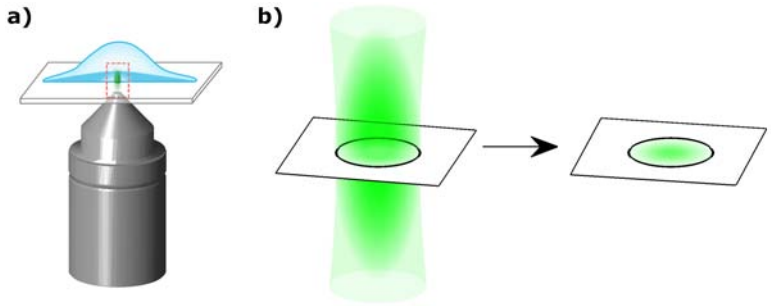

Figure 3.3: Reduction of 3D observation volume to 2D area

a) Schematic illustration of the orientation of the observation volume (green) to the plasma membrane of a biological cell (blue). b) Magnification of the red box in panel a). The movement of transmembrane or membrane-associated proteins is restricted to the plane of the plasma membrane of biological cells. (represented by the white plane). This allows the reduction of the 3D observation volume (the bright, green egg-shaped structure in the laser beam) to a 2D observation area (the green disk in the plane).

3.1.2 Autocorrelation function of the fluctuations

The fluorescence intensity from within the observation area is registered during a time period T resulting in a time series $i(t)$ (*Figure 3.4 a*). The fluctuations $\delta i(t)$ around the mean fluorescent intensity of this time series are obtained by using

$$\delta i(t) = i(t) - \langle i(t) \rangle \tag{2.36}$$

where $\langle i(t) \rangle = \frac{1}{T}\int_0^T i(t)\,d$ denotes the time average over the measurement time T. The fluctuations $\delta i(t)$ arise from one or several random processes and hence can be considered as a stochastic function with zero-mean. The unnormalized autocorrelation function (ACF) $G(\tau)$ of $\delta i(t)$ is defined as

$$\begin{aligned} G(\tau) &= \langle \delta i(t)\, \delta i(t+\tau) \rangle \\ &= \langle i(t)\, i(t+\tau) \rangle - \langle i(t) \rangle^2 \end{aligned} \tag{2.37}$$

where the angular brackets denote the time average over the measurement time T. The normalized ACF*, which amplitude ranges from 1 to 0, can be obtained using

$$g(\tau)=\frac{G(\tau)}{\langle i(t)\rangle^2}=\frac{\langle \delta i(t)\,\delta i(t+\tau)\rangle}{\langle i(t)\rangle^2} =\frac{\langle i(t)\,i(t+\tau)\rangle}{\langle i(t)\rangle^2}-1 \qquad (2.38)$$

$g(\tau)$ of $\delta i(t)$ will subsequently provide a measure of the average relationship between $\delta i(t)$ and $\delta i(t+\tau)$, $\tau > 0$†, (*Figure 3.4 b*).[89] The relative time separation τ is called the time lag. Rephrased in simple, applied terms it can be stated that the temporal ACF measures average properties of the fluctuations. These properties are duration, time course and amplitude. They can be used to describe respectively the rates and mechanisms of the underlying processes and the number densities of the fluorescent species in the observation volume.[121]

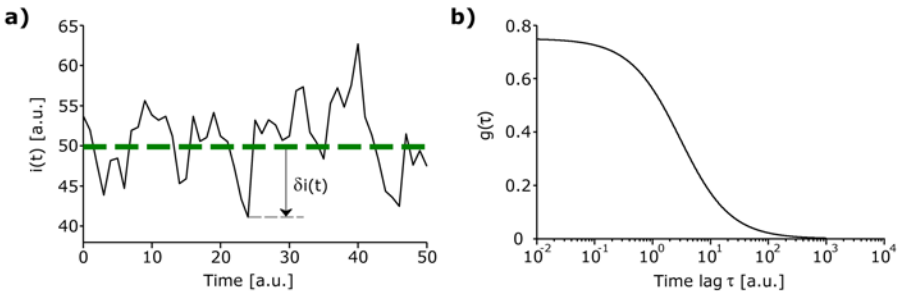

Figure 3.4: Analysis of fluctuations by means of their ACF

a) A short trace of a time series of fluorescence intensities $i(t)$ is plotted (black full line) together with its mean value $\langle i(t)\rangle$ (green dashed line). The fluctuation $\delta i(t)$ of one exemplar point is indicated. b) The average properties of the fluctuations are described by means of the ACF $g(\tau)$. A typical ACF for 2D diffusion is shown.

* *From this point on, the abbreviation ACF will be used to denote the normalized autocorrelation function, unless stated otherwise.*

† *The autocorrelation function is symmetric. τ can thus also have a negative value and $\delta i(t+\tau)$ can consequently also lie in the past. During the interpretation of the ACF, at least for temporal fluctuations, only $\tau \geq 0$ is considered.*

Eq. (3.1) through Eq. (3.3) utilize the time average of the fluorescence intensities. In theory the thermodynamic ensemble average should be used.[89,121] However, substitution of the ensemble average with the time average can be justified if, and only if, the fluorescence intensity is a stationary, ergodic signal. This assumption is only valid in absence of photobleaching during the measurement. The resulting time average approximation of the statistical ACF is called a sample ACF.[89]

3.1.3 Autocorrelation function analysis

Meaningful information can be retrieved from the ACF by fitting its time course to the analytical expression associated with the selected model. An appropriate model is selected based on the properties of the observation volume and the assumed mechanisms underlying the fluctuations.

3.1.3.a ACF for two-dimensional diffusion

The general analytical expression of the ACF in terms of the profile of the observation volume and the underlying mechanism can be obtained by first defining $\delta i(t)$ using these items as:[49,102,113,121]

$$\delta i(t) = I(r_o = 0)\kappa \int O(r_o)\,\delta\left(\sigma q C(r_o, t)\right) dr_o \qquad (2.39)$$

where r_o is a position in object space with its origin in the center of the observation volume. The excitation and detection features from the setup are represented in this equation by the excitation intensity amplitude $I(r_o = 0)$, the observation profile $O(r_o)$, and the overall fluorescence detection efficiency κ. The dynamics of the particles of interest, on the other hand, are described by the fluctuation term $\delta\left(\sigma q C(r_o, t)\right)$ that can include fluctuations in the molecular absorption cross-section σ, the fluorescence quantum yield q, and in the particle concentration $C(r_o, t)$.[113]

Eq. (3.4) can further be simplified by introducing the count-rate per detected molecule per second, ε:

$$\delta i(t) = \int O(r_o)\,\delta\left(\varepsilon C(r_o,t)\right) dr_o \tag{2.40}$$

where $\varepsilon = I(r_o = 0)\kappa\sigma q$ and with $\delta(\varepsilon C) = C_0\delta\varepsilon + \varepsilon\delta C$. C_0 is the spatially constant, average concentration of the molecules. Substitution of Eq. (3.5) into Eq. (3.3) finally leads to the general expression for the normalized ACF:[49,121]

$$g(\tau) = \frac{\int\int O(r_1)O(r_2)\left[C_0^2\left\langle\delta\varepsilon(t)\,\delta\varepsilon(t+\tau)\right\rangle + \varepsilon^2\left\langle\delta C(r_1,t)\,\delta C(r_2,t+\tau)\right\rangle\right] dr_1 dr_2}{\left[\varepsilon C_0\int O(r_1)\,dr_1\right]^2} \tag{2.41}$$

For the case of translational diffusion in absence of fluctuations in ε, Eq. (3.6) reduces to:[113]

$$g(\tau) = \frac{\int\int O(r_1)O(r_2)\,\phi(r_1,r_2,\tau)\,dr_1 dr_2}{\left[C_0\int O(r_1)\,dr_1\right]^2} \tag{2.42}$$

where $\phi(r_1,r_2,\tau)$ is the concentration correlation function. Note that the contribution of photon antibunching and fast photophysical or photochemical processes (triplet state dynamics, photo-isomerisation) of the fluorescent dye to the ACF is not brought into account. These fluctuations manifest on a time scale much smaller than the one accessible by the family of ICS techniques that will be discussed later on.[59]

In the case of an ideal solution, i.e. concentration- and position-independent diffusion coefficients, $\phi(r_1,r_2,\tau)$ can be solved using Green's function for classical diffusion kinetics:[49]

$$\phi(r_1,r_2,\tau) = \frac{C_0}{(4\pi D\tau)^{k/2}}\exp\left[-\frac{(r_1-r_2)^2}{4D\tau}\right] \tag{2.43}$$

where k is the spatial dimension and D is the translation diffusion coefficient. This function returns the joint probability of finding a molecule at a position r_1 at time τ if it was at position r_2 at time zero, multiplied by the average concentration.[113]

All that remains to obtain the final expression for the ACF of free, translation diffusion is the determination of $O(r_o)$, i.e. the geometry of the observation

profile. $O(r_o)$ is the product of the normalized illumination profile and the normalized collection efficiency profile $\Omega(r_o)$:

$$O(r_o) = \frac{I(r_o)}{I(r_o = 0)} \frac{\Omega(r_o)}{\Omega(r_o = 0)} \tag{2.44}$$

Any experimental geometry for $O(r_o)$ can be used, but often a symmetric 2D-Gaussian is assumed to obtain a closed analytical expression for 2D translation diffusion. The unnormalized profile $O'(r_o)$ for this geometry reads

$$O'(x, y) = \frac{2}{\pi \omega_0^2} \exp\left(-\frac{2(x^2 + y^2)}{\omega_0^2} \right) \tag{2.45}$$

where ω_0 is the radius of the observation profile at e^{-2} of its maximum intensity. For the normalized profile $O(r_o)$, the amplitude equals 1. Given this detection profile, the ACF for free 2D translation diffusion reads[112]

$$g(\tau) = \frac{1}{N}\left[1 + \frac{\tau}{\tau_D}\right]^{-1} \tag{2.46}$$

where N is the average number of molecules and τ_D is the characteristic diffusion time, i.e. the time the molecules spend on average in the observation volume. τ_D equals τ when the ACF drops to 50% of its initial value. Valuable information present in the ACF is obtained by fitting it to Eq. (3.11), yielding N and τ_D.

τ_D obtained from the fit is a technical parameter because of its dependence on the radius of the observation area. The larger this radius, the longer it will take for the molecule to diffuse throughout the observation area. Accordingly, conversion of τ_D to D is necessary to allow comparison between experiments on independent setups. D is inversely related to τ_D:[121]

$$\tau_D = \frac{\omega_0^2}{4D} \tag{2.47}$$

In words, the slower the particles diffuse, the larger τ_D will be (*Figure 3.5 a*).

The reciprocal of the ACF versus the lag time can be used as a consistency check[121,134] For a 2D situation, this plot should reveal a linear relationship because Eq. (3.11) can be written as:

$$\frac{1}{g(\tau)} = N + \frac{N}{\tau_D}\tau \qquad (2.48)$$

The ratio of intercept and slope of this line subsequently yield τ_D.

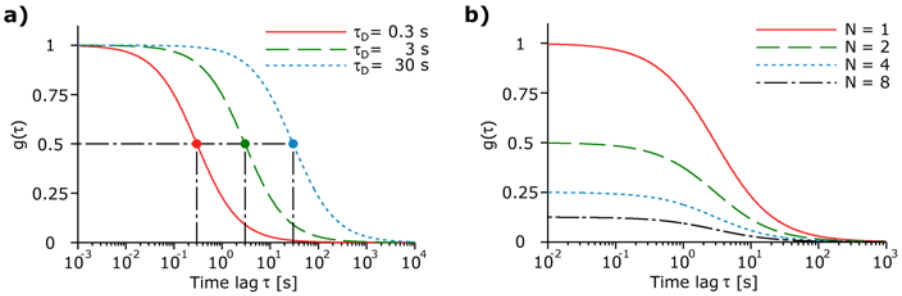

Figure 3.5: Interpretation of the autocorrelation function

a) The ACF holds information on the rate of the underlying process. A decreased rate results in a shift of the ACF towards longer time scales. Three ACFs of two-dimensional diffusion with $N = 1$ *are shown, each with a different residence time* τ_D *indicated by the dash-dotted lines at half of the maximum amplitude. b)* $g(0)$ *is equal to the reciprocal of the average number of particles* N *in the observation volume. The amplitude of the ACF decreases with increasing number. All four ACFs have* τ_D *= 3s.*

3.1.3.b ACF amplitude interpretation

From Eq. (3.11), it is obvious that the amplitude $g(0)$ of the ACF is a direct measure of the inverse of the average number of particles in the observation volume (*Figure 3.5 b*):

$$g(0) = \frac{1}{N} \qquad (2.49)$$

This follows from statistical mechanics: the variance of the fluctuations of independent random molecular processes in a system is equal to the reciprocal of N.[94,128] The variance of the fluctuations is also equal to the value of the ACF

in the limit as τ vanishes, i.e. $g(0)$. As a result, given the absence of noise, N would be the easiest parameter to be retrieved from the ACF.

However, in real experiments $g(0)$ will include a significant contribution from uncorrelated noise, rendering its direct calculation unsuitable.[21,76,94] Therefore, its value needs to be extrapolated from the ACF when approaching zero lag. This is achieved by fitting the calculated ACF to Eq. (3.11) while omitting the calculated $g(0)$ from the ACF. To distinguish the extrapolated $g(0)$ value from its counterpart directly observed from the ACF, the latter value will be denoted in this text as $g_o(0)$, where de index o denotes *observed*.

Although it seems rather easy to obtain the average number of molecules in the observation area, this value is actually a technical one. Its dependence on the dimension and shape of the observation area is obvious. When the area of the latter is known, N can directly be converted to an instrument-independent density:

$$C_0 = \frac{N}{V} \tag{2.50}$$

where V is the effective observation area. V created by the observation profile can be calculated as follows:[49]

$$V = \left[\int O(r_o)\,dr_o\right]^2 \left[\int O^2(r_o)\,dr_o\right]^{-1} \tag{2.51}$$

However, it is common practice to substitute the observation area with the integral of the normalized observation profile:[121]

$$V' = \int O(r_o)\,dr_o \tag{2.52}$$

which necessitates the introduction of a correction factor γ, also known as the shape factor:

$$\gamma = \frac{V'}{V} = \left[\int O^2(r)\,dr\right]\left[\int O(r)\,dr\right]^{-1} \tag{2.53}$$

For the assumed 2D Gaussian profile, γ equals $2^{-k/2}$ where k is the dimensionality of the observation profile.[121] In this way, the effective observation area of a 2D Gaussian profile, $V_{2DGauss}$, is:

$$V_{2DGauss} = 2\frac{\pi\omega_0^2}{2} = \pi\omega_0^2 \tag{2.54}$$

3.1.3.c *ACF in presence of multiple fluorescent species*

When n fluorescent species are present in the observation area, the intensity fluctuation around the mean can be written as the sum of n separate components:

$$\delta i(t) = \sum_{j=1}^{n} \int O(r_o)\,\delta\left(\varepsilon_j C_j(r_o,t)\right) dr_o \tag{2.55}$$

Using this definition, the ACF for multiple species can be calculated as:[121]

$$g(\tau) = \frac{\sum_{j=1}^{n}\sum_{l=1}^{n} \varepsilon_j \varepsilon_l \int\int O(r_1) O(r_2)\, f_{jl}(r_1, r_2, \tau)\, dr_1 dr_2}{\left[\sum_{j=1}^{n} \varepsilon_j C_{0,j} \int O(r_1)\, dr_1\right]^2} \tag{2.56}$$

where $f_{jl}(r_1, r_2, \tau)$ is the concentration cross-correlation function for species j and l, and $C_{0,j}$ is the spatially constant, average concentration of the j^{th} *species*. When the species do not interact, the mean cross-fluctuations terms can be assumed to be zero. The solution of Eq. (3.21) is found to be:[121]

$$g(\tau) = \sum_{j=1}^{n} \frac{\alpha_j^2 N_j{}^2 g_j(\tau)}{\left[\sum_{j=1}^{n} \alpha_j N_j\right]^2} \tag{2.57}$$

where N_j is the average number of particles of the j^{th} species in the observation area, $g_j(\tau)$ is the ACF of the j^{th} species as would be obtained in absence of the other species, and α_j is the relative brightness of the j^{th} species defined as

$$\alpha_j = \varepsilon_j / \varepsilon_1 \tag{2.58}$$

From Eq. (3.22), it can be learned that each species contributes to the total ACF by the square of its relative fluorescence contribution. When $u_j(\tau)$ is defined as the ACF of the j^{th} species for the situation that on average only one molecule of this species is present in the observation area, i.e. amplitude equal to 1, $g_j(\tau)$ can be rewritten as:

$$g_j(\tau) = \frac{1}{N_j} u_j(\tau) \tag{2.59}$$

Substitution of this expression into Eq. (3.22) leads to

$$g(\tau) = \sum_{j=1}^{n} \frac{\alpha_j^2 N_j}{\left[\sum_{j=1}^{n} \alpha_j N_j\right]^2} u_j(\tau) \tag{2.60}$$

The resulting $g(0)$ from a sample holding n species can thus be expressed as:

$$g(0) = \sum_{j=1}^{n} \frac{\alpha_j^2 N_j}{\left[\sum_{j=1}^{n} \alpha_j N_j\right]^2} \tag{2.61}$$

From this expression, it is clear that $g(0)$ can no longer be straightforwardly used as a measure for the concentration of the species, unless the relative brightness of each contributing species is known.

For the case of two species with equal brightness, Eq. (3.25) can be simplified to

$$\begin{aligned} g(\tau) &= \frac{N_1 u_1(\tau) + N_2 u_2(\tau)}{\left[N_1 + N_2\right]^2} \\ &= \frac{Y u_1(\tau) + (1-Y) u_2(\tau)}{N_{tot}} \end{aligned} \tag{2.62}$$

where N_{tot} is the total average number of particles in the observation volume and Y is the fraction of the first species.

3.1.3.d *ACF for a species with non-uniform brightness*

In the general theory presented above, each species is assumed to have a unique brightness, i.e. a fixed amount of fluorescent labels per particle, all with

identical properties. In biology, this assumption is best approached by proteins harboring an endogenous fluorochrome and for proteins genetically tagged with a fluorescent protein. For these situations, the fixed ratio of protein to label is obvious.

For cases where a different labeling method is used, a variation in the number of labels per protein can exist. The concomitant variance in the brightness per protein requires extra attention due to the importance of the brightness for the ACF as highlighted by Eq. (3.25). This situation arises when using a fluorescently labeled antibody, where it is conceivable to have a distribution of the number of labels per antibody. Given the brightness of each label is constant and independent of its location on the antibody, the antibody exhibits a brightness that is an integer multiple of the brightness of a single, fluorescent label. The labeled protein species can subsequently be considered as holding $n+1$ subspecies (comprising 0 to *n* labels), where n is the maximum number of labels the antibody can hold. Since the size of the fluorescent dye is often negligible compared to the size of the labeled protein, a varying number of fluorescent labels is thought not to influence the diffusion behavior of the protein of interest. As a result, $u_j(\tau)$ in Eq. (3.25) is constant across the subspecies of the protein and the problem of a species with non-uniform brightness is reduced to a correct interpretation of its ACF amplitude [Eq. (3.26)].

The solution to this problem of the ACF amplitude has already been applied for a similar case in which the aggregation of labeled monomers is studied, starting from identical preconditions.[92,95] It has been shown that for these conditions the amplitude of the ACF can be expressed as:[92]

$$g(0) = \frac{1}{N}\left(\frac{\sigma^2 + \mu^2}{\mu^2}\right) \tag{2.63}$$

where μ is the average number of labels per particle and σ^2 it the variance of the label distribution. In the end, knowledge of the mean and variance of the label distribution holds the key to a correct interpretation of the amplitude.

Coming back to the labeling of proteins using fluorescently labeled antibodies, one can assume that for a small number of fluorescent labels per antibody, this number is Poissonian distributed amongst the antibodies. μ and thus also σ^2 (

$\mu = \sigma^2$ for Poissonian distribution) of this distribution equal the degree of labeling of the antibody. This can experimentally be determined using absorption measurements. The resulting amplitude can then be written as:

$$g(0) = \frac{1}{N}\left(\frac{1+\mu}{\mu}\right) \tag{2.64}$$

where μ is the degree of labeling of the antibody. During analysis, one can work with an apparent average number of proteins $\mathcal{N}$ and correct it afterwards using:

$$N = \mathcal{N}\frac{1+\mu}{\mu} \tag{2.65}$$

When this effect is ignored, the concentration of the protein of interest, is underestimated by a factor of $\mu/1+\mu$ (*Figure 3.6*).

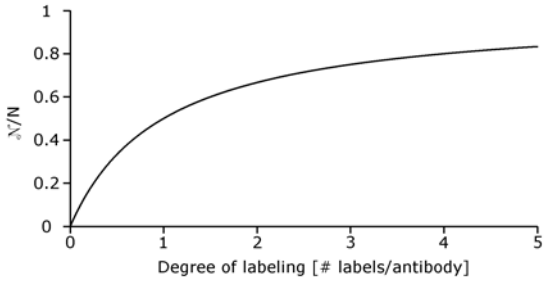

Figure 3.6: Underestimation of N when using a labeled antibody

The apparent average number of molecules in the observation area, normalized to its true counterpart, is plotted as a function of the degree of labeling of the antibody. The number of labels per antibody is assumed to follow a Poissonian distribution. The underestimation of N is evident and aggravates with decreasing degree of labeling.

3.1.4 Statistical accuracy of FCS

Since the introduction of FCS, considerable efforts are made to map the influence of experimental FCS parameters on the precision of FCS measurements in solution.[54,62,82,100,107,136] Some of these findings can also be applied to FCS of 2D diffusion. An essential point to realize is that the measurement of a single fluctuation, no matter how accurate, is insufficient to accurately determine the underlying mechanism.[107] Instead, statistical analysis of numerous fluctuations is required to obtain accurate results. This idea is

substantiated by the ACF. However, calculation of the true ensemble average ACF requires infinite experiment time, which is impossible to achieve.[107] As a result, the experimentally obtained ACF is an estimator of the true ensemble average ACF. A proper estimation of the sample ACF errors based on a single measurement allows for a correct weighting of the ACF during analysis without the need of several repetitions. This weighting is essential to recover correct estimates of the queried parameters describing the mechanisms provoking the original fluctuations.[136]

At least for 3D diffusion in an ideal system, determinants of the signal-to-noise ratio are measurement time T, concentration C of the fluorescent species and its brightness ε. Unfortunately, their effects are interrelated. It is reasonable to assume, at least to a certain extent, that their effects also hold for 2D systems. For measuring a diffusion coefficient, it is obvious that the accuracy of the FCS measurement is proportional to τ_D/T, but the exact relationship depends on its turn on ε: the higher ε, the smaller T is allowed to be in order to achieve an acceptable accuracy.[33,107] The contribution of ε is also complicated, since it depends on C: ε becomes more important when C decreases.[33]

When an FCS measurement is performed, extra experimental uncertainties will arise. A first important factor is the geometry and intensity distribution of the observation area. These can be affected by refractive index mismatches and incorrect cover-slide thickness, or *a priori* incorrect assumptions about these parameters can be made.[32,49] In addition to these optical aberrations, excitation saturation can also cause considerable artifacts.[32] Excitation saturation arises when the excitation rate of the fluorochromes in the detection area is no longer proportional to the excitation intensity.[32] The resulting artifacts manifest often as a spurious extra correlation terms and will often lead to erroneous parameter estimates.[32,49]

For 2D diffusion, the position and orientation of the sample plane with respect to the observation volume is a second important experimental factor.[85] Accurate positioning of the membrane in the confocal volume is essential. The radius of the cross-section between the observation volume and the sample plane parallel to the focal plane (*Figure 3.3*) increases with increasing axial distance from the

center of the observation volume.[116] As a result, the effective observation area experienced by the sample plane will increase and so will the characteristic diffusion time.[85,92] Neglecting this effect will lead to an apparent lower D. This effect is exploited by Z-scan FCS.[9,39]

Undulations of the membrane during the measurement might complicate the analysis even more. These small displacements of the membranes in the axial direction can contribute to an apparent anomalous diffusion behavior.[85]

Finally, a last factor that is known to affect the ACF, mainly its amplitude, is the instrumental noise.[62] This background noise can arise from thermal electronic noise or excitation light scattering. The amplitude of the ACF has to be larger than the ACF of the background noise, which is on the order of 10^{-4} to 10^{-3}.[92,121] This indicates the upper limit of N. Since the concentration of the fluorochrome can often not be arbitrarily adjusted, the size of the observation area should be reduced.[132] However, for 2D samples, the size of the observation area is not as stringent as for 3D systems due to the intrinsic limit of N resulting from the 2D configuration.[121]

The contribution of the background intensity should also be brought into account when the fluorescence intensity obtained from the fluorescent species is low, or when the background intensity is high compared the fluorescence intensity in general.[62] To show the effect of this contribution, Eq. (3.22) can be expressed in terms of average fluorescence intensity per species by substituting $\alpha_j N_j$ by $\langle i_j(t)\rangle$ in:

$$g(\tau)=\sum_{j=1}^{n}\frac{\langle i_j(t)\rangle^2\, g_j(\tau)}{\left[\sum_{j=1}^{n}\langle i_j(t)\rangle\right]^2} \qquad (2.66)$$

When the average contribution of the background is denoted by $\langle B(t)\rangle$, the effect of this contribution can be highlighted:

$$g(\tau) = \frac{\sum_{j=1}^{n} \langle i_j(t) \rangle^2 \, g_j(\tau) + \langle B(t) \rangle^2 \, g_B(\tau)}{\left[\sum_{j=1}^{n} \langle i_j(t) \rangle + \langle B(t) \rangle \right]^2} = \frac{\sum_{j=1}^{n} \langle i_j(t) \rangle^2 \, g_j(\tau)}{\left[\sum_{j=1}^{n} \langle i_j(t) \rangle + \langle B(t) \rangle \right]^2} \tag{2.67}$$

where the ACF $g_B(\tau)$ of the fluctuations in the background intensity is assumed to be zero. Although the absence of the background in the numerator, its contribution in the denominator is still present. Therefore, to obtain the correct ACF, the calculated ACF has to be multiplied with the background correction factor. Otherwise, a decreased $g(0)$ and thus an increased particle density will be obtained. The correction factor, C_B, can be calculated using the total average intensity $\langle i_{tot}(t) \rangle$ and $\langle B(t) \rangle$:[62]

$$C_B = \frac{\left[\langle i_{tot}(t) \rangle \right]^2}{\left[\langle i_{tot}(t) \rangle - \langle B(t) \rangle \right]^2} \tag{2.68}$$

where $\langle i_{tot}(t) \rangle = \sum_{j=1}^{n} \langle i_j(t) \rangle + \langle B(t) \rangle$.

3.2 Image correlation spectroscopy

Image correlation spectroscopy (ICS) is a tool for calculating the membrane receptor number densities or aggregation states.[94] Historically, ICS is a descendant of FCS, but for some this lineage might be obscure and very abrupt. In contrast to FCS, ICS starts from a single image with the imaged particles assumed to be fixed during the recording. However, there is a *missing link* that embodies the transition: scanning FCS (S-FCS).[92]

3.2.1 From S-FCS to ICS

Originally, S-FCS was introduced to overcome two problems encountered when studying the molecular weight of large molecules such as long DNA strands (up to full chromosomes) using FCS.[130] These large molecules exhibit a long characteristic diffusion time, requiring a very long experiment time to achieve an acceptable signal-to-noise ratio.[62,130] Furthermore, a long τ_D extends the exposure of the fluorochrome to the excitation light and the subsequent increased photodegradation will disturb the ACF.[130]

Basically, the first series of S-FCS experiments were a special case of FCS for uniform flow.[76,92] One was only interested in the number of macromolecules, i.e. the amplitude of the ACF, and diffusion was considered negligible.[130] The flow through the stationary observation volume increased the acquisition speed to rapidly obtain a large number of statistically independent samples.[130,131] The flow velocity was imposed by perfusion of the sample through a flow cell,[34,76], by a rotating cell,[130,131] or by linear translation of the sample through the laser beam.[76,92] The latter approach was successfully applied to study protein aggregation in biological cells.[93]

Another implementation of S-FCS is scanning a laser beam over a stationary, fixed sample.[76] Whether a fixed sample is moved at a uniform speed through a stationary laser beam or whether this laser beam is scanned at a constant speed across the stationary, fixed sample: both approaches result in identical ACFs.[95] However, it was only by the advent of the CLSM, giving access to rapid scanning, that boosted the application of S-FCS in biology. S-FCS measurements were extended to include multiple adjacent lines forming 2D images.[94] Consequently, the term ICS was adopted.

While ICS has its roots in S-FCS, the scanning beam is no longer necessary for this technique.[125] For fixed samples, any microscope can be used as long as the observation area is sufficiently oversampled, i.e. pixel size sufficiently smaller than the radius of this area. For unfixed samples like living biological cells, an extra requirement is put on top of the oversampling criterion. In order to have a negligible displacement of the observed fluorescent entities, the image acquisition time has to be minimal. For slow diffusion, this can be achieved by

very fast beam scanning or by means of a CCD camera with a short exposure time.

About 20 years after the introduction of SFCS, the technique revived through demonstration of its capability to measure diffusion rates using a CLSM.[63] The name scanning FCS was maintained, but to discriminate it in this text from its static predecessor, the new approach will be denoted as dynamic SFCS. It is implemented by repetitively scanning either a straight line (line-scan FCS) or an orbital. In both cases a spatiotemporal carpet, i.e. a 2D matrix with intensities as a function of space and time, is obtained.[103,106]

3.2.2 Spatiotemporal ACF

All members of the ICS family entail the calculation of an ACF, either in the spatial domain, in the temporal domain or in both. Therefore, the general spatiotemporal ACF (STACF) is introduced first.

Most members of the ICS family start from a time series, just like FCS. However, the time series $i(t)$ from FCS has to be extended to three dimensions, being the plane XY and time T. The resulting time series is denoted as $i(x,y,t)$, representing the fluorescence intensity at pixel location (x,y) in the image sampled at time t. Each frame in this time series of images is a convolution of the microscope PSF with the point-source emission from the fluorophores due to diffraction. All ICS techniques rely on this convolution to correlate fluorescence fluctuations over space, time or both.[61]

Because i is now a function of three independent variables, Eq. (3.1) can be rewritten as

$$\delta i(x,y,t) = i(x,y,t) - \langle i(x,y,t) \rangle_T \tag{2.69}$$

where $\langle\ \rangle_T$ indicates a temporal averaging of the stack of images. Since an image is a discrete set of data, the time averaging is performed as sums:

$$\langle i(x,y,t) \rangle_T = {}^{1}\!/_{N_T} \sum_{k=1}^{N_T} i(x,y,t_k) \tag{2.70}$$

where N_T is the total number of frames. $\langle i(x,y,t)\rangle_T$ is an image with resolution XY that holds for each pixel the time average for that pixel position throughout the stack of images. Since x and y are spatial coordinates and t is a temporal coordinate, $\delta i(x,y,t)$ is called the spatiotemporal intensity fluctuation around the ensemble average.

The time average used to define the intensity fluctuation is an estimate of the true ensemble average. When working with images, this ensemble average can also be accessed using the spatial average of each image, thereby assuming a homogeneous distribution of the particles. In an ideal system, both temporal and spatial averages are good estimates of the ensemble average. Therefore, these averages can be interchanged leading to the alternative definition of the (identical) fluctuations:

$$\delta i(x,y,t) = i(x,y,t) - \langle i(x,y,t)\rangle_{XY} \tag{2.71}$$

where the spatial average $\langle\ \rangle_{XY}$ of each frame in the stack is calculated as

$$\langle i(x,y,t)\rangle_{XY} = {}^{1}\!/_{XY} \sum_{n=1}^{X}\sum_{m=1}^{Y} i(x_n, y_m, t) \tag{2.72}$$

The definition of the fluctuations by Eq. (3.36) will be used throughout the rest of this chapter, unless stated otherwise.

Based on the definition of the spatiotemporal fluctuation, the corresponding three-dimensional, normalized, spatiotemporal ACF (STACF) can be calculated analogous to Eq. (3.3) as

$$g(\xi,\psi,\tau) = \left\langle \frac{\langle \delta i(x,y,t)\,\delta i(x+\xi, y+\psi, t+\tau)\rangle_{XY}}{\langle i(x,y,t)\rangle_{XY}\,\langle i(x+\xi, y+\psi, t+\tau)\rangle_{XY}} \right\rangle_T \tag{2.73}$$

where ξ and ψ are the spatial lags in respectively the X and Y direction.

3.2.3 ICS analysis

ICS analyzes the spatial fluctuations around the mean fluorescence intensity within an image through calculation of their spatial autocorrelation function

(SACF).[94] Depending on the experimental design (see *section 3.2.5*), the raw data can be a single image or a time series of *t* images.

The SACF is a special case of the STACF [Eq. (3.38)] with zero time lags (only within the image) and without averaging over the stack of t images:

$$g(\xi,\psi,0)_t = \frac{\langle \delta i(x,y,t)\,\delta i(x+\xi,y+\psi,t)\rangle_{XY}}{\left[\langle i(x,y,t)\rangle_{XY}\right]^2} = \frac{\langle i(x,y,t)\,i(x+\xi,y+\psi,t)\rangle_{XY}}{\left[\langle i(x,y,t)\rangle_{XY}\right]^2} - 1 \tag{2.74}$$

where the spatial fluctuation $\delta i(x,y,t)$ is calculated using Eq. (3.36). This will actually yield *t* number of SACFs. For discrete data sets like images, Eq. (3.39) can be evaluated as:[94]

$$g_o(\xi,\psi,0)_t = \frac{1/XY \sum_{n=1}^{X}\sum_{m=1}^{Y} i(x_n,y_m,t)\,i(x_n+\xi,y_m+\psi,t)}{\left[1/XY \sum_{n=1}^{X}\sum_{m=1}^{Y} i(x_n,y_m,t)\right]^2} - 1 \tag{2.75}$$

Direct calculation of the SACF using Eq. (3.40) is computationally demanding, but one can calculate the numerator of the SACF from the Fourier transform (FFT, $\Im$) of the power spectrum of the data, which in turn is calculated as the product of the FFT of the original image and its complex conjugate ($\Im^*$):[94]

$$g_o(\xi,\psi,0)_t = \frac{1/XY\ \Im^{-1}\left(\Im\left[i(x,y,t)\right]\Im^*\left[i(x,y,t)\right]\right)}{\left[1/XY \sum_{n=1}^{X}\sum_{m=1}^{Y} i(x_n,y_m,t)\right]^2} - 1 \tag{2.76}$$

To analyze the obtained SACFs, the observation area is assumed to have a 2D-Gaussian profile [Eq. (3.10)]. The resulting SACF can theoretically be predicted as:

$$g(\xi,\psi,0)_t = \boldsymbol{g}(\mathbf{0},\mathbf{0},\mathbf{0})_t \exp\left(-\frac{\xi^2+\psi^2}{\boldsymbol{\omega}_{0,t}^2}\right) + \boldsymbol{g}_{\infty,t} \tag{2.77}$$

where the dc component g_∞ is included to account for any non-zero correlations at large correlation distances due to the finite dimensions of the image.[92,94] The parameters printed in bold are optimized during the fit routine. During this fit, $g_o(0,0,0)$ receives zero weighting.

In the end, the ICS analysis of each image will yield three parameters. This list is further expanded by addition of the average image intensity $\langle i(x,y,t)\rangle_{XY}$ of each frame.

3.2.4 Conversion of ICS parameters to relevant biological parameters

Analogously to FCS, the average number of independent particles N in the observation area can be calculated as the inverse of $g(0,0,0)$. N on its turn can be converted to the particle density $\mathcal{P}$, which is the number of particles per μm^2, by dividing by the effective area $\pi\omega_0^2$ of the observation area [Eq. (3.15)]:[94]

$$\mathcal{P} = \frac{N}{\pi\omega_0^2} = \frac{1}{\pi\omega_0^2 g(0,0,0)} \tag{2.78}$$

In the literature, $\mathcal{P}$ is often denoted by *cluster density*.[95] However, an independent particle refers to any separate fluorescent entity. So a cluster of monomers as well as a single monomer will both be detected each as a particle. Therefore *cluster density* might lead to confusion and $\mathcal{P}$ is used instead.

Based on $\mathcal{P}$, an estimate of the degree of aggregation, $\mathcal{A}$, can be defined as the number of individual monomers per particle by dividing the average fluorescence intensity per particle by the average fluorescence intensity per monomer ε_m:[95]

$$\mathcal{A} = \frac{\langle i \rangle}{\varepsilon_m \mathcal{P}} \tag{2.79}$$

Even when ε_m is unknown, $\mathcal{A}$ can still be used as a relative measure given identical imaging settings are used. As a result, $\mathcal{A}$ is a convenient measure for following aggregation or dispersion in time.[95]

3.2.5 ICS applied to protein distribution and aggregation

ICS assumes that all imaged fluorescent particles are immobile during the acquisition. As a result, no information on the protein dynamics will be returned by the analysis *per se*. However, by comparing different situations, e.g. before and after stimulation or treatment, changes in receptor distribution or aggregation in the cell membrane can be detected.[95]

In general, two strategies exist to apply ICS. The first strategy has its origin in scanning FCS, in which fixated cells were used.[92,93] For each condition, cells are fixated and stained. To get a statistically relevant result, several cells are selected and imaged. One image or an accumulation of several images (to increase the signal-to-noise ratio) is recorded per cell and analyzed as described above. Afterwards, the average density $\mathcal{P}$ and degree of aggregation $\mathcal{A}$ of each condition are calculated. The final result is obtained by comparing $\mathcal{P}$ and $\mathcal{A}$ between the experimental conditions.

The advantage of this first strategy is that the image acquisition does not need to be fast, improving the quality of the recorded images. There are no special requirements for the acquisition system, except for sufficient sensitivity. The major drawback of this strategy is the necessity for extra conditions to check the effect of fixation.[94]

The second strategy also assumes that all proteins are immobile during the image acquisition. However, this condition is fulfilled by limiting the acquisition time instead of using chemical fixatives. The maximum acquisition time allowed is a function of the diffusion rate of the proteins of interest, but often a fast scanning system or a fast CCD camera are used. This approach has two advantages as compared to the first strategy. First, there is no interference by a fixation step and secondly, several images per cell are recorded. Although the image quality is partially sacrificed by the acquisition speed, each image represents a different snapshot of the cell. In this way, their SACFs can be averaged. This second approach also allows for monitoring changes in distribution or aggregation state as a function of time within a single cell.

3.2.6 Statistical accuracy of ICS

The statistical accuracy of ICS is mainly determined by the number of independent fluctuations, NIF.[21] NIF can be calculated as the ratio of the imaged area to the observation area. It is comparable to the ratio of τ_D to T in FCS. Although an increase in NIF yields better statistics, this number is often bounded by the physical dimensions of the biological cell. Furthermore, edges or other sharp boundaries or structures should be avoided since they perturb the SACF.[21,94] This can be accomplished by afterwards selecting a homogeneous rectangular region within the cell, or by decreasing the pixel size (increasing the *zoom*) such that only a homogeneous area is imaged.[94,133] In addition, it has been shown that the particle density has no significant effect on the accuracy.[21]

A detailed study of ICS applied to platelet-derived growth factor-β receptor clustering has indicated that the biological variability exceeds the technical variability by at least an order of magnitude.[133] This highlights the need of a sufficiently large sample size.

3.2.7 Practical aspects

ICS has been used to study membrane receptor aggregation in great detail.[133] As for FCS, the offset of the image intensity, i.e. the dark current of the system, has to be brought appropriately into account to obtain correct number densities. This is achieved through correction of the obtained amplitudes using the correction factor as defined in Eq. (3.33).[133] A different approach is to subtract the average dark current intensity from each image before further analyses. The average dark current intensity is determined using dark current images. Due to possible instrumental instabilities, dark current images should be recorded regularly during the course of the experiment.[133]

During the fit of the SACF, $g(0,0,0)$ receives zero weight. However, for experimental data, the contribution of the noise is often not limited to the zero spatial lags. Instead, the correlation of the noise might persist in other spatial lag channels.[94] For CLSM, this persistence is often orientated along the quickest scan dimensions (usually ξ). Since the scan process is often relatively slow to improve the signal to noise ratio, this detection noise correlation is often limited

to the first spatial lag channel. Its contribution can be neutralized by assigning also zero weights to these lag channels.[94]

The fit of the SACF will subsequently yield three parameters, of which mainly the amplitude of the SACF is of interest. However, ω_0 is also required to obtain the particle density. When ω_0 is calibrated independently, e.g. using sub-resolution beads, its value recovered from the fit can be used as indicator of the quality of the data. Smaller values of ω_0 are indicative for sharp edges or unusual large noise levels. Large values, on the other hand, suggest the presence of larger structures like patches in the image that exceed the resolution.[94] As a rule of thumb, obtained values of ω_0 should be within 30% of the calibrated value of the microscope system.[94] Otherwise, the frame of interest should be discarded in further analyses. Similar to FCS and SFCS, ICS depends on accurate determination of the observation area.

3.3 Raster image correlation spectroscopy

Raster image correlation spectroscopy (RICS) is also a member of the family of ICS techniques. Similar to ICS it employs the fluctuations within an image. Although the other members of the family have no special requirements about the origin of the images, it is essential for RICS that the images are acquired using a laser-scanning microscope.[25] Extra time information is present inside a single image because of the scanning motion of the laser beam. This implicit time information is utilized by RICS to study dynamic processes. In this respect, RICS can be regarded as the dynamic version of ICS.

Historically, however, transition from ICS to RICS has not been that straightforward, as the 12 years between the conception of both techniques suggest.[25,94] Introduction of dynamic SFCS was an important step in this transition. It proved the feasibility of using a CLSM to measure dynamics by repetitively scanning a line or orbit.[63] RICS makes use of a CLSM, but the original dynamic SFCS approach was modified in two ways. First, RICS records adjacent lines instead of the same line over and over. And secondly, it simultaneously considers fluctuations within and between recorded lines. In this

way, two time scales become available. The latter modification is recently also applied to dynamic SFCS.[103]

3.3.1 Principles of RICS

RICS operates on a time series of images acquired through the raster-scanning of a CLSM. Each image is built pixel by pixel and line by line (*Figure 3.7*). In this way, each image holds besides the regular spatial information also *hidden* time information. Adjacent pixels along a scanned line are a few microseconds apart (pixel dwell time, τ_P), while pixels over successive lines are a few milliseconds apart (line time, τ_L). In this way, two time scales are accessible. The frame time, i.e. time between the start of successive images, is even larger, but this time is not employed by RICS.

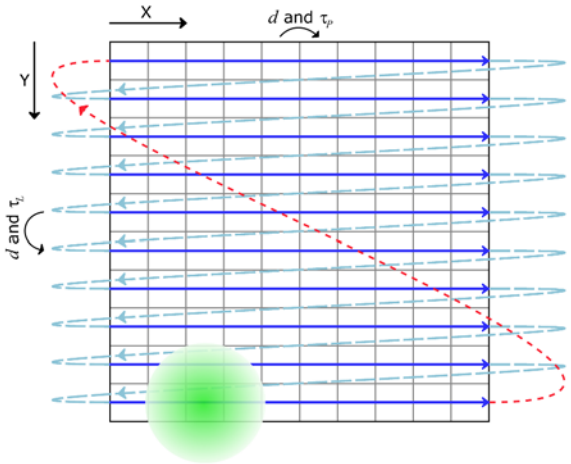

Figure 3.7: Raster-scanning by a CLSM

A CLSM generates an image by scanning pixel by pixel and line by line along an imaginary raster. Adjacent pixels along a scanned line will be a pixel dwell time apart, while adjacent pixels across successive lines will be a line time apart. The latter encompasses the time required to scan the pixels of one line (dark blue), plus the time required to retract the laser beam to the start of the next line (light blue), plus twice the time required to start and stop the linear scanning at both ends of the line. d is the pixel size. The oversampled observation profile is represented by the green disk.

When the SACF is calculated as done for ICS [Eq. (3.40)], for each spatial lag a matching temporal lag can be calculated. This is achieved through introduction of the scan function:

$$\tau(\xi,\psi) = \tau_P \xi + \tau_L \psi \tag{2.79}$$

where ξ and ψ are the spatial lags expressed in number of pixels, respectively along and perpendicular to the scan direction. Due to this time information, the SACF of a CLSM image can considered as a STACF.

The resulting SACF can be analyzed using the overall SACF:

$$g_S(\xi,\psi) = g(\xi,\psi) S(\xi,\psi) \tag{2.79}$$

where $g(\xi,\psi)$ brings into account the diffusion of the fluorescent species and $S(\xi,\psi)$ is the correlation due to the finite size of the scanning laser beam. For 2D diffusion, $g(\xi,\psi)$ can be obtained analogously to Eq. (3.11) through substitution of time by eq. (3.44):

$$g(\xi,\psi) = g(0,0)\left[1+\frac{4D(\tau_P \xi + \tau_L \psi)}{\omega_0^2}\right]^{-1} \tag{2.79}$$

The amplitude of $g(\xi,\psi)$ is still equal to the reciprocal of N. Since the observation profile overlaps several pixels in the XY-plane, an important requisite for RICS, the scanning itself also causes a correlation. This correlation is given for a 2D Gaussian observation area by:

$$S(\xi,\psi) = \exp\left[-\frac{\left(\frac{\xi d}{\omega_0}\right)^2 + \left(\frac{\psi d}{\omega_0}\right)^2}{1+\frac{4D(\tau_P \xi + \tau_L \psi)}{\omega_0^2}}\right] \tag{2.79}$$

3.3.2 Practical aspects

The instrumentation required for RICS is a CLSM. The scanning beam of this microscope is essential to RICS. Knowledge of the exact timing of this process is of course also essential. τ_P can often be found in the control software of the CLSM or in the meta-data of the image. τ_L, on the other hand, is not that easily accessible. However, the relationship between τ_P and τ_L is fixed for a given image resolution and can easily be calculated using a simple formula. For

example, for a Zeiss LSM 510 META and an image with a resolution of 512 × 512, τ_L can be calculated as $1200\tau_P$. The exact formula is of course system type specific.

The unique requirement of a CLSM combined with the widespread use of these systems in life science laboratories make RICS a very attractive technique. However, RICS performed on a CLSM operating in analog requires extra attention. Already in 1993, it was reported that the noise within a scanned image appears to correlate along the scan direction.[94] This correlation of detection noise probably originates from the signal processing of the current generated by the PMT and can be described by a certain time constant.[15] Since this time constant is independent of the scan process, the correlation due to detection noise will span more spatial lags when scanning is fast. For slow scanning, as applied in ICS, this correlation is in general limited to the first spatial lag or might be even absent.

When fitting the SACF to the selected model, the correlation due to detection noise should be remove from the SACF. This is achieved by assigning zero weights to all spatial lags that are affected by this correlation. These pixels are located in the scan direction (X) and the number of spatial lags to be cancelled is called *number of pixels to jump in* X. No general rule can be provided about this number because it is a system specific parameter.[86] When τ_L is the time scale of interest, as for slow moving membrane proteins, the complete ψ = 0 line of the SACF can be removed.[38]

The correlation due to detection noise is dramatically reduced when using a CLSM operating in photon counting mode. As a result, photon counting is advised for studying fast processes which rely on the ψ = 0 line.

In addition to the noise issue, another problem arises which is also observed in ICS. When an image intensity is inhomogeneous, this inhomogeneous background will perturb the SACF. Preventing such a background by only selecting homogeneous areas is the best solution, yet not always possible in biological cells. Therefore, a detrending algorithm is proposed.[25] This algorithm subtracts the average image of a stack from each image in that stack. Subsequently, the average intensity of the average image is added to each

image to keep the denominator during the SACF calculation before and after the detrending constant. In this way, the amplitude of the TACF remains unaffected.

Although the detrending algorithm is often referred to as a removal of the immobile fraction, it needs to be highlighted that a homogeneous distribution of immobile particles would not pose a problem. This situation can be considered as a two species system with D of one of them set to zero. The real problem is a inhomogeneous fluorescence intensity, as might be caused in cells by spatial differences in concentration of the probe. When RICS is applied on a stack of images displaying large intensity differences between subsequent images, it is of no use to correct each image in order to obtain a constant average intensity per image throughout the stack. Multiplication of an image by a constant will not change the SACF since this is the normalized spatial autocorrelation function. However, differences in the amplitude of the SACF can be expected when the intensity variation across the stack is due to a difference in the concentration of the particles.

Finally, the range of diffusion coefficient that can be studied using RICS is bounded by the size of the observation profile and the scan speeds offered by the system. Unless stimulated emission-depletion (STED) is used, the size of the observation profile can be considered as fixed for a given objective and pinhole size. The scan speed of the CLSM is also limited to a number of speeds. The ratio of τ_P to τ_L is also constrained and relies on the resolution of the image. When studying slow moving proteins in the cell membrane of live cells, the slowest scan speed might still be too fast, i.e. τ_L too small. This can be circumvented by performing a line-wise sequential scan in which several images (tracks) are recorded. In this way, each line is scanned as many times as there are tracks before the next line is scanned. In this way, τ_L can be extended. The resulting tracks can be considered as almost identical images. As a result, their SACFs can be averaged.

3.3.3 Validation of RICS using 3D isotropic diffusion

Before applying RICS to study the diffusion of protein in the cell membrane of live cells, the technique was first validated using 175 nm beads dissolved in buffers of various viscosity. To analyze these results an extra factor has to be added to Eq. (3.45):

$$g(\xi,\psi) = g(0,0)\left[1+\frac{4D(\tau_P\xi+\tau_L\psi)}{\omega_0^2}\right]^{-1}\left[1+\frac{4D(\tau_P\xi+\tau_L\psi)}{\omega_z^2}\right]^{-1/2} \qquad (2.80)$$

where ω_z^2 is the axial radius of the 3D Gaussian observation volume.

3.3.3.a *Material and methods*

Fluorescent latex beads (175 nm diameter, PSSpeck microscope point source kit, yellow-green, excitation λ = 505 nm/emission λ = 515 nm) and 120 µm thick adhesive spacers (Secure-seal spacer) were purchased from Molecular Probes (Invitrogen). Raster-scan images were collected with a Zeiss LSM 510 META one-photon CLSM (Jena, Germany, SN 002-11332, installed November 2002; scan parameter values appear to be dependent on the serial number) on an Axiovert 200M motorized frame placed on a vibration isolation table in an air-conditioned room kept at constant temperature. An analog photomultiplier tube (PMT; model is proprietary Zeiss information) was used for detection. Dark signal contributions to the images were effectively zeroed out by setting the proper detection offset value as provided in the Zeiss software.

The fluorescent latex beads were excited with the 488 nm line (selected by an extra 488 ± 10 nm interference-based laser cleanup filter) of the 30 mW air-cooled argon ion laser under the control of an acousto-optical tunable filter (AOTF; set at 1% transmission; 10 µW at the sample position as measured with a Coherent LaserMate Q powermeter (Coherent B.V., Utrecht, The Netherlands)). The excitation light was directed to the sample by a dichroic mirror (DC; HFT 488) and a Zeiss EC Plan-Neofluar 40×/NA 1.3 oil immersion objective. The fluorescence light was sent through the DC and a long-pass LP505 emission filter to the PMT. Images were collected using the Zeiss system control software version 4.0 SP2. The image size was typically set to 512 × 512 pixels, and the zoom factor was set to 8 (54.9 nm/pixel) to ensure that the PSF

contained a sufficiently large number of pixels (radius of 5-6 pixels). The detector gain was set to 900 Zeiss software units.

The axial and lateral radii of the observation profile were determined by performing a z-stack on 175 nm immobilized fluorescent beads, followed by applying the point distiller and data processing Huygens Essential software package (Scientific Volume Imaging, Hilversum, The Netherlands). The obtained intensity profiles in the XY-direction and in the Z-direction were subsequently fit with a Gaussian profile using Matlab (The MathWorks BV, Eindhoven, The Netherlands).

3.3.3.b Results and Discussion

The RICS method was evaluated by performing measurements on 175 nm diameter green fluorescent beads freely diffusing in isotropic solutions of different viscosities (0-56%(w/v) sucrose in 20mM HEPES pH7.2) at 23 °C. To perform RICS measurements, the fluorescent beads were "sandwiched" between a microscope slide and a coverslip, sealed by an adhesive spacer. The resulting microscopic chamber is small enough to eliminate any flow in the solution while retaining a 3D sample environment.[12] Raster-scan images were collected at various scan speeds ranging from a scan speed of 2 (τ_P =102.4 µs; τ_L =122.88 ms) up to a scan speed of 13 (τ_P = 0.57 µs; τ_L = 0.68 ms).

Before performing the correlation analyses, the respective backgrounds were subtracted by applying an overall immobile fraction removal algorithm. Autocorrelation spectra were cropped to 32 × 32 regions and fitted with a 3D free diffusion model (*Figure 3.8*). The results were essentially independent of the initial guesses of the parameter values. As summarized in

Table 3.1, the measured and expected D values according to the Stokes-Einstein equation are well in agreement. For each combination of solute and solvent, the diffusion coefficient was found to be essentially independent of the selected values of τ_P and τ_L within the range indicated above.

Table 3.1: 3D RICS diffusion measurements

RICS was validated using 3D isotropic diffusion of 175 nm fluorescent beads at 23°C in solutions of various viscosities.

Solution	η [$mPa.s$]	τ_P [μs]	τ_L [ms]	D^* [$\mu m^2/s$]	$D_{expected}$[§] [$\mu m^2/s$]
HEPES (5% Tween 20)	0.93	0.8-12.8	0.96-15.36	2.4 ± 0.4	2.7
2% sucrose	0.96	0.57-25.6	0.68-30.72	2.9 ± 0.7	2.6
10% sucrose	1.09	0.91-51.2	1.09-61.44	2.4 ± 0.5	2.3
40% sucrose	1.95	0.8-102.4	0.96-122.88	1.4 ± 0.1	1.3
56% sucrose	3.33	0.57-6.4	0.68-7.68	0.7 ± 0.1	0.7

§ Calculated according to the Stokes-Einstein equation
* Uncertainties are reported as standard errors.

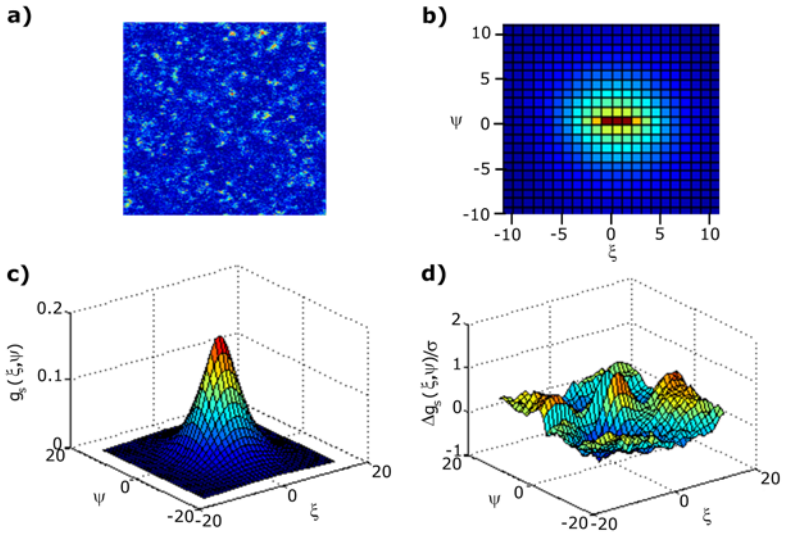

Figure 3.8: RICS measurement of 175 nm beads in 40 % sucrose

a) a 512 × 512 raster-scanned image of subresolution fluorescent beads (175 nm diameter) dissolved in 40% sucrose. b) Top view of the measured SACF. c) The fitted SACF for 3D free diffusion. d) the corresponding weighted residuals. Twenty images were collected at a scan speed of 9. d = 54.9 nm, τ_P = 1.6 µs, and τ_L = 1.92 ms

3.4 Temporal image correlation spectroscopy

Although all ICS techniques can be considered as imaging analogues of FCS, TICS approaches FCS the most. Analogously to FCS, it exploits the intensity fluctuations between regular, consecutive images to describe molecular dynamics.[118]

The spatial resolution introduced through the use of images results unavoidably in a decreased temporal resolution, meaning that fast dynamics are inaccessible to TICS. However, this trade-off is very much improved by the development of fast and highly sensitive electron multiplying charge-coupled device (EM-CCD) cameras.[109] The use of these cameras has extended the accessible maximum diffusion coefficients of 1 $\mu m^2/s$ for a CLSM to 10 $\mu m^2/s$ for a spinning disk confocal microscope or a TIRFM.[109,115]

When studying membranous proteins, the limited temporal resolution of TICS is partially compensated because the dynamics of interest occur on time scales of ms to s. These time scales are difficult to monitor via traditional FCS. Moreover, the use of images allows one to probe up to 10^5 locations simultaneously (*Figure 3.9*).[115] Even if FCS could be applied to membrane protein diffusion in intact, biological cells without technical artifacts, the relative long characteristic fluctuation time would lead to extended measurement times owing to the square root dependence of the FCS signal-to-noise ratio on the number of sampled fluctuations.[62,100,134] In conclusion, the parallel sampling inherent to TICS allows to measure membrane protein dynamics with an acceptable signal-to-noise ratio in relatively shorter periods of time.

Originally, TICS was applied using a CLSM,[134] but a TIRFM equipped with an EM-CCD offers a better time resolution.[60,109] Due to its analogies with TIR-FCS, this approach is also called ITIR-FCS (imaging TIR-FCS). The thin detection volume features an excellent surface selectivity while efficiently rejecting a cytoplasmic background when measuring in cellular membranes.[102]

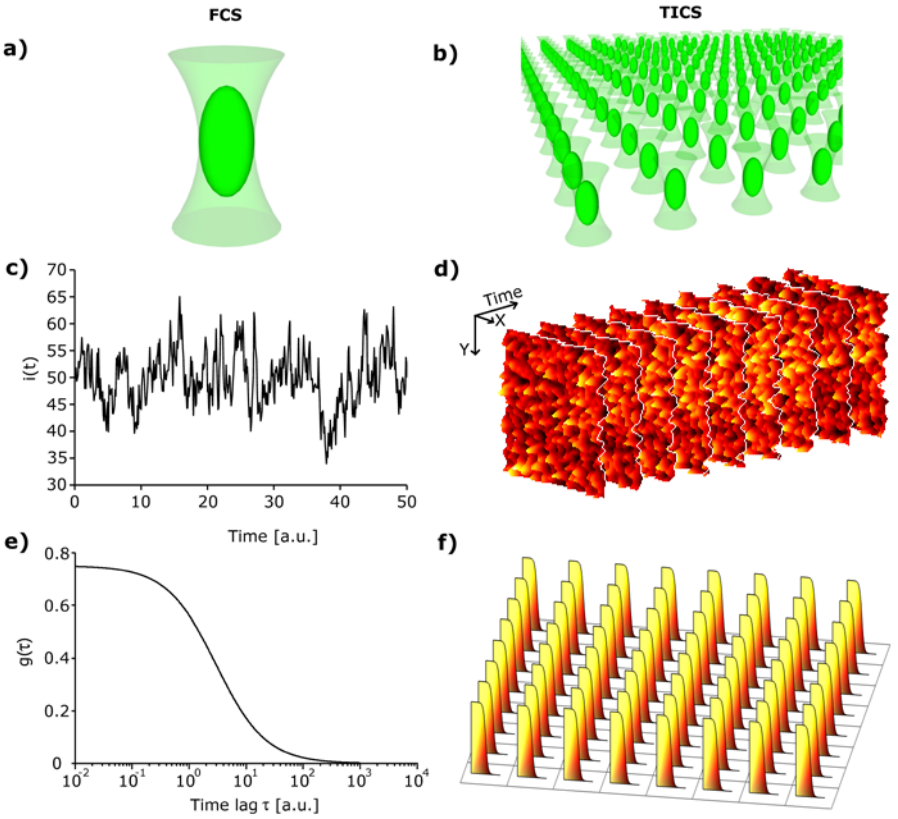

Figure 3.9: Analogies between FCS and TICS

TICS can be considered as a multiplex FCS experiment in which the single observation volume (a) is substituted by an array of up to 10^5 observation volumes (b, pictorial representation). The fluorescence intensity time series of FCS (c) is consequently replaced by a time series of images (d). Each pixel location in this time series can yield an ACF (f) which can all be averaged to obtain a single ACF as in FCS (e).

3.4.1 Temporal autocorrelation function

TICS entails the calculation of the temporal ACF (TACF) analogous to the ACF as used in FCS. The TACF is also a special case of the STACF by implementing zero spatial lags ($\xi = 0$ and $\psi = 0$). As a result, Eq. (3.38) reduces to

$$g(0,0,\tau) = \left\langle \frac{\langle \delta i(x,y,t)\, \delta i(x,y,t+\tau) \rangle_{XY}}{\langle i(x,y,t) \rangle_{XY} \langle i(x,y,t+\tau) \rangle_{XY}} \right\rangle_T \qquad (2.81)$$

Using the equation above, the fluctuations are first averaged in the spatial domain followed by a temporal averaging over the stack of images.

The TACF is essentially the temporal persistence of the average spatial cross-correlation between two images in a time series separated by a time delay τ. Originally, the normalized spatial cross-correlation was calculated for each possible combination of images using FFT methods, of which only the zero spatial lags value was used.[118] The disuse of non-zero spatial lags together with the increased number of images that came with the improved acquisition rate, have led to a more straightforward and faster approach: direct calculation of exclusively zero spatial lags values as a function of the time lag in the image series.[134] The recorded time series of images is discrete in both space and time and this enables the discrete approximation of Eq. (3.46), yielding a vector that holds for each lag time a single, average value:

$$g_C\left(0,0,\tau\right)=\left\langle \frac{\left(1/XY\right)\sum_{n=1}^{X}\sum_{m=1}^{Y} i\left(x_n,y_m,t\right)i\left(x_n,y_m,t+\tau\right)}{\left(1/XY\right)^2\left[\sum_{n=1}^{X}\sum_{m=1}^{Y} i\left(x_n,y_m,t\right)\right]\left[\sum_{n=1}^{X}\sum_{m=1}^{Y} i\left(x_n,y_m,t+\tau\right)\right]}\right\rangle_T \tag{2.82}$$

The evaluation time of this expression scales roughly with the square of the number of frames included in the time series. Originally, this number was limited to 300 frames or less.[59,134] For larger time series, either due to an increased frame rate or due to an elongated acquisition time, the computation time becomes impractically large. A solution is to evaluate the expression only for logarithmically spaced time lags, as applied in FCS and line-scan FCS.[103,110,124]

3.4.2 TACF interpretation

For pixel sizes considerable smaller than the observation profile, the obtained TACF is fitted to an expression similar to Eq. (3.11), but extended with an extra constant offset term g_∞:

$$g\left(0,0,\tau\right)=\boldsymbol{g\left(0,0,0\right)}\left[1+\frac{\tau}{\boldsymbol{\tau_D}}\right]^{-1}+\boldsymbol{g_\infty} \tag{2.83}$$

Where parameters printed in bold are optimized during the fit routine. In the literature, g_∞ is used as a measure of the immobile fraction present in the sample.[59] However, in practice it can arise from a number of sources which will be discussed in a dedicated section.

D can be obtained from τ_D by means of Eq. (3.12). This conversion requires exact knowledge of the dimensions of the observation area. Any uncertainty in ω_0 will propagate into an increased uncertainty in D. In FCS, this problem is tackled through calibration measurements using a standard solution of a fluorochrome with a well-documented D. However, this is not possible for TICS because D for 3D diffusion is often too high to be measured by TICS. To cope with this problem, an ICS analysis is performed on the time series of images. The average e^{-2} radius $\langle \omega_{0,t} \rangle$ throughout the stack is subsequently used as the estimate of ω_0.

The expected value of ω_0 can be calculated using the emission wavelength λ_{em} of the fluorochrome and the numerical aperture (NA) of the objective:[141]

$$\omega_0 = 2\sigma_0 = \frac{0.42\lambda_{em}}{NA} \tag{2.84}$$

where σ_0 is the radius of the observation profile at e^{-1} of its maximum intensity, i.e. the standard deviation of the 2D Gaussian profile. For an experiment using AlexaFluor 488 (λ_{em} = 519 nm) as fluorochrome and an objective with a high NA of 1.45, ω_0 = 150 nm. This value is significantly smaller than reported for $\langle \omega_{0,t} \rangle$ in the literature (ω_0 close to 400 nm).[59] This discrepancy might be explained in part by diffusion of the particles during image acquisition.[109] Addition in quadrature of σ_0 and the root mean squared displacement of a particle during acquisition time t_{acq} ($\sqrt{4Dt_{acq}}$) yield a better estimate of the dimensions of the observation profile:[109]

$$\sigma_0' = \sqrt{\left[0.21\lambda_{em}/NA\right]^2 + 4Dt_{acq}} \tag{2.85}$$

For the given experimental case, D = 0.1 $\mu m^2/s$ will lead to an increased radius of the observation profile of 320 nm. Although Eq. (3.50) has experimentally been demonstrated to be a good estimator of the size of the observation profile,[109]

the contribution of diffusion during the image acquisition is much smaller due to the accumulation of the signal during t_{acq}. Other factors broadening ω_0 are the axial position of the sample in the observation volume and the finite pixel size.[9,102] The increased σ_0' due to the finite pixel size can be calculated as:[119]

$$\sigma_0' = \sqrt{\sigma_0^2 + d^2} \tag{2.86}$$

where d is the side length of a pixel.

Recently, a workaround has been introduced to perform TICS measurements independent of the optical point spread function of the system.[44,52,53] The assumption of a Gaussian observation profile is actually only valid for circular pinholes much smaller than the Airy disk.[102] Each pixel of the CCD camera works essentially as a square pinhole. The resulting observation profile is the convolution of the image of the square pinhole in sample space with the point spread function of the objective.[102] Bringing this observation profile into account, the TACF for square pixels is given by:[102,109]

$$g(0,0,\tau) = \frac{1}{N}\left[erf(\varphi) + \frac{1}{\sqrt{\pi}\varphi}\left(e^{-\varphi^2} - 1\right)\right]^2 \tag{2.87}$$

where $\varphi = \frac{a}{\sqrt{4D\tau + \omega_0^2}}$ and $a = d$. The particle density can be calculated using a^2 as the effective observation area. It is advised for small pixels ($a < 2\omega_0$) to use Eq. (3.52) instead of Eq. (3.48) and to optimize ω_0 as a free parameter.[109] It has been shown that for large square pinholes ($a > 3\omega_0$), the contribution of ω_0 can be neglected.[53] This situation can be obtained by performing a symmetrical binning of the images ($a = n_b d$, n_b is the number of pixels binned in each direction).[44] In this way, determination of D depends on the pixel size that can be measured unambiguously. The drawback of this approach is its association with a longer τ_D due to the larger observation area and the concomitant longer measurement time.

3.4.3 Statistical accuracy

The statistical accuracy of TICS measurements is largely determined by two parameters: NIF and acquisition time. The accuracy is linearly proportional to the square root of both parameters. This means that a short acquisition time can, to a certain extent, be compensated by the resolution of the image. This is the key improvement of TICS over FCS: parallel sampling.[134] Other factors that influence the accuracy are already mentioned for FCS and include the brightness of the fluorescent particles.

As demonstrated for FCS, bringing into account the standard deviation of the ACF during the fit will yield more accurate parameter estimates. However, calculation of the standard deviation of the TACF as obtained in TICS using the spatial average is not described to the same extent as for FCS. However, since the TACF is calculated as the average of the TACFs obtained from the pixel positions included in the analysis, their standard deviation can also be calculated. Yet, for long acquisition times, the large number of data points at longer time lags will disturb the fit. The use of logarithmically spaced time lags circumvents this problem and avoids an arbitrary cutoff.

The minimal acquisition rate was also studied as a function of τ_D using computer simulations.[59] Above a minimal frame rate of two images per τ_D, no significant improvement was observed.[59] This again highlights that, above a certain level, the accuracy of the ACF can only be improved by increasing the number of observed independent fluctuations.[107] The criterion of a minimal frame rate of two frames per τ_D delineates the maximum D that can be observed using TICS.

Finally, the background noise has to be brought into account. Otherwise, the occupation number can be overestimated. To cope with this problem, the correction [Eq. (3.32)] as introduced for FCS can be used. A more frequently applied approach is to subtract this constant offset from the images prior to further analysis.[59,109]

3.4.4 Effect of photobleaching

In the presence of photobleaching, one can expect an apparently higher D. In addition to leaving the observation area by diffusion, an extra pathway to

disappear from this area exists when photobleaching occurs. Furthermore, the decreasing number of fluorescent particles will lead to an increase of the TACF amplitude.[23]

The problem can be divided into two aspects: correct calculation of the TACF on one hand and its correct interpretation on the other.[23] For FCS, where a time average is used, the calculation of the ACF is incorrect. The time average will no longer be representative for the ensemble average due to the decreasing fluorescence intensity over time. Two frequently applied solutions are piecewise analysis of the fluorescence intensity time series or a correction of the fluorescence intensity over time prior to ACF calculation.[23] Although both methods allow for the correct calculation of the ACF, they do not correct for the decaying concentration of the fluorescent species. The ACF in the presence of photobleaching, $g_{pb}(\tau)$, can be corrected for a decaying N by:[23]

$$g(\tau) = g_{pb}(\tau)\left\langle\left[\langle b(t)\rangle\langle b(t+\tau)\rangle\right]^{-1/2}\right\rangle^{-1} \tag{2.88}$$

where $b(t)$ is the time course of N during the measurement normalized to the initial occupation number N_0. For photobleaching, $b(t)$ often results in a mono- or bi-exponential decay.

TICS measurements will also be affected by photobleaching. However, in contrast to FCS, TICS estimates the ensemble average through a spatial average.[‡] When each position in the sample experiences identical bleaching, this approach will remain valid. As a result, only the correction of the TACF should be considered.

It has been shown that a correction similar to Eq. (3.53) is also possible for TICS.[59] However, the final expression does not bring τ into account. Based on Eq. (3.53) it is reasonable to assume that this might lead to small errors, especially when $\tau << T$. Therefore, the problem is reconsidered.

The average, spatial image intensity can be expressed in terms of the average occupation number and the brightness of the fluorescent species:

[‡] *For TICS utilizing the time average, an elegant correction for photobleaching can be obtained through modification of the correction applied by Ries et al. (2009) for line-scan FCS. This required modification is the inclusion of non-Poissonian detection noise and its system-specific noise parameters.*

$$\left\langle i(x,y,t)\right\rangle_{XY} = \varepsilon \left\langle N(x,y,t)\right\rangle_{XY} \tag{2.89}$$

where N is now assumed to be a function of space and time. To bring into account the fluctuation in each pixel, the pixel intensity $i(x,y,t)$ can be written as:

$$i(x,y,t) = \varepsilon \left\langle N(x,y,t)\right\rangle_{XY} + \vartheta(x,y,t)\,\varepsilon\sqrt{\left\langle N(x,y,t)\right\rangle_{XY}} \tag{2.90}$$

where $\vartheta(x,y,t)$ represents the normalized thermodynamical fluctuation[23] related to $\left\langle N(x,y,t)\right\rangle_{XY} = 1$, i.e. $\left\langle \vartheta(x,y,t)^2 \right\rangle_{XY} = 1$.

Substitution of Eq. (3.54) and Eq. (3.55) into Eq. (3.36) yields the intensity fluctuations around the average:

$$\delta i(x,y,t) = \vartheta(x,y,t)\,\varepsilon\sqrt{\left\langle N(x,y,t)\right\rangle_{XY}} \tag{2.91}$$

Based on this definition, the TACF can be calculated using Eq. (3.38):

$$\begin{aligned} g(0,0,\tau) &= \left\langle \frac{\left\langle \vartheta(x,y,t)\,\varepsilon\sqrt{\left\langle N(x,y,t)\right\rangle_{XY}}\,\vartheta(x,y,t+\tau)\,\varepsilon\sqrt{\left\langle N(x,y,t+\tau)\right\rangle_{XY}} \right\rangle_{XY}}{\varepsilon\left\langle N(x,y,t)\right\rangle_{XY}\,\varepsilon\left\langle N(x,y,t)\right\rangle_{XY}} \right\rangle_T \\ &= h(0,0,\tau)\left\langle \frac{\sqrt{\left\langle N(x,y,t)\right\rangle_{XY}}\sqrt{\left\langle N(x,y,t+\tau)\right\rangle_{XY}}}{\left\langle N(x,y,t)\right\rangle_{XY}\left\langle N(x,y,t)\right\rangle_{XY}} \right\rangle_T \\ &= h(0,0,\tau)\left\langle \frac{1}{\sqrt{\left\langle N(x,y,t)\right\rangle_{XY}}\sqrt{\left\langle N(x,y,t+\tau)\right\rangle_{XY}}} \right\rangle_T \end{aligned} \tag{2.92}$$

where $h(0,0,\tau) = \left\langle \left\langle \vartheta(x,y,t)\,\vartheta(x,y,t+\tau)\right\rangle_{XY} \right\rangle_T$.

Since it is assumed that all pixels experience an identical bleaching, $\left\langle N(x,y,t)\right\rangle_{XY}$ can be expressed as the product of the initial spatial average occupation number N_0 with a bleach function $b(t)$ [$b(0)=1$]:

$$\left\langle N(x,y,t)\right\rangle_{XY} = N_0 b(t) \tag{2.93}$$

Eq. (3.58) can subsequently be expressed in terms of N_0 and $b(t)$:

$$g_{pb}(0,0,\tau) = \frac{h(0,0,\tau)}{N_0}\left\langle\left[b(t)b(t+\tau)\right]^{-1/2}\right\rangle_T = g(0,0,\tau)\left\langle\left[b(t)b(t+\tau)\right]^{-1/2}\right\rangle_T \tag{2.94}$$

In comparison with Eq. (3.53), not the product of the time averages but the time average of the product is used. The TACF corrected for photobleaching can thus be obtained as:

$$g(0,0,\tau) = \frac{g_{pb}(0,0,\tau)}{\left\langle\left[b(t)b(t+\tau)\right]^{-1/2}\right\rangle_T} \tag{2.95}$$

Although $b(t)$ is assumed to be a decaying function in case of photobleaching, it can be any function representing a general trend in the observed occupation number during the measurement.

The effect of a mono-exponential bleaching with various bleaching rates was investigated, highlighting the robustness of the correction.[59] Unfortunately, the results were limited to specific experimental conditions. Therefore, the limitations of the correction are revised here.

The correction relies essentially on the fluctuations of the remaining fluorescent particles. It is reasonable to assume that the correction fails when all fluorescence is bleached. Furthermore, deviations will start to arise when the fractional intensity drops below 1/N. As a result, higher densities will allow for a better bleach correction.

The effect of the bleach rate was studied by us by using computer simulations. Stacks of 4000 images were simulated with a density of 10 $particles/\mu m^2$, 512×512 resolution, ω_0 = 400 nm and d = 80 nm. D was set to 0.1 $\mu m^2/s$ and the interval between frames was kept constant at $\frac{1}{4}\tau_D = 0.1\,s$. The effect of the finite pixel size was ignored. The bleaching was applied as a mono-exponential:

$$b(t) = e^{-kt} \tag{2.96}$$

where k is the bleaching decay constant with reciprocal time units. k ranged from 0 to 1 s^{-1}. Each stack of images was analyzed repetitively while varying the number of frames included in the analysis. The analysis comprised calculation of

the TACF, fit of the fluorescence decrease with a mono-exponential including a constant offset, correction of the TACF according to Eq. (3.60) and fit of both the original and corrected TACF [*Figure 3.10*].

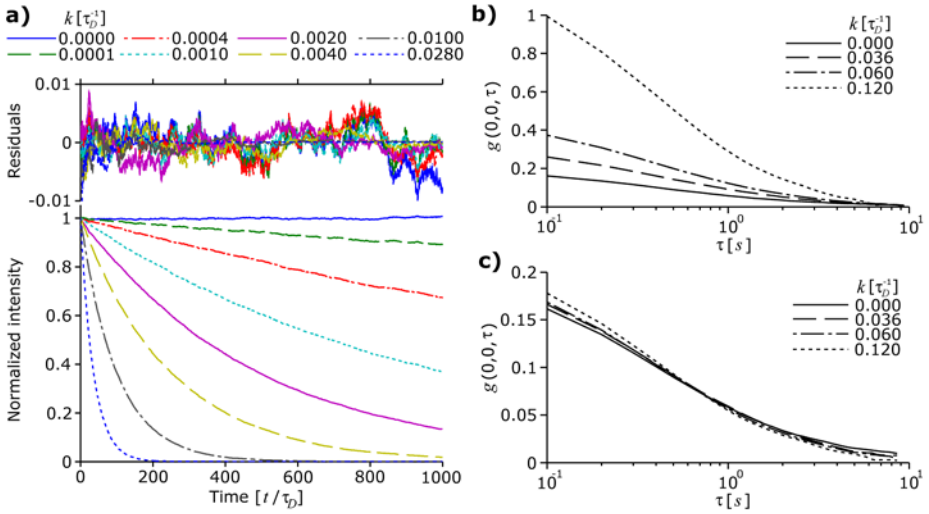

Figure 3.10: Exemplar curves for simulated fluorescence decrease and TACF

a) Time course of fluorescence for eight different stacks of simulated images. The bleaching rate k is expressed as the reciprocal of τ_D for generality. The unweighted residuals between the fit of the decay and the simulated values are shown in the top left panel. b) The TACF of the first 100 frames associated with four different bleaching rates. The difference in amplitude is obvious. c) identical TACFs as in b), but corrected using the method described above [Eq (3.60)*].*

The normalized deviation of the obtained results in comparison to the simulation parameters where subsequently plotted as a function of bleaching rate and the number of frames included in the TACF calculation [*Figure 3.11*]. It is obvious that an increasing number of frames included in the analysis has a negative effect on the recovery of both the occupation number and τ_D. This is in contrast with the situation in absence of photobleaching, where the uncertainty on the recovered parameter values is reduced by increasing the number of frames included in the analysis.

As expected, N is underestimated for high k. The bleach correction extends the range of bleach rates that can still be tolerated by about one decade. For τ_D, in contrast, no obvious improvement is detected by applying the bleach correction. The simulations show an increase of τ_D with increasing k.

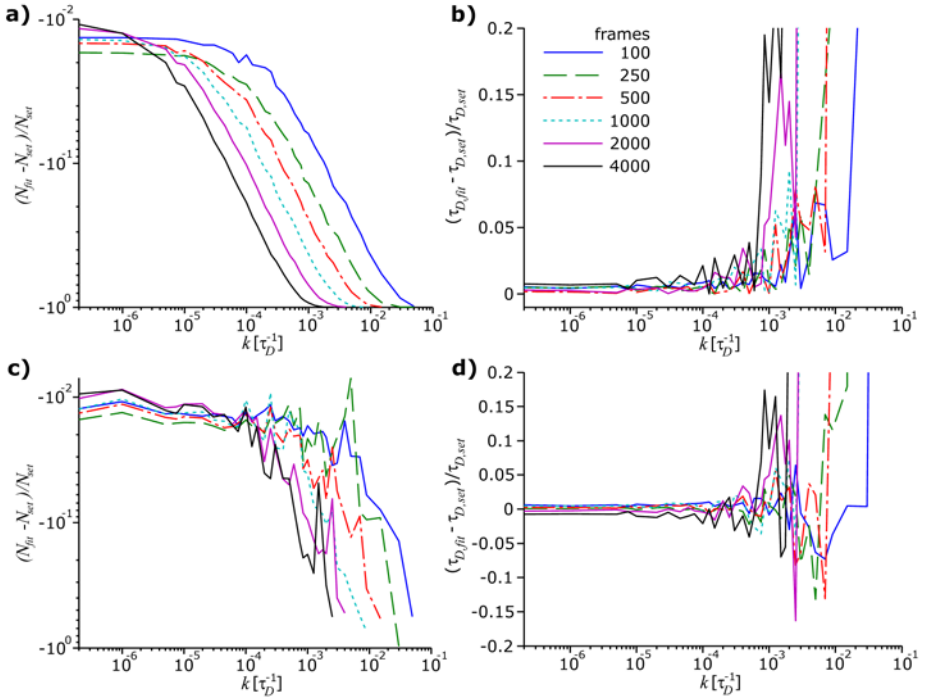

Figure 3.11: Graphical representation of the deviation on the retrieved parameters

The TACFs of the simulated data sets were fit and normalized deviations were plotted as a function of k. The analyses also included six different numbers of frames, each depicted in a different color. (a) For uncorrected TACFs, the occupation number is underestimated for large k, which is further aggravated when more frames are included in the analysis. (b) The bleach correction reduces the deviation and extends the bleaching range that still allows for a correct analysis. (c) and (d) show the result for τ_D as a function of k obtained from respectively uncorrected and corrected TACFs. Also here, the effect of the number of included frames is obvious. The correction, however, does apparently not result in a reduction of the error for large k.

The number of frames included in the analysis determines the maximum k that can be corrected for. Since this number depends on experimental settings, the simulation are further generalized by plotting the result as a function of the amount of fluorescence that is lost during the acquisition [*Figure 3.12*]. These results demonstrate that the underestimation of N is independent of k and depends solely on the loss of fluorescence during the acquisition. Again, the bleach correction reduces the normalized error by one decade. Also for τ_D, an increase in the loss of fluorescence aggravates the error, which again cannot be corrected by the bleach correction method.

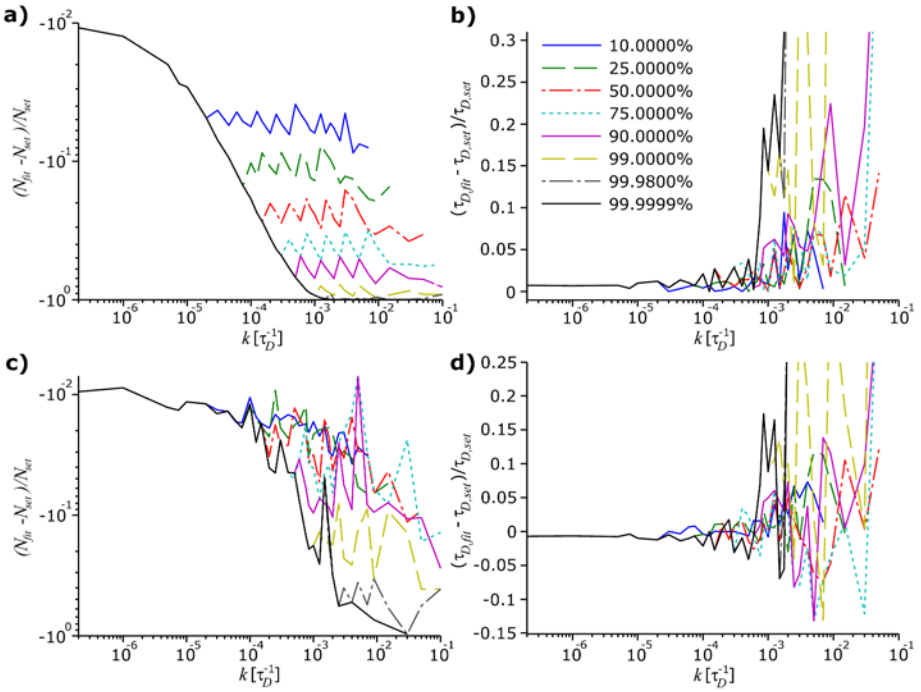

Figure 3.12: Deviation on the retrieved parameters as a function of lost fluorescence

The normalized deviations were plotted as a function of k. Instead of considering the number of frames included in the analysis, the fluorescence intensity was used as a criterion to determine this number. The black curve indicates the limit of the analysis, which is 4000 frames. (a) For uncorrected TACFs, the underestimation of the occupation number increases with increasing loss of fluorescence. This is constant for all k. (b) The bleach correction reduces the normalized deviation by one decade. (c) and (d) show the result for τ_D as a function of k obtained from respectively uncorrected and corrected TACFs. Also here, an increasing loss of fluorescence will deteriorate the obtained result. The correction, however, does apparently not result in a reduction of the error for large k.

Based on these results, it is obvious that the loss of fluorescence during the acquisition has to be minimized. For high bleaching rates, a solution can be found by limiting the number of frames included in the analysis. A loss of fluorescence less than 50% yields, after correction, parameter estimates with less than 10 % of normalized errors for high *k*. Unfortunately, this approach has a tradeoff. By reducing the number of frames the number of observed τ_D will also decrease, leading again to an increase of the uncertainty (see *Statistical accuracy* above).

3.4.5 g_∞ : indicator for immobile fraction?

It is obvious that TICS benefits from the preceding years of development of FCS. However, when it comes to the analysis of specimens holding an immobile species in addition to the species of interest, TICS can no longer mimic FCS in its approach. Prior to the actual FCS measurement, the immobile species within the observation volume is bleached during the first few seconds of exposure to the parked laser beam. This removes the fluorescence contribution of the immobile species from the remaining intensity trace and reduces the problem to a regular FCS measurement. The mobile fraction within the small observation area will also be affected in this initial phase, but the mobile fraction of the surrounding reservoir will be largely unaffected. As a result, the mobile molecules are continuously replaced.

A similar bleaching approach applied in TICS would deplete a large part of the total fluorescence of interest because the observation area spans the total bottom membrane of the biological cells and not just a diffraction limited spot. Moreover, the replacement of the bleached, mobile particles in this area by fresh ones will take a long time.

The type of average utilized to define the fluctuations in TICS has important consequences concerning the immobile fraction. When the time average is used [Eq. (3.34)], the intensity contribution of the immobile species will not fluctuate. As a result, this fraction will not correlate and its contribution is comparable to the noise contribution [Eq. (3.32)]. As a result, the presence of an immobile fraction will only influence the amplitude of the TACF, but not its shape. When the magnitude of the immobile fraction is known, the correct $g(0,0,0)$ can be calculated. However, this information cannot be obtained from the measurement itself. If the influence of an immobile fraction is ignored, the amplitude can considerably be underestimated, finally leading to an overestimation of the concentration. It is important to note that some publications erroneously define the fluctuations in TICS using a time average while they do detect an immobile species.[59,135]

The case of an immobile fraction dramatically changes when calculating the fluctuations using the spatial average [Eq. (3.36)]. Each immobile fluorescent species can now be considered to generate fluctuations around the spatial

average intensity. This is obvious, because TICS assumes that all particles are fixed during the acquisition of a single image. However, the difference between immobile and mobile particles arises when considering the temporal correlation of these spatial fluctuations, as performed in TICS. For mobile species, this correlation will decay as predicted by Eq. (3.48). The correlation of the immobile species, on the other hand, will be constant. This can be illustrated by inserting an increasing τ_D (corresponding to a decreasing D) into Eq. (3.48), eventually leading to a constant amplitude.

When a mixture of mobile and immobile species is studied, the latter will cause a constant offset. As a result, g_∞ [Eq. (3.48)] can be considered an indicator of the immobile species. The percentage of immobile species can subsequently be calculated by:[59,135]

$$\%\ immobile = 100\frac{g_\infty}{g_\infty + g(0,0,0)} \tag{2.97}$$

This can be demonstrated by considering Eq. (3.26) for two species of equal brightness. Although this approach is correct (as long as both mobile and immobile species have identical brightness), its interpretation in the literature is not always correct. g_∞ is used to calculate the absolute number of immobile particles, thereby assuming that this species has indeed equal brightness.[135] However, the concentration obtained for both the immobile and mobile species will be an overestimation of the true concentrations.

To obtain the correct concentrations, Eq. (3.25) for multiple species should be used. When assuming equal brightness, this equation can be reduced to:

$$g(0,0,\tau) = \frac{\sum_{j=1}^{n}\left[N_j u_j(\tau)\right] + N_{im}}{\left\{\sum_{j=1}^{n}\left[N_j\right] + N_{im}\right\}^2} \tag{2.98}$$

where N_{im} is the occupation number of the immobile species, N_j the occupation number of the j^{th} mobile species and u_j is the TACF of the j^{th} mobile species for $N_j = 1$. The mobile fraction M can be expressed as the ratio of mobile particles to the total number of particles (N_{tot}):

$$M = \sum_{j=1}^{n} N_j \Big/ N_{tot} \tag{2.99}$$

Eq. (3.63) can subsequently be written as:

$$g(0,0,\tau) = \frac{\sum_{j=1}^{n}\left[N_j u_j(\tau)\right] + \frac{1-M}{M}\sum_{j=1}^{n}\left[N_j\right]}{\left\{\frac{1}{M}\sum_{j=1}^{n}\left[N_j\right]\right\}^2} \tag{2.100}$$

In the presence of only one mobile species with occupation number N, Eq. (3.65) further reduces to:

$$g(0,0,\tau) = \frac{Mu(\tau)+1-M}{N/M} \tag{2.101}$$

When the contribution of the immobile fraction to the amplitude of the TACF is ignored, the term 1-M in the numerator disappears and the apparent occupation number N' is set to equal the reciprocal of that part of the TACF amplitude that is only due to the mobile species:

$$N' = \frac{1}{g(0,0,0)} = \frac{N}{M^2} \tag{2.102}$$

In conclusion, the error in the occupation number obtained while ignoring the immobile species, scales with the inverse of the square of the mobile fraction. This can be reformulated as [*Figure 3.13*]:

$$\log\left(\frac{N'}{N}\right) = -2\log(M) \tag{2.103}$$

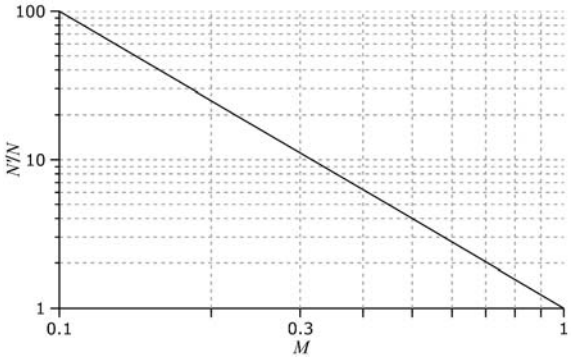

Figure 3.13: Overestimation of N as a function of the mobile fraction

The overestimation of the occupation number N scales with the square of the mobile fraction M when the immobile species is ignored.

Unfortunately, g_∞ not necessarily finds its origin in the presence of an immobile species. This offset comprises any non-zero correlations at large time lags due to the finite measurement time.[59,109] This effect can be minimized by increasing the recording time. Yet, there is still another effect that is currently absent in the literature. In addition to an immobile species, any bright structure, sharp edges or gradients within the analysis region will generate a constant offset. This is because they also can be considered as fixed fluctuations around the mean. Presence of these items further complicates the analysis due to the complex addition of the resulting correlations. Similar problems are encountered by RICS and ICS.

A simple solution to this problem is to select a region devoid of these structures and gradients. When this solution is not possible, the spatial resolution has to be sacrificed to obtain smaller analysis regions in which the gradient can be ignored.[134] The concomitant increase in the uncertainty in the estimated parameters can be compensated by increasing the measurement time. The minimal dimensions of the analysis region are defined by the observation area: the analysis region should include at least a few observation areas (see NIF in *Statistical accuracy of ICS*) to get a reliable estimate of the ensemble average.

3.5 Other members of the ICS family

All techniques discussed in this chapter employ the ACF (either spatial, temporal or a combination of both) to obtain the information of interest of the studied sample. The use of the cross-correlation function (CCF) can further expand the capabilities of the ICS family. Members utilizing the CCF are often denoted with a double C (ICCS, TICCS, RICCS, …). The use of the CCF to study diffusion and directed motion (flow) has readily been demonstrated and, at least equally important, appropriate software is made available since the end of 2010.[47,109,110]. The advantage of CCF in this context is that the CCF between two regions at a known distance of each other can be analyzed. This distance relies only on the correct calibration of the pixel size – which is easy to achieve – and minimizes the effect of the observation profile.[109] In this sense, it can be thought of as the imaging analogue of two-focus FCS in which the CCF between two observation volumes at a well-known, fixed distance is used.[24] k-space ICS (kICS), yet another member, is also developed to measure diffusion, and offers the advantage that it is insensitive to bleaching and blinking artifacts.[60]

In addition to the diffusion and flow measurements, CCF can also be used to study protein interactions.[21,134] The only requisite on top of the preconditions of the regular correlation methods is that both putative binding partners can be separated into two channels. The basis of this separation is often a difference in emission wavelength, which is obtained by a differential labeling of the potential binding partners. Finally, ICCS has been shown to outperform standard co-localization algorithms with a high dynamic range, while also returning accurate number densities of interacting populations.[19]

A more detailed discussion of the ICS family can be found elsewhere.[61,109]

3.6 Discussion

ICS, RICS and TICS are related to FCS. As a result, they have some fundamental properties in common. First, the amplitude of the obtained autocorrelation function is proportional to the inverse of the occupation number. For multiple species, each species contributes by the square of its relative fluorescence contribution. Analysis of the amplitude can therefore be used to estimate the concentration of the species. Secondly, the statistical accuracy of these techniques is largely determined by the number of fluctuations that are measured.

ICS, RICS and TICS offer also some advantages over FCS. ICS allows for determination of aggregation states, even of immobile molecules. RICS has the advantage that it can be applied on any commercial CLSM. Furthermore, RICS can simultaneously measure dynamics and render images of specimens. Finally, TICS can be considered as many FCS experiments in parallel, which improves the signal-to-noise ratio.

Glycine receptor 4

A differential expression of GlyR α_3 splice variant *L* and *K* is reported in the hippocampus of patients suffering from severe TLE.[31] In the hippocampus of healthy people, GlyR α_3 *L* is the predominant variant, the majority of them located extra-synaptically.[31] The small fraction that resides in a synapse is preferentially located at glutamatergic nerve endings.[31].

Interestingly, a remarkable difference exists between both splice variants concerning their aggregation state. While extra-synaptic GlyR α_3 *K* exhibits a diffuse distribution, distinct clusters are formed by its longer counterpart.[31] Moreover, evidence supports a gephyrin-independent cluster mechanism.[31] Due to the described relationship between receptor clustering and receptor desensitization kinetics,[70] clustering can modulate receptor functioning. Therefore, investigating the origin of this clustering might reveal a new regulation of signal transduction.

The first issue that is addressed here concerns the number of GlyR α_3 *L* receptors that resides, on average, in a cluster. Secondly, the diffusion dynamics of the GlyR α_3 are investigated in live cells. Both items are studied using haemagglutinin(HA)-tagged GlyR α_3 *L* and *K* expressed in HEK 293T cells.

4.1 Materials and methods

4.1.1 Cell culturing conditions

Human embryonic kidney 293 T cells (HEK 293T) were maintained at 37°C in a humidified incubator at 5% CO_2 in Dulbecco's modified eagle's medium (Gibco BRL, Paisley, UK) supplemented with 10% fetal calf serum and a penicillin (100 IU/ml)-streptomycin (100 µg/ml) mixture. The cells used for microscopic observation were plated two days before the experiment in 8-well Lab-Tek™ II chambered coverglass (#1.5; Nalge Nunc International, Rochester, NY, USA) seeded at a density of 20 000 cells per well in transfection medium. This is Dulbecco's modified eagle's medium (Gibco BRL, Paisley, UK) supplemented with 10% fetal calf serum but without the penicillin/streptomycin mixture.

4.1.2 Transfection

24 hours after plating, the cells were transfected using calcium phosphate precipitation. Plasmids encoding for HA-tagged human GlyR α_3 *L* (*HA-GlyRα_3L*) and GlyR α_3 *K* (*HA-GlyRα_3K*) were kindly provided by Professor J. Meier (RNA Editing and Hyperexcitability Disorders Helmholtz Group, Max Delbrück Center of Molecular Medicine, Berlin, Germany).[31,87] The HA-tag is located in the extracellular N-terminal domain between amino acids 35 and 36.[31] The plasmids were diluted in 250 mM $CaCl_2$ buffer at a concentration of 20 ng/µl and an equal amount of HEPES buffered saline solution (HBS, pH 7.05) buffer was gently added. After 15 minutes incubation, this buffer was added to the culture medium of the cells. For transfections in 8-well Lab-Tek™ II chambered coverglasses, a final amount of 0.15 µg DNA was added per well. For transfection of cells in small culture flasks (25 cm^2), a final amount of 2 µg DNA was added. After 6 hours, the transfection medium was replaced with transfection medium holding 200 nM strychnine. All measurements occurred within 24 to 36 hours after transfection.

4.1.3 Western blot

3 million cells were plated in small culture flasks for *HA-GlyRα_3L*, *HA-GlyRα_3K* and wild type (WT). Transfection of the cells (except for WT) occurred as described above. After 24 hours of transfection, cells were rinsed with cold (4°C) PBS and trypsinated. The cell suspensions were centrifuged and rinsed again with PBS. After a second centrifugation step, cells were lysed by addition of RIPA buffer (Sigma-Aldrich). Protein concentrations were determined using the BCA™ Protein Assay kit (Pierce,). For each condition, 10, 25 and 50 µg of total protein content was subjected to precast 8% Novex® Tris-Glycine gel electrophoresis usin an XCell SureLock™ Mini-Cell. The proteins were subsequently transferred onto a nitrocellulose transfer membrane via the iBlot™ Dry blotting System (Invitrogen/Molecular Probes). After blocking with 2% non-fat milk in PBS (overnight at 4°C), the membranes were incubated with mAb4a (1:500, Synaptic Systems) followed by secondary antibody rabbit anti-mouse-HRP (Dakocytomation). The bands were finally visualized using a DAB kit (Sigma-Aldrich, Bornem, Belgium)

4.1.4 Electrophysiological recordings

Cells were seeded in 35 mm dishes. Transfection occurred as described above. Whole-cell patch-clamp recordings were performed. The standard extracellular solution for HEK cells (HES) had a composition of (in mM) 150 NaCl, 5.4 KCl, 2 $CaCl_2$, 1 $MgCl_2$, 10 HEPES, and 10 glucose (Sigma-Aldrich, Bornem, Belgium). The intracellular solution (HIS) contained (in mM): 120 CsCl, 2 Na_2ATP, 2 MgATP, 10 EGTA, and 10 HEPES. To measure the dose-response to glycine, different glycine concentrations (1 µM, 10 µM, 30 µM, 100 µM, 300 µM and 1 mM) in HES were applied onto the cell surface during 10 s at an holding potential of -60 mV. The average maximum current as a function of concentration was fit to the *Hill* equation to yield the EC_{50} of both splice variants.

The desensitization of the responses was measured by fitting a mono-exponential to the desensitization phase of the glycine response. The recordings were performed by Dr. D. Janssen (BIOMED, Universiteit Hasselt, Diepenbeek, Belgium).

4.1.5 Anti-HA Antibody for imaging

A chicken polyclonal anti-HA antibody (Bethyl lab Inc, Montgomery, TX, USA) was used to stain the HA-tagged GlyRs. This antibody was labeled with Alexa Fluor 488 using a commercial Alexa Fluor 488 tetrafluorophenyl labeling kit (Molecular Probes/Invitrogen) and according to the manufacturer's protocol. Two vials of reactive fluorochrome were used to increase the degree of labeling (DOL). The DOL was determined using a Nanodrop ND-1000 spectrophotometer (Thermo Scientific, Wilmington, DE, USA) at 3.9 labels per antibody.

4.1.6 ICS measurements on fixated cells

Cells were rinsed twice with HEPES-buffered DMEM without phenol red (medium without phenol red, MWPR) and incubated for 10 minutes at 37°C with a 4 µg/ml antibody solution. Afterwards, cells were rinsed three times with MWPR and fixated using 4% (w/v) paraformaldehyde in PBS. Images were acquired using a Zeiss LSM 510 META CLSM (Jena, Germany) on an epifluorescence Axiovert 200M motorized frame equipped with an αPLAN-APOCHROMAT 100x/1.46 objective (Zeiss, Jena, Germany). 150 fs pulsed laser light of a Ti:Sapphire laser (Maitai, Spectra-Physics) tuned at an output wavelength of 930 nm (1.4 W output power) with 1.5 mW on the stage was used to excite Alexa Fluor 488. The emission light was detected using non-descanned detection: the fluorescence was directed using a short-pass KP685 and a band-pass BP495-545 towards a PMT (Hamamatsu 7422). This PMT was connected to an SPC830 card (Becker and Hickl) which also received the scan pulses from the CLSM. Data was acquired in fifo imaging mode. The resulting images have a 512 by 512 resolution, a pixel size of 22 nm, and a pixel dwell time of 51.2 µs.

4.1.7 FRAP measurements

FRAP measurements are performed using a Zeiss LSM 510 META CLSM (Jena, Germany) on an epifluorescence Axiovert 200M motorized frame. Samples were excited with the 488 nm line (selected by a 488 ± 10 nm interference-base laser cleanup filter) of the 30 mW air-cooled argon ion laser (5.5 A tube-current) under the control of an AOTF (set at 0.8% transmission). The excitation light

was directed to the sample via a dichroic mirror (DC, HFT 488) and a Plan-Neofluar 40x/1.3 oil immersion objective (Zeiss, Jena, Germany). The fluorescence light was directed through the DC and a long-pass LP505 emission filter to the photomultiplier tube (PMT). The pinhole size was set to 3 Airy units and the image size was typically set to 512 × 512 pixels with a pixel size of 63 nm. The interval between the start of subsequent frames was determined as $\frac{1}{3}\tau_D$. Each time series typically comprised 2 pre-bleach frames and 18 recovery frames. Cells were kept at 37°C by means of a small stage incubator and an objective heater (Pecon).

Data analysis was performed as already described in sections 2.4.2.d and 2.4.2.e, except for the reference area. The latter was selected as depicted in *Figure 2.2 c*.

4.1.8 RICS measurements

The RICS measurements are performed with the identical setup as used for ICS. A small stage incubator and an objective heater (Pecon) was used to keep the cells at 37 °C. Besides the αPLAN-APOCHROMAT 100x/1.46 objective (Zeiss, Jena, Germany), also a LD C-Apochromat 40x/1.1 W Korr UV-VIS-IR objective (Zeiss, Jena, Germany) was used. Pixel sizes are respectively 22.1 nm and 54,8 nm and image resolution was 512 × 512. Pixel dwell times of 163.9 µs, 102 µs, 51.8 µs, 25.6 µs and 6.4 µs were used. The associated line times can be calculated as $1200\tau_P n_{tracks}$, where n_{tracks} is the number of times each line is sequentially scanned before proceeding to the next line.

4.1.9 TICS measurements

All images were acquired using an epi-fluorescence microscope (Olympus IX71 frame S1F-3, Olympus Optical, Tokyo, Japan) equipped with a PlanApo 60× oil (NA 1.45; Olympus Optical, Tokyo, Japan). After passing through a half-wave plate, quarter-wave plate, and two neutral density filters (optical density 2.5 and 0.1, the highest density available on the setup), the laser beam of a 100 mW 488 nm diode laser (Excesior 488, Spectra-Physics) was directed by the dichroic mirror (z405/491rdc; Chroma) towards the objective which it entered off-axis to

obtain TIRF. The resulting fluorescence was collected through the same objective and excitation light was removed using the dichroic and an HQ500LP emission filter (Chroma). The images were recorded using an EM-CCD camera (ImageEM, Hamamatsu) with a resolution of 512 × 512. The resulting pixel size is 80 nm.

The exposure time of the camera was kept constant at 50 ms and the EM gain was set at 149. Images were acquired at various intervals ranging from 50 ms to 5 s. To reduce bleaching, a shutter in the beam path, which also triggered the camera, was used to block the laser light between consecutive images.

Cells were kept at 37°C through the use of a commercial stage incubator (Pecon). Cargille type 37 was used for immersion oil. These measurements were performed in the laboratory of prof. J. Hofkens (KULeuven).

4.2 Results

4.2.1 Expression and functionality

The expression of both HA-tagged splice variants in transfected HEK 293T cells was clearly demonstrated by western blot analysis. Both variants are located between 40 and 50 kDa, as expected. Furthermore, the molecular weight of *HA-GlyRα_3L* was larger than the weight of *HA-GlyRα_3K*. This results from the presence of the extra amino acids in the *L* splice variant.

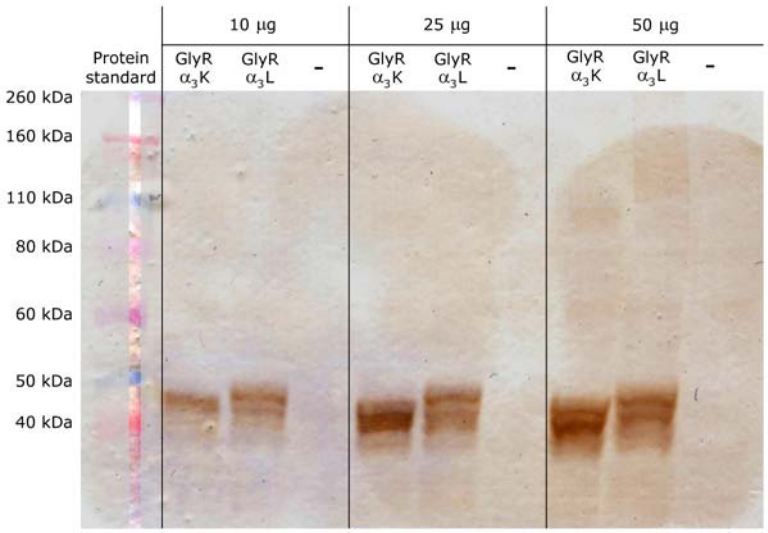

Figure 4.1: HA-GlyR α_3 expression

The expression of both HA-GlyRα_3L and HA-GlyRα_3K was confirmed using western blot. The band of both receptors is located between 40 and 50 kDa, as expected. Furthermore, due to the extra amino acids, the band of HA-GlyRα_3L is located at higher weights as compared to HA-GlyRα_3K. The antibody mAb4a was used to recognize all GlyRs present in the cell lysates. No significant expression was detected of endogenous GlyRs by wild-type HEK 293T cells. (The contrast of a small stripe of the protein standard lane was digitally enhanced to improve the visualization of the protein standard.)

The functionality of both splice variants was demonstrated by electrophysiological data. Furthermore, the time constant of the desensitization of *HA-GlyRα_3L* was significantly larger than that of *HA-GlyRα_3K*, which is in good agreement with literature.[87]

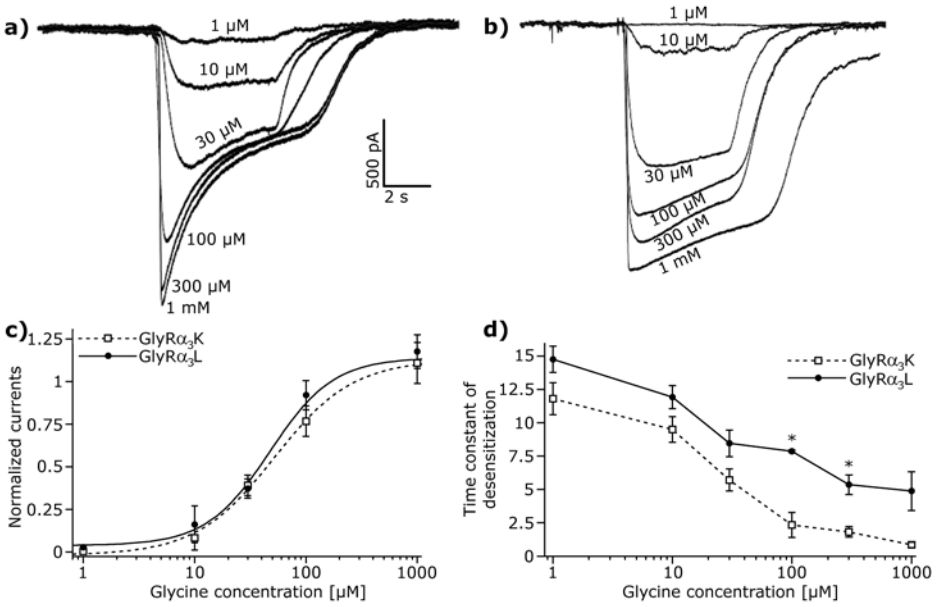

Figure 4.2: Electrophysiological recordings

Current traces of responses were induced by different concentrations of glycine for GlyR α_3 K (a) and GlyR α_3 L (b). The dose-response curve of both receptors is shown in (c). Mean values ± SEM are plotted. A non-linear fit according to the Hill equation revealed an EC_{50} of 47 ± 10 (n=6) for the K splice variant and an EC_{50} 52 ± 24 (n=6) for the L splice variant. The time constant of the desensitization as a function of the glycine concentration of the two isoforms is plotted in (d). A dose-dependent desensitization was present. Moreover, GlyR α_3 L desensitized more slowly than GlyR α_3 K. (: P < 0.05)*

4.2.2 Comparison of aggregation states of splice variants

The aggregation states of the splice variants were quantified using ICS analysis on fixated cells. A homogeneous region of the bottom membrane of cells expressing either GlyR α_3 *K* or *L* was imaged (see *Figure 4.3* for GlyR α_3 *K*). Visual inspection of this type of images already suggests that GlyR α_3 *L* is distributed over less but brighter fluorescent entities, probably clusters (*Figure 4.4 a and b*). This punctate pattern contrasts with the more diffuse staining of GlyR α_3 *K*.

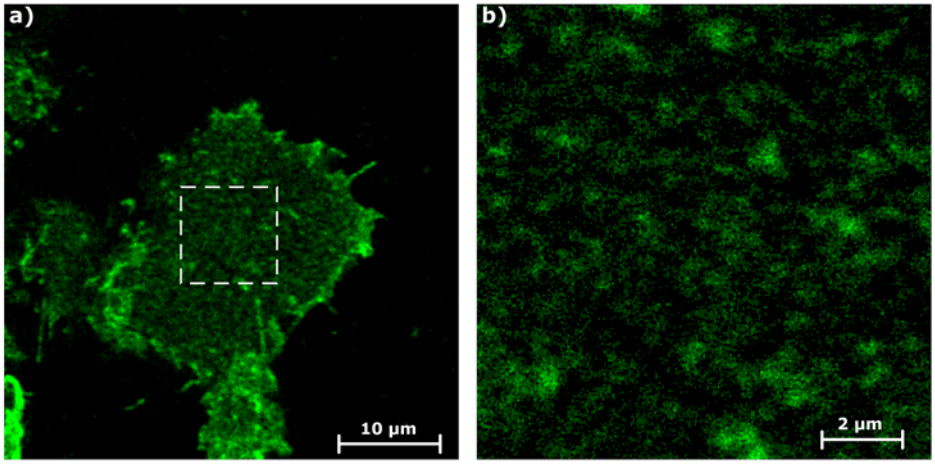

Figure 4.3: Exemplar images of an ICS measurement

(a) A CLSM recording of the bottom membrane of a fixated HEK 293T cell expressing the GlyR α_3K. (b) A magnified region of the cell depicted in (a), indicated by the dashed rectangle). ICS analysis requires the absence of structures and cell edges in the image. This is achieved by increasing the zoom, i.e. decreasing the pixel size.

This qualitative impression is confirmed by ICS analysis (*Figure 4.4 c and d* and *Table 4.1*). On average, there are about 4.5 times more fluorescent entities per μm^2 in cells expressing GlyR α_3 *K* as compared to those expressing the other splice variant. This difference in density is accompanied with a 7.5 times difference in brightness, with the fluorescence entities of GlyR α_3 *L* being the brightest. When a constant brightness of the fluorescent labels, independent of aggregation state of the receptor, is assumed, and when each fluorescent entity of GlyR α_3 *K* is assumed to correspond to an individual receptor, it can be concluded that each fluorescent entity of GlyR α_3 *L* corresponds with a cluster comprising on average 7.5 receptors.

Table 4.1: Summary of ICS results on fixated cells

ICS analysis performed on fixated cells expressing either GlyR α_3K or GlyR α_3L. Particle density $\mathcal{P}$ and brightness ε were corrected for background intensity and non-specific binding of the antibody. Errors are reported as standard errors of the mean (n=9).

splice variant	$\mathcal{P}$ [particles/μm^2]	ε [counts/s particle]	ω_0 [nm]	$\mathcal{H}$
GlyR α_3 *K*	5.9 ± 0.8	0.28 ± 0.04	$43\times10^1 \pm 8\times10^1$	1
GlyR α_3 *L*	1.3 ± 0.3	2.1 ± 0.4	$40\times10^1 \pm 2\times10^1$	7.5 ± 0.4

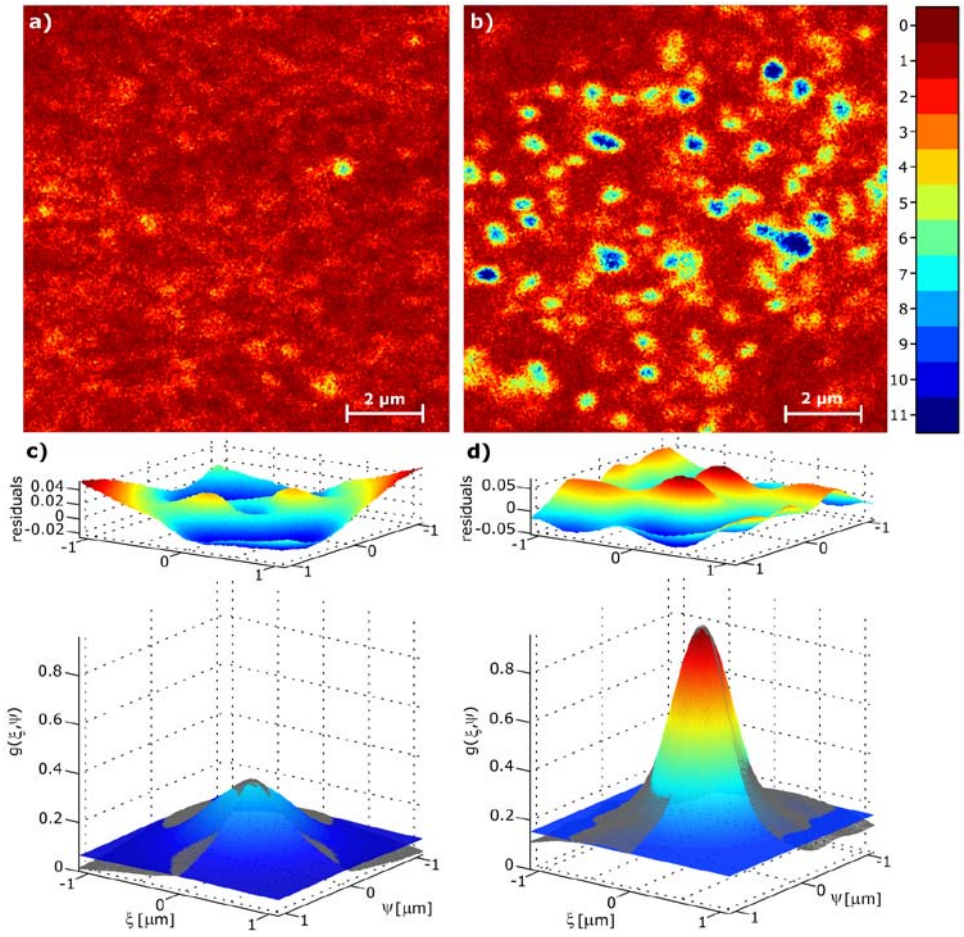

Figure 4.4: ICS analysis of GlyR α_3 K and L variants

(a) and (b) are representative images obtained from respectively GlyR α_3 K and GlyR α_3 L in fixated HEK 293T cells. Both images have the same intensity scale as depicted to the right of panel (b) [expressed in counts per pixels]. Qualitative inspection reveals a diffuse staining of the K splice variant and a punctate pattern of GlyR α_3 L. (c) and (d) are the experimentally obtained SACF (gray mesh, facing quadrant removed) of respectively GlyR α_3 K and GlyR α_3 L, together with the best fit (surface in rainbow colors). The residuals are above the corresponding SACF.

4.2.3 Mobility of splice variants

The mobility of GlyR α_3 *K* and *L* at 37°C was investigated by means of three different techniques: FRAP, RICS and TICS. A summary of the obtained D values per technique is reported in

Table 4.2.

Table 4.2: Summary of obtained diffusion coefficients at 37°C per technique

The average diffusion coefficient [in μm²/s] is reported per microfluorimetric technique that was applied. Errors are reported as standard error of the mean. Number of cells included in the analysis is 31 for FRAP, 6 for RICS (both for K and L) and 6 for TICS (both for K and L). For TICS, two species were found but only the fastest species is reported. The slowest species is unreliable due to photobleaching.

	Microfluorimetric technique		
splice variant	FRAP	RICS	TICS
GlyR α_3 *K*	0.15 ± 0.01	0.11 ± 0.02	0.16 ± 0.07
GlyR α_3 *L*	NF*	0.008 ± 0.002	0.021 ± 0.009

**Not feasible*

FRAP experiments using GlyR α_3 *K* and individually analyzed using the uniform disk model yielded D = 0.15 ± 0.01 μm²/s. This is in good agreement with the other techniques applied. However, when the same data set is analyzed globally, either with the UDM or the new generalized disk model, the resulting diffusion coefficient increases to D = 0.24 ± 0.02 μm²/s. Visual inspection of the graphical representation of the obtained result (*Figure 4.5*) learns that this globally obtained value clearly overestimates the individual values. Furthermore, the resolution factor R retrieved by the global analysis using the GDM is very small and suffers from a large uncertainty (1×10^{-8} ± 0.5 μm²).

The mobile fraction of the GlyR α_3 *K* obtained using the average value of individual analyses was 0.93 ± 0.04. This means that the majority of receptors is mobile during the time frame of the measurement.

FRAP experiments on GlyR α_3 *L* were unsuccessful due to the low concentration of the bright clusters. Movement of these clusters in and out the bleach ROI dramatically affects the recovery curve and render it unsuitable for further analysis. Unrealistic large ROIs have to be considered to avoid these effects.

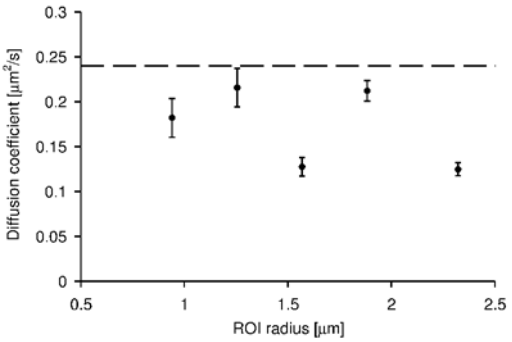

Figure 4.5: FRAP result for GlyR α_3 K

Diffusion coefficients obtained from 31 cells and analyzed using the uniform disk model are plotted as the average and standard deviation per ROI radius. The overall average is 0.15 ± 0.01 µm²/s. The dashed line indicates D obtained using a global analysis of the same data fit to the generalized disk model with a freely adjustable R.

RICS analysis of GlyR α_3 *K* and *L* revealed a difference in D values of more than a decade. Furthermore, several regions from the same cell were analyzed to get information on the heterogeneity of D within a single cell (*Figure 4.6*). This revealed a variation that was smaller than the difference between GlyR α_3 *K* and *L*.

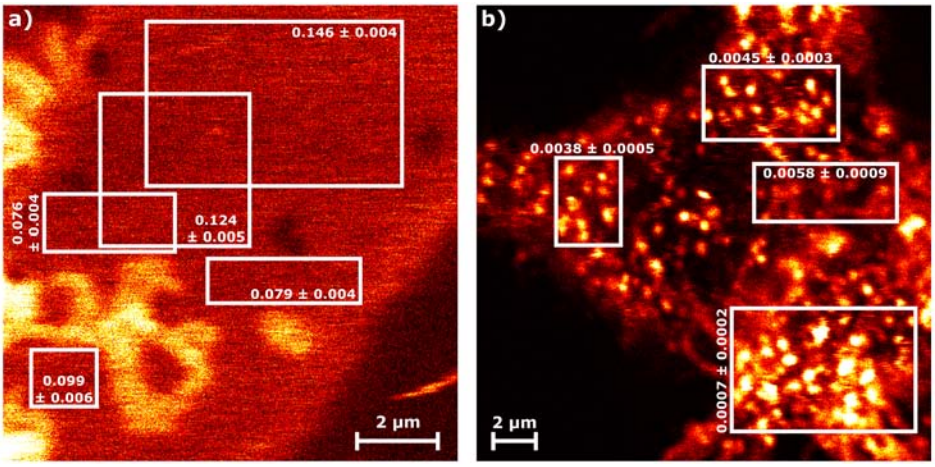

Figure 4.6: Spatial heterogeneity in mobility of GlyRs as revealed by RICS

RICS of live HEK 293T cells expressing GlyR α_3 K (a) and GlyR α_3 L (b) allows for a coarse mapping of the mobility of the respective receptors. Each white rectangular box represents an analyzed area with the obtained D [in µm²/s] and standard error reported. In general, D differs over one decade between both splice variants. In addition, D also varies within a single cell, albeit to a lesser extent. The intensity scale is for each image separately optimized to improve the contrast.

TICS experiments performed on GlyR α_3 *K* and *L* revealed for both splice variants the presence of two species (*Figure 4.7*). Due to the high bleaching rate, only D of the fastest species is reliable. Average D values of both splice variants are a bit higher as compared to the values obtained using RICS. This small discrepancy might arise due to the uncertainty on the radius of the observation profile.

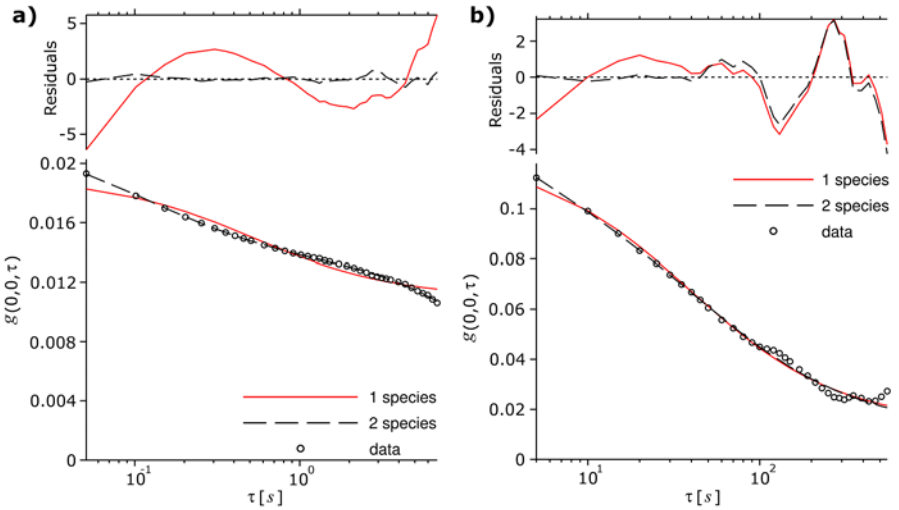

Figure 4.7: Examplar TACFs for GlyR α_3 K and L

The TACF obtained in TICS analysis of GlyR α_3 K (a) and L (b) are plotted, together with the 1 species and 2 species fit. The upper panels show the weighted residuals.

4.3 Discussion

The retrieved D for GlyR α_3 *K* is about five times larger than reported for homomeric GlyR α_1 in HeLa cells, obtained at room temperature by SPT.[29] Both receptors lack the gephyrin-binding domain in their TM3-TM4 endoplasmic loop and are assumed to reside in the plasma membrane as individual receptors. The high homology between both receptor isoforms further suggests that their conformation is comparable. As a result, it is reasonable to expect similar behavior of these GlyRs.

Several factors, both biological and technical in origin, can contribute to a discrepancy in the diffusion coefficient. The most important biological factors are probably the cell lines used in the experiments, and the expression level of the

receptor. The constitution of the plasma membrane might differ between cells. This can result in a different plasma membrane viscosity and hence also in the resultant D. With respect to the expression level, it is known that a high protein content in the cell membrane can lead to a decrease of D due to crowding. Since both experiments were performed at 24 hours after transfection, a similar expression pattern can be expected.

Although the mentioned biological parameters can indeed have an effect, a large part of the discrepancy between both receptor isoforms can probably be explained by the difference in temperature. All experiments in the current work to measure D of GlyR α_3 *K* are performed at 37°C, while the published results with GlyR α_1 in HeLa cells mention room temperature. A lower temperature can indeed decrease D. The best approach to compare both receptors is to remove as many variable parameters as possible. This means that both receptors should be expressed in the same cell line and that all experimental manipulations and measurements are performed as identical as possible.

The difference in temperature is probably the main reason, but it is equally important to recognize that the reported values in the literature are the median values of a collection of Ds obtained using SPT. Inspection of the associated cumulative distribution learns that over 75% of all tracked receptors have a D between 0.1 and 0.01 $\mu m^2/s$. For FRAP and RICS, it can be expected that they are insensitive for the lower Ds due to the time scales applied to probe the large fraction of faster moving receptors. Therefore, slow moving receptors will probably reside in the immobile fraction. This highlights the relative meaning of the immobile fraction i.e. molecules whose movement occurs outside the detection range of the technique which in its turn relies on the experimental parameters. Furthermore, the added value of combining complementary techniques is demonstrated, since TICS did reveal a second, smaller, slow moving fraction of receptors. This presence of at least two populations is also confirmed by on-going SPT studies within the research group.

Opposite to the immobile fraction, it can occur that a sub-population of the proteins moves too fast to be properly detected. The reason of this inability often resides in limitations of the instrument, which cannot obtain the appropriate time or spatial resolution. For the techniques applied to study the GlyR α_3, care has been taken to avoid or at least minimize these artifacts. For

example, if TICS would have been applied as originally described (at a frame rate of 0.2 Hz) the large, fast moving fractions of the proteins would not be detected. Of course, the current frame rate of 20 Hz can still be improved, although this is technically demanding. Yet, presence of a subpopulation that moves even faster would easily be detected by RICS at higher scan speeds. This procedure did not result in higher Ds and thus excludes any such occurrence.

For the other variant GlyR α_3 *L* the obtained D seems to be in very good correspondence with reported values for the adult GlyR $\alpha_1\beta$ outside the range of a gephyrin meshwork.[29] However, these reported results are also obtained at room temperature. Therefore, it can be expected that GlyR α_3 *L* diffuses slower than GlyR $\alpha_1\beta$. This suggests that GlyR $\alpha_1\beta$ outside the range of a gephyrin meshwork is present in smaller clusters than those of GlyR α_3 *L*, at least if GlyR α_3 *L* does not interact with cytoplasmic proteins.

Irrespective of the cause, clustering of GlyR α_3 *L* is quantified. On average, these clusters comprise 7.5 receptors assuming a constant brightness per receptor. When aggregation reduces this brightness, for example by steric hindrance of bound antibody, 7.5 will be the lower limit. Note that application of high-resolution methods would suffer from the same problem. Due to this extra uncertainty, it is better to round the average number of receptors per GlyR α_3 *L* cluster to 8. The size of the detected clusters is still below the diffraction limit, as indicated by the average retrieved observation profile radius in ICS. This radius does not differ significantly between both splice variants, as can also be predicted based on the size of the GlyR (8.5 nm diameter).[57]

Based on D values of both *L* and *K* splice variant, a larger number of receptors in the GlyR α_3 *L* clusters could be expected. For free diffusion in the plasma membrane, it has been shown that D is proportional to the inverse of the particle radius.[37] For GlyR α_3 *L*, this would mean that the cluster size is roughly 85 nm, requiring more than just 8 receptors. However, the cluster size is not the only factor influencing D. As indicated above, interactions with cytoplasmic proteins and the cellular cytoskeleton can also decrease D.

In conclusion, clustering of GlyR α_3 *L* is confirmed and each cluster is estimated to comprise 8 receptors on average. This clustering is also reflected by the difference in diffusion coefficient between GlyR α_3 *L* and GlyR α_3 *K*. The various

techniques applied yield consistent results. However, in order to investigate putative interactions with submembranous proteins, it is required to compare these control situations with test conditions, such as the disruption of the cytoskeleton or the use of receptors holding point mutations.

5 General discussion and conclusions

The main goal of this research is to explore the feasibility of studying the GlyR α_3 in the plasma membrane of live cells using ensemble averaging techniques. Due to the existing relationship between receptor clustering and receptor desensitization kinetics,[70] aggregation of the receptor can be a manner to regulate the receptor. To investigate the causes of this clustering, accurate description of the clustering and mobility of the receptors is required. The explored techniques (FRAP, ICS, RICS and TICS) are briefly discussed, followed by a discussion of the results obtained for the GlyR α_3.

Practical details of the application of FRAP to study processes in live cells were considered. This resulted in a thorough and objective approach to select a reference region. Furthermore, a new approach was developed to estimate the weights of a single recovery curve. Finally, global analysis was introduced to improve the analysis of recovery curves.

The other considered techniques belong to the family of image correlation techniques and have many properties in common. To better understand these methods, a good understanding of FCS is beneficial. FCS can be considered as the ancestor of the family of ICS techniques. The interpretation of the amplitude of the resulting autocorrelation functions is discussed in great detail, covering the situation of multiple species and an immobile fraction. For ICS, the amplitude is very important. When the results are properly corrected for the contribution of detection noise and non-specific binding, accurate estimates of the concentration of a fluorescently labeled protein can be obtained. Nevertheless, if a large variance in particle brightness exists, the obtained concentration is underestimated. Yet, it can still serve as a lower limit of the concentration.

RICS, the second correlation technique applied in this work, was tested using 3D isotropic diffusion of fluorescent beads prior to protein diffusion studies. Obtained results were in good agreement with theoretically expected values. This indicates that the perturbation of the SACF by the correlation due to detection noise is appropriately brought into account.

The main advantage of RICS is that it does not require special hardware. A regular CLSM is sufficient. We have demonstrated previously its successful application to study membrane proteins. In this work, RICS analyses indicate an

obvious difference in diffusion coefficient of GlyR α_3 *K* and *L*, as expected from the clustering demonstrated by ICS. Furthermore, the heterogeneity within individual cells could be investigated due to the mapping capability of RICS. This heterogeneity was much smaller than the difference observed between the splice variants.

Finally, TICS was considered in great detail. The amount of bleaching the technique can tolerate was demonstrated as a function of the expected diffusion coefficient. This maximal tolerable amount was further generalized by defining it as the total fluorescence lost at the end of the measurement. Furthermore, it was demonstrated that offset of the TACF is sensitive to the presence of an immobile fraction, but that other factors might also contribute to this offset. Application of TICS to study GlyR α_3 *K* and *L* revealed two species, of which only the fasted species could reliably be interpreted due to the amount of bleaching.

Published reports mainly utilize single particle tracking (SPT) to study the dynamic behavior of the GlyR.[2,7,17,29,71,81] The contribution of these SPT studies to current insights in the GlyR dynamics and synaptic regulation is very important. The capability of SPT to study individual proteins and uncover putative subpopulations has led to the demonstration of multiple association states between the adult GlyR $\alpha_1\beta$ and gephyrin.[29] The four explored techniques offer an added values to these studies. For example, ICS can determine the average number of receptors per cluster.

In order to be successful, all microfluorimetric methods applied to study proteins in the plasma membrane of live cells should be non-invasive and fast. Non-invasive in this context means that the measurement does not interfere with the protein dynamics. Since all considered techniques as well as SPT use fluorescence, their non-invasiveness is identical. Both HA-tagged GlyR α_3 splice variants used in the experiments are demonstrated to function properly. This proves a correct oligomerization of its subunits. For all tested techniques, GlyR α_3 is further labeled using a fluorescently labeled anti-HA antibody. The divalent binding capability of this antibody could induce clustering of the receptor through cross-linking. However, ICS results indicate no such antibody-induced clustering. To further minimize any effect of the antibody, it was labeled with a fluorescent dye (Alexa Fluor 488) instead of using quantum dots. Unfortunately,

the reduced size of the fluorescent dye is accompanied by a reduction in the signal-to-noise ratio and photostability.

The second property of interest is the acquisition time. Cells studied at 37°C are very active and mobile. To reduce the effect of cell movement or membrane undulations, it is best to keep the measurement time short. Yet, the proteins have to move, so the minimum time required for the measurement is in part bounded by the magnitude of the diffusion coefficients. In addition, the distance the proteins have to travel during the measurement is the other determinant. This holds the fundamental difference between the ensemble-average techniques and SPT. The latter measures the distance travelled by the protein during a defined period of time while the other methods measure the time required to travel a fixed distance. Due to the diffraction limit, the minimal fixed distance will easily be an order of magnitude larger than the minimal displacement that can be detected by SPT. As a result, it can be expected that SPT will always outperform the other techniques when considering very small Ds in the plasma membrane of live cells.

For FRAP, the distance proteins need to travel is determined by the size of the bleach region (down to 1 µm). Since the required time scales with the square of the radius of the bleach ROI, larger ROIs are more susceptible to be affected by cell movement. To improve the accuracy of smaller ROIs, the new generalized model brings into account the finite resolution of the instrument.

For TICS and RICS, the diffraction limit is the lower boundary of the distances at which protein movement can be measured. For very small Ds, TICS measurements can take minutes before acquiring enough fluctuations. RICS, in contrast, is limited by the slowest scan speed of the instrument. However, although the acquisition of a single image can take up to a few minutes, the correlation is only considered between adjacent pixels and lines which are only a few seconds apart. As previously discussed, RICS measures fewer fluctuations as compared to TICS, and this abolishes the improved accuracy due to reduced cell movement. The observation area can be reduced, i.e. the diffraction limit can be circumvented, by using stimulated emission depletion (STED). The reduced size of the observation area, would allow RICS to probe smaller Ds.

Although FRAP, RICS and TICS might suffer from cell movement for very small Ds, the results obtained for GlyR α_3 *K* and *L* are in good agreement with preliminary SPT measurements performed within the research group (*preliminary results obtained by Kristof Notelaers*). Nevertheless, for values of D as reported for GlyRs at synapses, these techniques will probably be not applicable due to the long acquisition times involved.

For the studied GlyR α_3 splice variants, all explored techniques return mutually consistent results. Clusters of GlyR α_3 *L*, estimated to comprise at least 8 receptors, are shown to diffuse much slower than GlyR α_3 *K*. With FRAP it was not feasible to obtain accurate results for GlyR α_3 *L* due to the low density of the clusters. On the other hand, FRAP clearly indicated that the majority of GlyR α_3 *K* are mobile on the time scale of the measurements. Other technical limitations were encountered for TICS. TICS experiments suffered from too much photobleaching during image acquisition, while using all laser attenuation available on the setup. Decreasing the frame rate is not an option due to the minimal frame rate dictated by the diffusion coefficient of the receptors. Therefore, the only way to reduce photobleaching is to use a higher laser attenuation. The concomitant loss of intensity can be partially compensated by increasing the pixel size of the camera.

Based on these results, it can be concluded that the ensemble averaging techniques are capable to give an integrated view on the mobility and aggregation state of the receptors.

Future directions

Clustering of GlyR α_3 *L* is quantified but its origin is not demonstrated. To investigate the cause of this clustering, the explored techniques should also be applied to biological cells expressing GlyR α_3 *L* and treated with agents that can disrupt putative interactions. For example, latrunculin A can be used to probe the effect of the cytoskeleton through its disruption. Similarly, nocodazole can be used to study the effect of microtubules. Direct study of the aggregation state of the receptors combined with information on their mobility across several test conditions could reveal the cause of the clustering.

Another important issue that should be considered is the expression level of the receptors. Since an increasing density of GlyR α_1 is shown to lead to a change in receptor desensitization kinetics,[70] possibly through induction of clustering, experiments should be performed at various time points after transfection. Since the correlation techniques offer the possibility to determine the receptor density aside the receptor mobility, they are excellent candidates to review this effect on GlyR α_3 splice variants.

Finally, the correlation techniques applied in this work utilizes only one type of staining. When two batches of antibodies with each a different fluorochrome are used, interaction between receptors could directly be measured by calculation of the cross-correlation function between the two channels.

In the end, when a change in mobility or aggregation is observed, these results should be complemented with electrophysiological data in order to determine its impact on the functionality of the receptor.

Nederlandse samenvatting 6

De glycinereceptor (GlyR) vervult een belangrijke rol in de snelle, inhibitorische neuronale signaaloverdracht in het centrale zenuwstelsel van vertebraten. De GlyR is een pentameer dat kan bestaan uit verschillende subeenheden (α_1, α_2, α_3, α_4, β). Clustering van de heteropentamere GlyR α_1β ter hoogte van het post-synaptisch membraan is essentieel om de signaaloverdracht efficiënt uit te voeren. De regulatie van deze clustering werd lange tijd beschouwd als een statisch gegeven waarbij voornamelijk de endo- en exocytose van aggregaten van GlyRs bepalend werd geacht. Fluorescentiemicroscopie van de receptor in levende cellen heeft deze visie grondig veranderd.

Het statisch model is geleidelijk aan vervangen door een dynamisch evenwicht tussen een synaptische en een extrasynaptische groep GlyRs. Dit evenwicht wordt gereguleerd door laterale diffusie van de receptoren in het celmembraan gecombineerd met transiënte binding aan submembranaire eiwitten. Belangrijk hierbij is de interactie tussen de β subeenheid van de GlyR en het submembranair eiwit gephyrine. De overige subeenheden (α_1 tot en met α_4) kunnen geen binding aangaan met gephyrine. Aanwezigheid van de β subeenheid in de GlyR is noodzakelijk voor de clustering van de receptor ter hoogte van het post-synaptisch membraan.

De GlyR is ook betrokken bij andere processen. Zo vervult de homomere GlyRα_3 een prominente rol bij het zicht, de nociceptie en bij het verwerken van akoestische signalen. Daarnaast is de GlyR α_3 ook aanwezig in de hippocampus, waar post-transcriptionele modificatie van het GLRA3 transcript geassocieerd wordt met pathofysiologische aspecten van *temporal lobe* epilepsie (TLE). Bovendien is ook de regulatie van de alternatieve *splicing* van de GlyR α_3 veranderd in patiënten met ernstige TLE: de expressie van GlyR α_3 *K* is verhoogd ten koste van GlyR α_3 *L*. Het verschil tussen deze *splice*-varianten beperkt zich tot een segment van 15 aminozuren dat ontbreekt bij GlyR α_3 *K*.

Net als bij de overige GlyR α subeenheden hebben zowel de GlyR α_3 *K* als de GlyR α_3 *L* subeenheden geen gephyrine-bindingsdomein. Desondanks leiden de 15 extra aminozuren tot een clustering van de GlyR α_3 *L* en een vertraging van de desensitisatiekinetiek. Hoewel voor de GlyR α_1 is beschreven dat de receptordichtheid en desensitisatiekinetiek versnelt, is het duidelijk dat er een nauwe relatie bestaat tussen de aggregatietoestand van de receptoren en hun

werking. Om deze relatie verder te onderzoeken is het noodzakelijk om de aggregatietoestand van de receptoren en mogelijke interacties met submembranaire eiwitten te bepalen. Hiertoe werden in dit werk vier *ensemble-average* microfluorimetrische technieken toegepast. Sommige van deze technieken werden uitgebreid bestudeerd en verder ontwikkeld. De resultaten bekomen voor de GlyR α_3 *K* en de GlyR α_3 *L* werden onderling vergeleken en getoetst aan gepubliceerde waarden.

Hieronder wordt eerst een kort overzicht van de toegepaste technieken gegeven waarna de resultaten voor de GlyR α_3 *K* en de GlyR α_3 *L* worden toegelicht.

De eerste techniek die werd toegepast was *fluorescence recovery after photobleaching* (FRAP, ***Hoofdstuk 2***). Bij deze techniek wordt het herstel van de fluorescentie intensiteit binnen een welbepaalde regio na een korte bleekfase gebruikt om de diffusiecoëfficiënt en de fractie van mobiele receptoren te verkrijgen. Een nieuwe methode werd geïntroduceerd voor de selectie van een controlegebied om de techniek minder gevoelig te maken voor de laterale heterogeniteit in het plasma membraan van een levende cel. Daarenboven werd een nieuwe aanpak afgeleid voor het schatten van de variantie van elke herstelcurve. Hierdoor is het niet langer nodig om identieke metingen te verrichten om tot een betrouwbare schatting te komen. Deze nieuwe methode werd geïntegreerd met een simultane (globale) analyse van de herstelcurves, waarbij alle herstelcurves niet langer individueel maar collectief geanalyseerd worden. Hierbij wordt rekening gehouden met de gemeenschappelijke parameters over de fitcurven waardoor het aantal vrijheidsgraden gereduceerd wordt.

De kracht van deze vernieuwende aanpak werd duidelijk aangetoond bij de toepassing van het *generalized disk model*. Dit nieuwe theoretisch model, afgeleid door prof. K. Braeckmans, brengt de eindige resolutie van de optische microscoop in rekening, en dit zowel tijdens de bleekfase als tijdens het opnemen van de beelden. Hierdoor kunnen ook bleekregio's kleiner dan vier keer de *point-spread* functie betrouwbaar geanalyseerd worden. Het nieuwe model vereist echter kennis van zowel de detectie- als de bleek-*point-spread*

functie. Een globale analyse van een dataset die bleekregio's van verscheidene groottes omvat, laat toe om deze parameters simultaan met de overige parameters te bepalen. Hierdoor zijn geen bijkomende kalibratiemetingen vereist.

De overige technieken die werden toegepast zijn alle gerelateerd aan fluorescentie correlatiespectroscopie (FCS). Daarom werden eerst de basisprincipes van FCS besproken (**Hoofdstuk 3**). Deze techniek gebruikt de autocorrelatie van spontane, thermodynamische fluctuaties die ontstaan door de diffusie van de fluorescente deeltjes, om zowel deze diffusie alsook de concentratie van de deeltjes te bepalen. Dit gebeurt door de genormaliseerde autocorrelatiefunctie (ACF) te berekenen. Drie aanverwante technieken maken gebruik van beelden en daarom spreekt men van *image* correlatiespectroscopie (ICS), *raster* ICS (RICS) en *temporal* ICS (TICS). ICS is de oudste van de drie technieken en geeft geen informatie over de dynamiek van de receptoren. Het laat echter wel toe om de aggregatietoestand van de receptor af te schatten door verscheidene situaties met elkaar te vergelijken. De enige voorwaarde is dat de receptoren gefixeerd zijn of als gefixeerd kunnen worden beschouwd tijdens de opname van de beelden.

RICS leunt qua analysemethode heel nauw aan bij ICS, maar deze techniek veronderstelt niet langer dat de receptoren gefixeerd zijn. Daarenboven vereist RICS dat de beelden zijn opgenomen met behulp van een confocale, laser-scannende microscoop. Op deze wijze bevat elk beeld niet alleen spatiale informatie, maar is er ook een temporale component aanwezig die toelaat de dynamiek van de receptoren te bestuderen. Om de nauwkeurigheid van een RICS meting te verbeteren, kunnen de spatiale ACFs van verscheidene beelden gemiddeld worden. Ten opzichte van FCS heeft RICS het grote voordeel dat er tijdens de meting ook een beeld wordt opgebouwd van de cel. Omdat RICS een relatief nieuwe techniek is, werd de methode eerst gevalideerd door middel van 3D isotrope diffusie van fluorescente *beads*.

TICS, ten slotte, laat ook toe om de dynamiek van de receptor te beschrijven. In tegenstelling tot RICS wordt het verloop van de fluctuaties tussen individuele beelden gebruikt om de dynamiek te beschrijven. In essentie kunnen TICS metingen beschouwd worden als talrijke FSC metingen in parallel. Hierdoor kan de benodigde meettijd aanzienlijk worden verkort. TICS zou ook kunnen

gebruikt worden voor het bepalen van de immobiele fractie op basis van de offset van de ACF. Er zijn echter nog andere factoren die tot eenzelfde effect kunnen leiden. Tenslotte is het effect van bleking op TICS resultaten onderzocht. Als uitbreiding op de bestaande literatuur is aangetoond dat niet enkel de snelheid van de bleking maar ook het totale fluorescentieverlies belangrijke parameters zijn.

Bovenstaande technieken werden gebruikt om de GlyR α_3 *K* en *L* te onderzoeken. Analyse van GlyR α_3 *K* met FRAP, RICS als TICS resulteerden allen in een diffusiecoëfficiënt tussen 0.11 en 0.16 $\mu m^2/s$. Deze waarden liggen vijf keer hoger dan de diffusiecoëfficiënt vermeld voor de GlyR α_1 in de literatuur, maar dit verschil kan grotendeels worden verklaard door het verschil in temperatuur waarbij de metingen plaatsvonden (37°C in het voorliggende werk versus kamertemperatuur in de literatuur). Andere factoren die een verschil in de hand kunnen werken zijn de verschillende celtypes en de verschillende technieken die gebruikt zijn. De waarden in de literatuur zijn verkregen door middel van *single-particle tracking* (SPT) en deze techniek kan een afwijking naar tragere diffusiecoëfficiënten vertonen. FRAP analyse van GlyR α_3 *K* toont ook aan dat ongeveer 93% van alle receptoren mobiel zijn. Dit wil zeggen dat een kleine fractie van de receptoren gebonden zijn of dat ze schijnbaar immobiel zijn op de tijdschaal van de metingen. Op basis van de TICS metingen kan men concluderen dat er minstens twee subpopulaties van de GlyR α_3 *K* aanwezig zijn. Helaas laten de experimentele omstandigheden niet toe om de tragere subpopulatie betrouwbaar in kaart te brengen.

FRAP, RICS en TICS werden ook toegepast op de GlyR α_3 *L*. Helaas resulteerde dit voor FRAP niet in bruikbare resultaten door de lage densiteit van de fluorescente deeltjes, vermoedelijk receptorclusters. De overige technieken werden wel succesvol toegepast en dit resulteerde in een diffusiecoëfficiënt die minstens een factor 10 kleiner is. Ook voor deze *splice*-variant werden er met TICS twee subpopulaties gedetecteerd.

Het verschil in diffusiecoëfficiënt tussen GlyR α_3 *K* en *L* zou kunnen verklaard worden door ofwel aggregatie van GlyR α_3 *L*, ofwel door interactie van de GlyR α_3 *L* met een submembranair eiwit of structuur, ofwel door een combinatie van

deze twee. ICS analyse van de receptoren heeft aangegeven dat elk fluorescent deeltje van de GlyR α_3 *L* equivalent is aan minstens acht fluorescente deeltjes van de GlyR α_3 *K*. In de veronderstelling dat de fluorescente deeltjes van de GlyR α_3 *K* individuele receptoren voorstellen, kan men besluiten dat de GlyR α_3 *L* aggregaten vormt met minstens acht receptoren. Samenvattend kan het verschil in de diffusiecoëfficiënt minstens ten dele verklaard worden door aggregatie van de GlyR α_3 *L*. De oorzaak van deze aggregatie, ofwel inherent aan de receptor of door interactie met een andere eiwit, blijft echter onbepaald.

Om de oorzaak van de aggregatie te onderzoeken kunnen er twee strategieën gevolgd worden, die elkaar niet noodzakelijk uitsluiten. In een eerste aanpak kan men de interacties met andere cellulaire componenten onderzoeken door de controlesituatie te vergelijken met testsituaties waarin deze mogelijke interacties voorkomen of afgebroken worden. Zo kan men de interactie met het cytoskelet onderzoeken met inhibitie van het actinenetwerk door middel van latrunculine A. De interactie tussen de receptoren onderling kan dan weer bestudeerd worden door gebruik te maken van twee verschillende fluorochromen. De kruiscorrelatie (CCF) tussen beide fluorochromen bepaald door ICCS, RICCS of TICCS, zal dan aangeven welke fractie van de receptoren zich samen in de celmembraan beweegt en onderling een interactie aangaat.

List of references

1. Akagi H., Hirai K., and Hishinuma F. (**1991**) "Cloning of a glycine receptor subtype expressed in rat brain and spinal cord during a specific period of neuronal development" FEBS Lett. 281(1-2): 160-6 [DOI:10.1016/0014-5793(91)80383-E]

2. Alcor D., Gouzer G., and Triller A. (**2009**) "Single-particle tracking methods for the study of membrane receptors dynamics" Eur. J. Neurosci. 30(6): 987-97 [DOI:10.1111/j.1460-9568.2009.06927.x]

3. Axelrod D., Koppel D.E., Schlessinger J., Elson E., and Webb W.W. (**1976**) "Mobility measurement by analysis of fluorescence photobleaching recovery kinetics" Biophys. J. 16(9): 1055-69 [DOI:10.1016/S0006-3495(76)85755-4]

4. Axelrod D., Ravdin P., Koppel D.E., Schlessinger J., et al. (**1976**) "Lateral motion of fluorescently labeled acetylcholine receptors in membranes of developing muscle fibers" Proc. Natl. Acad. Sci. U. S. A. 73(12): 4594-8 [DOI:10.1073/pnas.73.12.4594]

5. Baker A.M., Sauliere A., Gaibelet G., Lagane B., et al. (**2007**) "CD4 interacts constitutively with multiple CCR5 at the plasma membrane of living cells. A fluorescence recovery after photobleaching at variable radii approach" J. Biol. Chem. 282(48): 35163-8 [DOI:10.1074/jbc.M705617200]

6. Becker C.M., Hoch W., and Betz H. (**1988**) "Glycine receptor heterogeneity in rat spinal cord during postnatal development" EMBO J. 7(12): 3717-26

7. Bedet C., Bruusgaard J.C., Vergo S., Groth-Pedersen L., et al. (**2006**) "Regulation of gephyrin assembly and glycine receptor synaptic stability" J. Biol. Chem. 281(40): 30046-56 [DOI:10.1074/jbc.M602155200]

8. Beechem J.M., Gratton E., Ameloot M., Knutson J.R., and Brand L. (**1991**) "The global analysis of fluorescence intensity and anisotropy decay data: second generation theory and programs" in Topics in Fluorescence Spectroscopy: Volume2: Principles, J. R. Lakowicz, Ed., pp. 241-305, Plenum Press, New York.

9. Benda A., Benes M., Marecek V., Lhotsky A., Hermens W.T., and Hof M. (**2003**) "How to determine diffusion coefficients in planar phospholipid systems by confocal fluorescence correlation spectroscopy" Langmuir 19(10): 4120-6 [DOI:10.1021/La0270136]

10. Blonk J.C.G., Don A., Vanaalst H., and Birmingham J.J. (**1993**) "Fluorescence photobleaching recovery in the confocal scanning light-microscope" J. Microsc. 169: 363-74

11. Bormann J., Rundstrom N., Betz H., and Langosch D. (**1993**) "Residues within Transmembrane Segment M2 Determine Chloride Conductance of Glycine Receptor Homo-Oligomers and Heterooligomers" EMBO J. 12(10): 3729-37

12. Braeckmans K., Peeters L., Sanders N.N., De Smedt S.C., and Demeester J. (**2003**) "Three-dimensional fluorescence recovery after photobleaching with the confocal scanning laser microscope" Biophys. J. 85(4): 2240-52 [DOI:10.1016/S0006-3495(03)74649-9]

13. Braeckmans K., Stubbe B.G., Remaut K., Demeester J., and De Smedt S.C. (**2006**) "Anomalous photobleaching in fluorescence recovery after photobleaching measurements due to excitation saturation--a case study for fluorescein" J. Biomed. Opt. 11(4): 044013 [DOI:10.1117/1.2337531]

14. Braeckmans K., Remaut K., Vandenbroucke R.E., Lucas B., De Smedt S.C., and Demeester J. (**2007**) "Line FRAP with the confocal laser scanning microscope for diffusion measurements in small regions of 3-D samples" Biophys. J. 92(6): 2172-83 [DOI:10.1529/biophysj.106.099838]

15. Brown C.M., Dalal R.B., Hebert B., Digman M.A., Horwitz A.R., and Gratton E. (**2008**) "Raster image correlation spectroscopy (RICS) for measuring fast protein dynamics and concentrations with a commercial laser scanning confocal microscope" J. Microsc. 229(Pt 1): 78-91 [DOI:10.1111/j.1365-2818.2007.01871.x]

16. Cascio M. (**2004**) "Structure and function of the glycine receptor and related nicotinicoid receptors" J. Biol. Chem. 279(19): 19383-6 [DOI:10.1074/jbc.R300035200]

17. Charrier C., Ehrensperger M.V., Dahan M., Levi S., and Triller A. (**2006**) "Cytoskeleton regulation of glycine receptor number at synapses and diffusion in the plasma membrane" J. Neurosci. 26(33): 8502-11 [DOI:10.1523/JNEUROSCI.1758-06.2006]

18. Chenna R., Sugawara H., Koike T., Lopez R., et al. (**2003**) "Multiple sequence alignment with the Clustal series of programs" Nucleic Acids Res. 31(13): 3497-500 [DOI:10.1093/nar/gkg500]

19. Comeau J.W., Costantino S., and Wiseman P.W. (**2006**) "A guide to accurate fluorescence microscopy colocalization measurements" Biophys. J. 91(12): 4611-22 [DOI:10.1529/biophysj.106.089441]

20. Coons A., Creech H., and Jones R. (**1941**) "Immunological properties of an antibody containing a fluorescent group" Proc. Soc. Exp. Biol. Med. 47: 200-2

21. Costantino S., Comeau J.W., Kolin D.L., and Wiseman P.W. (**2005**) "Accuracy and dynamic range of spatial image correlation and cross-correlation spectroscopy" Biophys. J. 89(2): 1251-60 [DOI:10.1529/biophysj.104.057364]

22. Dalal R.B., Digman M.A., Horwitz A.F., Vetri V., and Gratton E. (**2008**) "Determination of particle number and brightness using a laser scanning confocal microscope operating in the analog mode" Microsc. Res. Tech. 71(1): 69-81 [DOI:10.1002/jemt.20526]

23. Delon A., Usson Y., Derouard J., Biben T., and Souchier C. (**2004**) "Photobleaching, mobility, and compartmentalisation: inferences in fluorescence correlation spectroscopy" J. Fluoresc. 14(3): 255-67 [DOI:10.1023/B:JOFL.0000024557.73246.f9]

24. Dertinger T., Pacheco V., von der Hocht I., Hartmann R., Gregor I., and Enderlein J. (**2007**) "Two-focus fluorescence correlation spectroscopy: a new tool for accurate and absolute diffusion measurements" Chemphyschem 8(3): 433-43 [DOI:10.1002/cphc.200600638]

25. Digman M.A., Sengupta P., Wiseman P.W., Brown C.M., Horwitz A.R., and Gratton E. (**2005**) "Fluctuation correlation spectroscopy with a laser-scanning microscope: exploiting the hidden time structure" Biophys. J. 88(5): L33-6 [DOI:10.1529/biophysj.105.061788]

26. Digman M.A., Dalal R., Horwitz A.F., and Gratton E. (**2008**) "Mapping the number of molecules and brightness in the laser scanning microscope" Biophys. J. 94(6): 2320-32 [DOI:10.1529/biophysj.107.114645]

27. Dlugaiczyk J., Singer W., Schick B., Iro H., et al. (**2008**) "Expression of glycine receptors and gephyrin in the rat cochlea" Histochem. Cell Biol. 129(4): 513-23 [DOI:10.1007/s00418-008-0387-x]

28. Edidin M., Zagyansky Y., and Lardner T.J. (**1976**) "Measurement of membrane protein lateral diffusion in single cells" Science 191(4226): 466-8 [DOI:10.1126/science.1246629]

29. Ehrensperger M.V., Hanus C., Vannier C., Triller A., and Dahan M. (**2007**) "Multiple association states between glycine receptors and gephyrin identified by SPT analysis" Biophys. J. 92(10): 3706-18 [DOI:10.1529/biophysj.106.095596]

30. Eichler S.A., Kirischuk S., Juttner R., Schafermeier P.K., et al. (**2008**) "Glycinergic tonic inhibition of hippocampal neurons with depolarizing GABAergic transmission elicits histopathological signs of temporal lobe epilepsy" J Cell Mol Med 12(6B): 2848-66 [DOI:10.1111/j.1582-4934.2008.00357.x]

31. Eichler S.A., Forstera B., Smolinsky B., Juttner R., et al. (**2009**) "Splice-specific roles of glycine receptor alpha3 in the hippocampus" Eur. J. Neurosci. 30(6): 1077-91 [DOI:10.1111/j.1460-9568.2009.06903.x]

32. Enderlein J., Gregor I., Patra D., and Fitter J. (**2004**) "Art and artefacts of fluorescence correlation spectroscopy" Curr. Pharm. Biotechnol. 5(2): 155-61 [DOI:10.2174/1389201043377020]

33. Enderlein J., Gregor I., Patra D., and Fitter J. (**2005**) "Statistical analysis of diffusion coefficient determination by fluorescence correlation spectroscopy" J. Fluoresc. 15(3): 415-22 [DOI:10.1007/s10895-005-2633-0]

34. Feher G., and Weissman M. (**1973**) "Fluctuation Spectroscopy: Determination of Chemical Reaction Kinetics from the Frequency Spectrum of Fluctuations" Proceedings of the National Academy of Sciences 70(3): 870-5 [DOI:10.1073/pnas.70.3.870]

35. Flint A.C., Liu X., and Kriegstein A.R. (**1998**) "Nonsynaptic glycine receptor activation during early neocortical development" Neuron 20(1): 43-53 [DOI:10.1016/S0896-6273(00)80433-X]

36. Fritschy J.M., Harvey R.J., and Schwarz G. (**2008**) "Gephyrin: where do we stand, where do we go?" Trends Neurosci. 31(5): 257-64 [DOI:10.1016/j.tins.2008.02.006]

37. Gambin Y., Lopez-Esparza R., Reffay M., Sierecki E., et al. (**2006**) "Lateral mobility of proteins in liquid membranes revisited" Proc. Natl. Acad. Sci. U. S. A. 103(7): 2098-102 [DOI:10.1073/pnas.0511026103]

38. Gielen E., Smisdom N., vandeVen M., De Clercq B., et al. (**2009**) "Measuring Diffusion of Lipid-like Probes in Artificial and Natural Membranes by Raster Image Correlation Spectroscopy (RICS): Use of a Commercial Laser-Scanning Microscope with Analog Detection" Langmuir 25(9): 5209-18 [DOI:10.1021/La8040538]

39. Gielen E., Vandeven M., Margineanu A., Dedecker P., et al. (**2009**) "On the use of Z-scan fluorescence correlation experiments on giant unilamellar vesicles" Chem. Phys. Lett. 469(1-3): 110-4 [DOI:10.1016/j.cplett.2008.12.061]

40. Grenningloh G., Rienitz A., Schmitt B., Methfessel C., et al. (**1987**) "The strychnine-binding subunit of the glycine receptor shows homology with nicotinic acetylcholine receptors" Nature 328(6127): 215-20 [DOI:10.1038/328215a0]

41. Grenningloh G., Pribilla I., Prior P., Multhaup G., et al. (**1990**) "Cloning and expression of the 58 kd beta subunit of the inhibitory glycine receptor" Neuron 4(6): 963-70 [DOI:10.1016/0896-6273(90)90149-A]

42. Griffon N., Buttner C., Nicke A., Kuhse J., Schmalzing G., and Betz H. (**1999**) "Molecular determinants of glycine receptor subunit assembly" EMBO J. 18(17): 4711-21 [DOI:10.1093/emboj/18.17.4711]

43. Grudzinska J., Schemm R., Haeger S., Nicke A., et al. (**2005**) "The beta subunit determines the ligand binding properties of synaptic glycine receptors" Neuron 45(5): 727-39 [DOI:10.1016/j.neuron.2005.01.028]

44. Guo L., Har J.Y., Sankaran J., Hong Y.M., Kannan B., and Wohland T. (**2008**) "Molecular diffusion measurement in lipid Bilayers over wide concentration ranges: A comparative study" Chemphyschem 9(5): 721-8 [DOI:10.1002/cphc.200700611]

45. Harvey R.J., Depner U.B., Wassle H., Ahmadi S., et al. (**2004**) "GlyR alpha3: an essential target for spinal PGE2-mediated inflammatory pain sensitization" Science 304(5672): 884-7 [DOI:10.1126/science.1094925]

46. Haverkamp S., Muller U., Harvey K., Harvey R.J., Betz H., and Wassle H. (**2003**) "Diversity of glycine receptors in the mouse retina: localization of the alpha3 subunit" J. Comp. Neurol. 465(4): 524-39 [DOI:10.1002/cne.10852]

47. Hebert B., Costantino S., and Wiseman P.W. (**2005**) "Spatiotemporal image correlation spectroscopy (STICS) theory, verification, and application to protein velocity mapping in living CHO cells" Biophys. J. 88(5): 3601-14 [DOI:10.1529/biophysj.104.054874]

48. Henis Y.I., Rotblat B., and Kloog Y. (**2006**) "FRAP beam-size analysis to measure palmitoylation-dependent membrane association dynamics and microdomain partitioning of Ras proteins" Methods 40(2): 183-90 [DOI:10.1016/j.ymeth.2006.02.003]

49. Hess S.T., and Webb W.W. (**2002**) "Focal volume optics and experimental artifacts in confocal fluorescence correlation spectroscopy" Biophys. J. 83(4): 2300-17 [DOI:10.1016/S0006-3495(02)73990-8]

50. Huang Z., and Thompson N.L. (**1996**) "Imaging fluorescence correlation spectroscopy: nonuniform IgE distributions on planar membranes" Biophys. J. 70(4): 2001-7 [DOI:10.1016/S0006-3495(96)79766-7]

51. Jonkman J.E.N., and Stelzer E.H.K. (**2002**) "Resolution and Contrast in Confocal and Two-Photon Microscopy" Chap. 5 in Confocal and Two-Photon Microscopy: Foundations, Applications and Advances, A. Diaspro, Ed., pp. 101-23, Wiley-Liss, Inc., New York.

52. Kannan B., Har J.Y., Liu P., Maruyama I., Ding J.L., and Wohland T. (**2006**) "Electron multiplying charge-coupled device camera based fluorescence correlation spectroscopy" Anal. Chem. 78(10): 3444-51 [DOI:10.1021/ac0600959]

53. Kannan B., Guo L., Sudhaharan T., Ahmed S., Maruyama I., and Wohland T. (**2007**) "Spatially resolved total internal reflection fluorescence correlation microscopy using an electron multiplying charge-coupled device camera" Anal. Chem. 79(12): 4463-70 [DOI:10.1021/ac0624546]

54. Kask P., Günther R., and Axhausen P. (**1997**) "Statistical accuracy in fluorescence fluctuation experiments" Eur. Biophys. J. 25(3): 163-9 [DOI:10.1007/s002490050028]

55. Kim E.Y., Schrader N., Smolinsky B., Bedet C., et al. (**2006**) "Deciphering the structural framework of glycine receptor anchoring by gephyrin" EMBO J. 25(6): 1385-95 [DOI:10.1038/sj.emboj.7601029]

56. Kirsch J., Langosch D., Prior P., Littauer U.Z., Schmitt B., and Betz H. (**1991**) "The 93-kDa glycine receptor-associated protein binds to tubulin" J. Biol. Chem. 266(33): 22242-5

57. Kistler J., Stroud R.M., Klymkowsky M.W., Lalancette R.A., and Fairclough R.H. (**1982**) "Structure and function of an acetylcholine receptor" Biophys. J. 37(1): 371-83 [DOI:10.1016/S0006-3495(82)84685-7]

58. Kneussel M., and Betz H. (**2000**) "Receptors, gephyrin and gephyrin-associated proteins: novel insights into the assembly of inhibitory postsynaptic membrane specializations" J. Physiol. (Lond.) 525 Pt 1: 1-9 [DOI:10.1111/j.1469-7793.2000.t01-4-00001.x £££].

59. Kolin D.L., Costantino S., and Wiseman P.W. (**2006**) "Sampling effects, noise, and photobleaching in temporal image correlation spectroscopy" Biophys. J. 90(2): 628-39 [DOI:10.1529/biophysj.105.072322]

60. Kolin D.L., Ronis D., and Wiseman P.W. (**2006**) "k-Space image correlation spectroscopy: a method for accurate transport measurements independent of fluorophore photophysics" Biophys. J. 91(8): 3061-75 [DOI:10.1529/biophysj.106.082768]

61. Kolin D.L., and Wiseman P.W. (**2007**) "Advances in image correlation spectroscopy: measuring number densities, aggregation states, and dynamics of fluorescently labeled macromolecules in cells" Cell Biochem. Biophys. 49(3): 141-64 [DOI:10.1007/s12013-007-9000-5]

62. Koppel D.E. (**1974**) "Statistical Accuracy in Fluorescence Correlation Spectroscopy" Phys Rev A 10(6): 1938-45 [DOI:10.1103/PhysRevA.10.1938]

63. Koppel D.E., Morgan F., Cowan A.E., and Carson J.H. (**1994**) "Scanning concentration correlation spectroscopy using the confocal laser microscope" Biophys. J. 66(2 Pt 1): 502-7 [DOI:10.1016/S0006-3495(94)80801-X]

64. Kubitscheck U., Wedekind P., and Peters R. (**1994**) "Lateral diffusion measurement at high spatial resolution by scanning microphotolysis in a confocal microscope" Biophys. J. 67(3): 948-56 [DOI:10.1016/S0006-3495(94)80596-X]

65. Kubitscheck U., Wedekind P., and Peters R. (**1998**) "Three-dimensional diffusion measurements by scanning microphotolysis" J. Microsc. 192(2): 126-38 [DOI:10.1046/j.1365-2818.1998.00406.x]

66. Kuhse J., Schmieden V., and Betz H. (**1990**) "Identification and functional expression of a novel ligand binding subunit of the inhibitory glycine receptor" J. Biol. Chem. 265(36): 22317-20

67. Kuhse J., Laube B., Magalei D., and Betz H. (**1993**) "Assembly of the inhibitory glycine receptor: identification of amino acid sequence motifs governing subunit stoichiometry" Neuron 11(6): 1049-56 [DOI:10.1016/0896-6273(93)90218-G]

68. Kungel M., and Friauf E. (**1997**) "Physiology and pharmacology of native glycine receptors in developing rat auditory brainstem neurons" Brain Res. Dev. Brain Res. 102(2): 157-65 [DOI:10.1016/S0165-3806(97)00087-4]

69. Langosch D., Thomas L., and Betz H. (**1988**) "Conserved quaternary structure of ligand-gated ion channels: the postsynaptic glycine receptor is a pentamer" Proc. Natl. Acad. Sci. U. S. A. 85(19): 7394-8 [DOI:10.1073/pnas.85.19.7394]

70. Legendre P., Muller E., Badiu C.I., Meier J., Vannier C., and Triller A. (**2002**) "Desensitization of homomeric alpha1 glycine receptor increases with receptor density" Mol. Pharmacol. 62(4): 817-27 [DOI:10.1124/mol.62.4.817]

71. Levi S., Schweizer C., Bannai H., Pascual O., Charrier C., and Triller A. (**2008**) "Homeostatic regulation of synaptic GlyR numbers driven by lateral diffusion" Neuron 59(2): 261-73 [DOI:10.1016/j.neuron.2008.05.030]

72. Lopez A., Dupou L., Altibelli A., Trotard J., and Tocanne J.F. (**1988**) "Fluorescence recovery after photobleaching (FRAP) experiments under conditions of uniform disk illumination. Critical comparison of analytical solutions, and a new mathematical method for calculation of diffusion coefficient D" Biophys. J. 53(6): 963-70 [DOI:10.1016/S0006-3495(88)83177-1]

73. Loren N., Nyden M., and Hermansson A.M. (**2009**) "Determination of local diffusion properties in heterogeneous biomaterials" Adv. Colloid Interface Sci. 150(1): 5-15 [DOI:10.1016/j.cis.2009.05.004]

74. Lynch J.W. (**2004**) "Molecular structure and function of the glycine receptor chloride channel" Physiol. Rev. 84(4): 1051-95 [DOI:10.1152/physrev.00042.2003]

75. Lynch J.W. (**2009**) "Native glycine receptor subtypes and their physiological roles" Neuropharmacology 56(1): 303-9 [DOI:10.1016/j.neuropharm.2008.07.034]

76. Magde D., Webb W.W., and Elson E.L. (**1978**) "Fluorescence Correlation Spectroscopy .3. Uniform Translation and Laminar-Flow" Biopolymers 17(2): 361-76 [DOI:10.1002/bip.1978.360170208]

77. Malosio M.L., Marqueze-Pouey B., Kuhse J., and Betz H. (**1991**) "Widespread expression of glycine receptor subunit mRNAs in the adult and developing rat brain" EMBO J. 10(9): 2401-9

78. Mangin J.M., Guyon A., Eugene D., Paupardin-Tritsch D., and Legendre P. (**2002**) "Functional glycine receptor maturation in the absence of glycinergic input in dopaminergic neurones of the rat substantia nigra" J. Physiol. (Lond.) 542(Pt 3): 685-97 [DOI:10.1113/jphysiol.2002.018978]

79. Matzenbach B., Maulet Y., Sefton L., Courtier B., et al. (**1994**) "Structural analysis of mouse glycine receptor alpha subunit genes. Identification and chromosomal localization of a novel variant" J. Biol. Chem. 269(4): 2607-12

80. Mazza D., Cella F., Vicidomini G., Krol S., and Diaspro A. (**2007**) "Role of three-dimensional bleach distribution in confocal and two-photon fluorescence recovery after photobleaching experiments" Appl. Opt. 46(30): 7401-11 [DOI:10.1364/AO.46.007401]

81. Meier J., Vannier C., Serge A., Triller A., and Choquet D. (**2001**) "Fast and reversible trapping of surface glycine receptors by gephyrin" Nat. Neurosci. 4(3): 253-60 [DOI:10.1038/85099]

82. Meseth U., Wohland T., Rigler R., and Vogel H. (**1999**) "Resolution of fluorescence correlation measurements" Biophys. J. 76(3): 1619-31 [DOI:10.1016/S0006-3495(99)77321-2]

83. Meyer G., Kirsch J., Betz H., and Langosch D. (**1995**) "Identification of a gephyrin binding motif on the glycine receptor beta subunit" Neuron 15(3): 563-72 [DOI:10.1016/0896-6273(95)90145-0]

84. Meyvis T.K., De Smedt S.C., Van Oostveldt P., and Demeester J. (**1999**) "Fluorescence recovery after photobleaching: a versatile tool for mobility and interaction measurements in pharmaceutical research" Pharm. Res. 16(8): 1153-62 [DOI:10.1023/A:1011924909138]

85. Milon S., Hovius R., Vogel H., and Wohland T. (**2003**) "Factors influencing fluorescence correlation spectroscopy measurements on membranes: simulations and experiments" Chem. Phys. 288(2-3): 171-86 [DOI:10.1016/s0301-0104(03)00018-1]

86. Moens P.D., Gratton E., and Salvemini I.L. (**2010**) "Fluorescence correlation spectroscopy, raster image correlation spectroscopy, and number and brightness on a commercial confocal laser scanning microscope with analog detectors (Nikon C1)" Microsc. Res. Tech. [DOI:10.1002/jemt.20919]

87. Nikolic Z., Laube B., Weber R.G., Lichter P., et al. (**1998**) "The human glycine receptor subunit alpha3. Glra3 gene structure, chromosomal localization, and functional characterization of alternative transcripts" J. Biol. Chem. 273(31): 19708-14 [DOI:10.1074/jbc.273.31.19708]

88. Oertel J., Villmann C., Kettenmann H., Kirchhoff F., and Becker C.M. (**2007**) "A novel glycine receptor beta subunit splice variant predicts an unorthodox transmembrane topology. Assembly into heteromeric receptor complexes" J. Biol. Chem. 282(5): 2798-807 [DOI:10.1074/jbc.M608941200]

89. Orfanidis S.J. (**2007**) "Random Signals" Chap. 1 in Optimum Signal Processing. An Introduction, pp. 1-71, Prentice-Hall, Englewood Cliffs, NJ.

90. Peters R., Peters J., Tews K.H., and Bahr W. (**1974**) "A microfluorimetric study of translational diffusion in erythrocyte membranes" Biochim. Biophys. Acta 367(3): 282-94 [DOI:10.1016/0005-2736(74)90085-6]

91. Peters R., and Kubitscheck U. (**1999**) "Scanning microphotolysis: three-dimensional diffusion measurement and optical single-transporter recording" Methods 18(4): 508-17 [DOI:10.1006/meth.1999.0819]

92. Petersen N.O. (**1986**) "Scanning fluorescence correlation spectroscopy. I. Theory and simulation of aggregation measurements" Biophys. J. 49(4): 809-15 [DOI:10.1016/S0006-3495(86)83709-2]

93. Petersen N.O., Johnson D.C., and Schlesinger M.J. (**1986**) "Scanning fluorescence correlation spectroscopy. II. Application to virus glycoprotein aggregation" Biophys. J. 49(4): 817-20 [DOI:10.1016/S0006-3495(86)83710-9]

94. Petersen N.O., Hoddelius P.L., Wiseman P.W., Seger O., and Magnusson K.E. (**1993**) "Quantitation of membrane receptor distributions by image correlation spectroscopy: concept and application" Biophys. J. 65(3): 1135-46 [DOI:10.1016/S0006-3495(93)81173-1]

95. Petersen N.O. (**2001**) "FCS and Spatial Correlations on Biological Surfaces" Chap. 8 in Fluorescence Correlation Spectroscopy: Theory and Applications, R. Rigler and E. S. Elson, Eds., pp. 162-84, Springer-Verlag, Heidelberg.

96. Phair R.D., and Misteli T. (**2000**) "High mobility of proteins in the mammalian cell nucleus" Nature 404(6778): 604-9 [DOI:10.1038/35007077]

97. Phair R.D., Gorski S.A., and Misteli T. (**2004**) "Measurement of dynamic protein binding to chromatin in vivo, using photobleaching microscopy" Methods Enzymol. 375: 393-414

98. Poulopoulos A., Aramuni G., Meyer G., Soykan T., et al. (**2009**) "Neuroligin 2 drives postsynaptic assembly at perisomatic inhibitory synapses through gephyrin and collybistin" Neuron 63(5): 628-42 [DOI:10.1016/j.neuron.2009.08.023]

99. Pribilla I., Takagi T., Langosch D., Bormann J., and Betz H. (**1992**) "The atypical M2 segment of the beta subunit confers picrotoxinin resistance to inhibitory glycine receptor channels" EMBO J. 11(12): 4305-11

100. Qian H. (**1990**) "On the Statistics of Fluorescence Correlation Spectroscopy" Biophys. Chem. 38(1-2): 49-57 [DOI:10.1016/0301-4622(90)80039-A]

101. Reddy-Alla S., Schmitt B., Birkenfeld J., Eulenburg V., et al. (**2010**) "PH-domain-driven targeting of collybistin but not Cdc42 activation is required for synaptic gephyrin clustering" Eur. J. Neurosci. 31(7): 1173-84 [DOI:10.1111/j.1460-9568.2010.07149.x]

102. Ries J., Petrov E.P., and Schwille P. (**2008**) "Total internal reflection fluorescence correlation spectroscopy: effects of lateral diffusion and surface-generated fluorescence" Biophys. J. 95(1): 390-9 [DOI:10.1529/biophysj.107.126193]

103. Ries J., Chiantia S., and Schwille P. (**2009**) "Accurate determination of membrane dynamics with line-scan FCS" Biophys. J. 96(5): 1999-2008 [DOI:10.1016/j.bpj.2008.12.3888]

104. Rigler R., and Elson E.S., Eds. (**2001**) "Fluorescence Correlation Spectroscopy: Theory and Applications" Springer-Verlag, Heidelberg.

105. Rivera C., Voipio J., Payne J.A., Ruusuvuori E., et al. (**1999**) "The K+/Cl- co-transporter KCC2 renders GABA hyperpolarizing during neuronal maturation" Nature 397(6716): 251-5 [DOI:10.1038/16697]

106. Ruan Q., Cheng M.A., Levi M., Gratton E., and Mantulin W.W. (**2004**) "Spatial-temporal studies of membrane dynamics: scanning fluorescence correlation spectroscopy (SFCS)" Biophys. J. 87(2): 1260-7 [DOI:10.1529/biophysj.103.036483]

107. Saffarian S., and Elson E.L. (**2003**) "Statistical analysis of fluorescence correlation spectroscopy: The standard deviation and bias" Biophys. J. 84(3): 2030-42 [DOI:10.1016/S0006-3495(03)75011-5]

108. Salome L., Cazeils J.L., Lopez A., and Tocanne J.F. (**1998**) "Characterization of membrane domains by FRAP experiments at variable observation areas" Eur. Biophys. J. 27(4): 391-402 [DOI:10.1007/s002490050146]

109. Sankaran J., Manna M., Guo L., Kraut R., and Wohland T. (**2009**) "Diffusion, transport, and cell membrane organization investigated by imaging fluorescence cross-correlation spectroscopy" Biophys. J. 97(9): 2630-9 [DOI:10.1016/j.bpj.2009.08.025]

110. Sankaran J., Shi X., Ho L.Y., Stelzer E.H., and Wohland T. (**2010**) "ImFCS: a software for imaging FCS data analysis and visualization" Opt. Express 18(25): 25468-81 [DOI:10.1364/OE.18.025468]

111. Saxena R., and Chattopadhyay A. (**2011**) "Membrane organization and dynamics of the serotonin(1A) receptor in live cells" J. Neurochem. 116(5): 726-33 [DOI:10.1111/j.1471-4159.2010.07037.x]

112. Schwille P., Oehlenschlager F., and Walter N.G. (**1996**) "Quantitative hybridization kinetics of DNA probes to RNA in solution followed by diffusional fluorescence correlation analysis" Biochemistry (Mosc). 35(31): 10182-93 [DOI:10.1021/bi960517g]

113. Schwille P. (**2001**) "Cross-correlation analysis in FCS" Chap. 17 in Fluorescence Correlation Spectroscopy: Theory and Applications, R. Rigler and E. S. Elson, Eds., pp. 360-78, Springer-Verlag, Heidelberg.

114. Simon J., Wakimoto H., Fujita N., Lalande M., and Barnard E.A. (**2004**) "Analysis of the set of GABA(A) receptor genes in the human genome" J. Biol. Chem. 279(40): 41422-35 [DOI:10.1074/jbc.M401354200]

115. Sisan D.R., Arevalo R., Graves C., McAllister R., and Urbach J.S. (**2006**) "Spatially resolved fluorescence correlation spectroscopy using a spinning disk confocal microscope" Biophys. J. 91(11): 4241-52 [DOI:10.1529/biophysj.106.084251]

116. Sorscher S.M., and Klein M.P. (**1980**) "Profile of a Focused Collimated Laser-Beam near the Focal Minimum Characterized by Fluorescence Correlation Spectroscopy" Rev. Sci. Instrum. 51(1): 98-102 [DOI:10.1063/1.1136028]

117. Soumpasis D.M. (**1983**) "Theoretical analysis of fluorescence photobleaching recovery experiments" Biophys. J. 41(1): 95-7 [DOI:10.1016/S0006-3495(83)84410-5]

118. Srivastava M., and Petersen N.O. (**1996**) "Image cross-correlation spectroscopy: A new experimental biophysical approach to measurement of slow diffusion of fluorescent molecules" Methods Cell Sci. 18(1): 47-54 [DOI:10.1007/bf00123523]

119. Starchev K., Zhang J.W., and Buffle J. (**1998**) "Applications of fluorescence correlation spectroscopy - Particle size effect" J. Colloid Interface Sci. 203(1): 189-96 [DOI:10.1006/jcis.1998.5470]

120. Takahashi T., Momiyama A., Hirai K., Hishinuma F., and Akagi H. (**1992**) "Functional correlation of fetal and adult forms of glycine receptors with developmental changes in inhibitory synaptic receptor channels" Neuron 9(6): 1155-61 [DOI:10.1016/0896-6273(92)90073-M]

121. Thompson N.L. (**1991**) "Fluorescence Correlation Spectroscopy" Chap. 6 in Topics in Fluorescence Spectroscopy, J. R. Lakowicz, Ed., pp. 337-78, Plenum Press, New York.

122. Valeur B. (**2001**) "On the origin of the terms fluorescence, phosphorescence and luminescence" Chap. 1 in New trends in fluorescence spectroscopy: applications to chemical and life sciences, B. Valeur and J.-C. Brochon, Eds., pp. 3-6, Springer-Verlag, Berlin.

123. van Ooij C. (**2009**) "Nature milestones in light microscopy" Nat. Cell Biol. Supplement: S10-S1 [DOI:10.1038/ncb1932]

124. Wahl M., Gregor I., Patting M., and Enderlein J. (**2003**) "Fast calculation of fluorescence correlation data with asynchronous time-correlated single-photon counting" Opt. Express 11(26): 3583-91 [DOI:10.1364/OE.11.003583]

125. Wang M.D., and Axelrod D. (**1994**) "Microclustering patterns of acetylcholine receptors on myotubes studied by spatial fluorescence autocorrelation" Bioimaging 2(1): 22-35 [DOI:10.1002/1361-6374(199403)2:1<22::aid-bio2>3.0.co;2-3]

126. Watanabe E., and Akagi H. (**1995**) "Distribution patterns of mRNAs encoding glycine receptor channels in the developing rat spinal cord" Neurosci. Res. 23(4): 377-82 [DOI:10.1016/0168-0102(95)00972-V]

127. Webb T.I., and Lynch J.W. (**2007**) "Molecular pharmacology of the glycine receptor chloride channel" Curr. Pharm. Des. 13(23): 2350-67

128. Webb W.W. (**2001**) "Fluorescence Correlation Spectroscopy: Genesis, Evolution, Maturation and Prognosis" Chap. 14 in Fluorescence Correlation Spectroscopy: Theory and Applications, R. Rigler and E. S. Elson, Eds., pp. 305-30, Springer-Verlag, Heidelberg.

129. Wedekind P., Kubitscheck U., and Peters R. (**1994**) "Scanning microphotolysis: a new photobleaching technique based on fast intensity modulation of a scanned laser beam and confocal imaging" J. Microsc. 176(Pt 1): 23-33

130. Weissman M., Schindler H., and Feher G. (**1976**) "Determination of molecular weights by fluctuation spectroscopy: application to DNA" Proc. Natl. Acad. Sci. U. S. A. 73(8): 2776-80

131. Weissman M.B., Schindler H., and Feher G. (**1976**) "DNA molecular weight measurement by fluctuation spectroscopy" Biophys. J. 16(2): 67a

132. Weissman M.B. (**1981**) "Fluctuation Spectroscopy" Annu. Rev. Phys. Chem. 32: 205-32 [DOI:10.1146/annurev.pc.32.100181.001225]

133. Wiseman P.W., and Petersen N.O. (**1999**) "Image correlation spectroscopy. II. Optimization for ultrasensitive detection of preexisting platelet-derived growth factor-beta receptor oligomers on intact cells" Biophys. J. 76(2): 963-77 [DOI:10.1016/S0006-3495(99)77260-7]

134. Wiseman P.W., Squier J.A., Ellisman M.H., and Wilson K.R. (**2000**) "Two-photon image correlation spectroscopy and image cross-correlation spectroscopy" J. Microsc. 200(Pt 1): 14-25 [DOI:10.1046/j.1365-2818.2000.00736.x]

135. Wiseman P.W., Brown C.M., Webb D.J., Hebert B., et al. (**2004**) "Spatial mapping of integrin interactions and dynamics during cell migration by image correlation microscopy" J. Cell Sci. 117(Pt 23): 5521-34 [DOI:10.1242/jcs.01416]

136. Wohland T., Rigler R., and Vogel H. (**2001**) "The standard deviation in fluorescence correlation spectroscopy" Biophys. J. 80(6): 2987-99 [DOI:10.1016/S0006-3495(01)76264-9]

137. Wolf A.V., Brown M.G., and Prentiss P.G. (**1979-1980**) "Concentrative properties of aqueous solutions: conversion tables" in CRC Handbook of Chemistry and Physics, R. C. Weast, Ed., pp. 227-76, CRC Press, Inc., Boca Raton, Florida.

138. Young H.D., and Freedman R.A. (**2008**) "Electromagnetic waves" Chap. 32 in University Physics, pp. 1092-120, Pearson Addison-Wesley, San Fransisco.

139. Young H.D., and Freedman R.A. (**2008**) "The nature and propagation of light" Chap. 33 in University Physics, pp. 1121-56, Pearson Addison-Wesley, San Fransisco.

140. Zagyansky Y., and Edidin M. (**1976**) "Lateral diffusion of concanavalin A receptors in the plasma membrane of mouse fibroblasts" Biochim. Biophys. Acta 433(1): 209-14 [DOI:10.1016/0005-2736(76)90188-7]

141. Zhang B., Zerubia J., and Olivo-Marin J.C. (**2007**) "Gaussian approximations of fluorescence microscope point-spread function models" Appl. Opt. 46(10): 1819-29 [DOI:10.1364/AO.46.001819]

Curriculum vitae

Nick Smisdom was born on the 27th of August 1984 in Leuven, Belgium. After finishing his secondary grade education (Mathematics-Sciences) at the Sint-Tarcisiuscollege in Zoutleeuw in 2002, he started his Bachelor studies in Biomedical Sciences at the transnational University Limburg (tUL, collaboration between University of Hasselt and University of Maastricht) in Diepenbeek. In July 2005, he obtained the degree of Bachelor in Biomedical Sciences with high distinction (*Grote onderscheiding)*. The year after, July 2006, he obtained the degree of Master in Biomedical Sciences, option Bio-electronics and nanotechnology, with highest distinction (*Grootste onderscheiding met gelukwensen van de jury*).

In september 2006, he joined the group of Cell Physiology of the Biomedisch onderzoeksinstituut (BIOMED) at the University of Hasselt and tUL. At the end of 2006, he successfully applied for a PhD grant from the Institute for the Promotion of Innovation through Science and Technology in Flanders (IWT-Vlaanderen), which he started in January 2007 and ended in December 2010.

Publications in international journals

Boens N., Qin W., Baruah M., De Borggraeve W.M., Filarowski A., **Smisdom N.**, Ameloot M., Crovetto L., Talavera E. M., Alvarez-Pez J. M. (**2011**) "*Rational Design, Synthesis, Spectroscopic and Photophysical Properties of a Visible Light Excitable, Ratiometric, Fluorescent Near-Neutral pH Indicator Based on BODIPY*" Chem. Eur. J. *accepted* [DOI:*10.1002/chem.201002280*]

Smisdom N., Braeckmans K., Deschout H., vandeVen M., Rigo J.-M., De Smedt S.C., and Ameloot M. (**2011**) "*Fluorescence recovery after photobleaching on the confocal laser-scanning microscope: generalized model without restriction on the size of the photobleached disk*" J. Biomed. Opt. 16(4): 046021-8 [DOI:*10.1117/1.3569620*].

Valev V.K., Silhanek A.V., **Smisdom N.**, De Clercq B.*,* Gillijns W., Aktsipetrov O. A., Ameloot M., Moshchalkov V. V., Verbiest T. (**2010**) "*Linearly polarized second harmonic generation microscopy reveals chirality*" Opt. Express 18(*8*): 8286-93 [DOI:*10.1364/OE.18.008286*].

Smisdom N., Smets I., Williams O.A., Daenen M., Wenmackers S., Haenen K., Nesladek M., D'Haen J., Wagner P., Rigo J. M., Ameloot M., and vandeVen M. (**2009**) "*Chinese hamster ovary cell viability on hydrogen and oxygen terminated nano- and microcrystalline diamond surfaces*" Phys. Status. Solidi. A 206(9): 2042-7 [DOI:*10.1002/pssa.200982206*].

Gielen E.*, **Smisdom N.***, vandeVen M., De Clercq B., Gratton E., Digman M., Rigo J.-M., Hofkens J., Engelborghs Y., Ameloot, M. (**2009**) "*Measuring Diffusion of Lipid-like Probes in Artificial and Natural Membranes by Raster Image Correlation Spectroscopy (RICS): Use of a Commercial Laser-Scanning Microscope with Analog Detection*" Langmuir 25(9): 5209-18 [DOI:*10.1021/La8040538*]. * contributed equally to this paper

Valev V.K., **Smisdom N.**, Silhanek A.V., De Clercq B., Gillijns W., Ameloot M., Moshchalkov V. V., Verbiest T. (**2009**) "*Plasmonic Ratchet Wheels: Switching Circular Dichroism by Arranging Chiral Nanostructures*" Nano Lett. 9(*11*): 3945-8 [*DOI:10.1021/Nl9021623*].

Gielen E.*, **Smisdom N.***, De Clercq B., Vandeven M., Gijsbers R., Debyser Z., Rigo J. M., Hofkens J., Engelborghs Y., and Ameloot M. (**2008**) "*Diffusion of myelin oligodendrocyte glycoprotein in living OLN-93 cells investigated by raster-scanning image correlation spectroscopy (RICS)*" J. Fluoresc. 18(5): 813-9 [DOI:*10.1007/s10895-007-0308-8*]. * contributed equally to this paper

Published abstracts

vandeVen M., Gielen E., De Clercq B., **Smisdom N.**, Gijsbers R., Debyser Z., Engelborghs Y., and Ameloot M. (**2008**) "*One-photon raster image correlation spectroscopy (RICS) on model systems and living oligodendrocytes*" Biophys. J. 94:838

Gielen E., vandeVen M., De Clercq B., **Smisdom N.**, Engelborghs Y. and Ameloot M. (**2007**) "*Cell membrane dynamics revealed by raster-scanning image correlation spectroscopy (RICS)*" Eur. Bophys. J. 36(S1): S140

vandeVen M., Gielen E., **Smisdom N**., Gijsbers R., Debyser Z., Engelborghs Y., and Ameloot M. (**2007**) "*Diffusion of eGFP labeled protein in oligodendroglial cells*" Biophys. J. 92(1): 324A

Poster presentations (first author posters)

FRAP on the Confocal Laser Scanning Microscope: a Generalized Model without Restriction on the Size of the Photobleached Disk.
Advanced light microscopy symposium
September 23-24, **2010**, Gent, Belgium

Diffusion of membrane proteins investigated by fluorescence recovery after photobleaching on a laser scanning confocal microscope.
Belgian Physical Society meeting
May 25, **2007**, Antwerpen, Belgium

Probing the lateral membrane heterogeneity of oligodendrocytes through diffusion measurements of the myelin-oligodendrocyte glycoprotein
Belgian Society for Neuroscience bi-annual meeting
May 7, **2007**, Antwerpen, Belgium

Oral presentations

Diffusion and aggregation state of glycine receptor α_3 splice variants probed using ensemble microfluorimetric methods and MAC-TREC AFM
2nd Belgian Biophysical Society Young Scientist Day
May 31, **2011**, Gent, Belgium

Appendix

TICS Simulation

The simulation process starts with the definition of the virtual simulation space. The minimal dimensions of this virtual space, expressed in µm, are set by the desired image resolution multiplied by the pixel size and increased by the size of the point spread function filter kernel on each side. The latter is defined as 12 times the user defined e^{-2} radius of the Gaussian beam. The maximal dimensions of the virtual space depend on the required particle density and the available memory. In practice, the simulation space dimensions are often defined as five times the original image dimensions to reduce boundary effects.

Once the dimensions of the simulation space are set, the particles are randomly seeded at the specified density within the space. This is achieved by multiplying for each particle and each dimension a pseudorandom number drawn from the standard uniform distribution on the open interval]0,1[with the total length of the dimension. Throughout the simulation, their coordinates are stored as floating-point double-precision numbers.

Each particle created during the seeding operation also receives a number representing the amount of labels it bears. This degree of labeling can be a constant number throughout the population or it can be a random number drawn from a Poisson distribution with the population-average degree of labeling as mean. The number of labels is stored as uint8, which is sufficient for both cases as long as the average degree of labeling does not exceed 180. The brightness of each particle can subsequently be obtained as the product of the number of labels times the brightness of a single label.

Particles were bleached by reducing their number of labels. Since one particle can hold several labels, each label was considered as an entity, i.e. each label has a chance of being bleached irrespective of the other labels attached to the same particle. The bleach process itself can be executed in two ways: either a uniform bleach throughout the population of the labels or a bleaching based on their particle's position in the simulation box. If one or several labels from a particle are bleached, its corresponding number of labels is reduced by this amount. For the bleaching based on position, the illuminated view is considered to be the bounding circle of the image extended by 1.5 times the PSF kernel.

From the simulated particles, images are generated by first determining the pixel to which the particle belongs. Secondly, the sub-pixel localization within each pixel is determined. The precision of this localization depends on the oversampling rate of the regular pixel. For a pixel size of 80 nm, the oversampling rate is 160, meaning that the precision is 0.5 nm. Next, a look-up table is used that holds for each sub-pixel localization the corresponding values of the pixel in which the particle is located, and its surrounding pixels (*Figure 1*). These values are added to the general image, leading to the final image after all particles are processed.

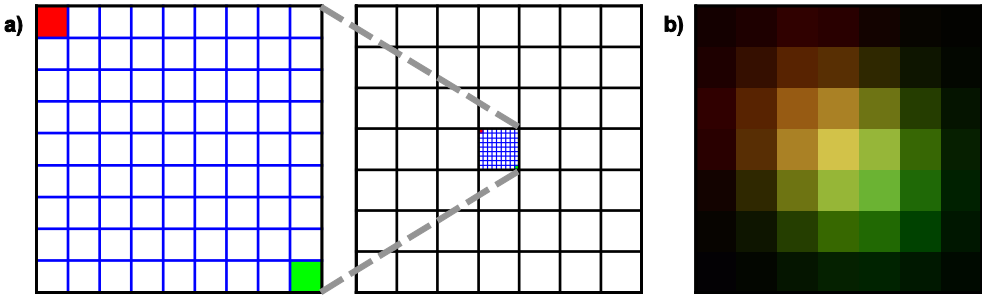

Figure 1: demonstration of the localization precision

Two particles located each in an opposing corner of a pixel are indicated in red and green (a). Their resulting image (b) clearly demonstrates that their point spread functions are not just superimposed but that their sub-pixel localization is brought into account.

Dankwoord

Bijna negen jaar geleden ben ik gestart met mijn studies Biomedische wetenschappen aan het toen nog Limburgs Universitair Centrum (LUC). De tocht begon een beetje onwennig: voor het eerst de vertrouwde piste verlaten en zonder gangmaker me een weg banen in die nieuwe, grote wereld. Gelukkig vond ik een peloton vol sfeer en vriendschap, met af een toe een duwtje in de rug en altijd wel iemand in de buurt om een lekke band te herstellen. Het gezellig keuvelen moest helaas af en toe plaats maken voor individuele tijdritten, die vaak in groep werden voorbereid met de bib als uitvalsbasis. Deze inspanningen werden achteraf ruimschoots gecompenseerd met ontspannende activiteiten. Zo passeerden de eerste twee seizoenen.

In mijn derde seizoen als student kreeg ik onder andere de col *microfluorescentie* voorgeschoteld. Alsof het een voorteken was schakelde ik nog een tand groter, om nog sneller kennis te vergaren… En ook omdat ik even voordien mijn fietsje ingeruild had voor een tandem. Met z'n tweetjes nog sneller door de studies laveren.

Uiteindelijk ben ik na vier seizoenen mogen beginnen in een hogere klasse: die van de doctoraatstudenten. Weg met de steunwieltjes, weg met de bewegwijzering, en vooral, weg met de mooi geasfalteerde weg. Van dan af ging het *off road*, met een onbekende bestemming maar ook met een hoop goede raad en ondersteuning. Die laatste zijn absoluut onmisbaar, want bij het verlaten van de vertrouwde wereld met al zijn zekerheden begonnen de *single tracks* met verraderlijke hindernissen. En daarna kwamen nog onbereden wegen: een doolhof van nauwe paadjes, vaak doodlopend en zelden goed berijdbaar. Hier kunnen zelfs de ervaren gidsen het noorden verliezen. Maar deze moeilijkheden en zware inspanning waren snel vergeten wanneer nieuwe wegen en plaatsen ontdekt werden, wanneer de weg voor achtervolgers was geëffend of toch tenminste was bewegwijzerd, en wanneer er gerust kon worden aan een plaatselijk café.

Ik heb dan ook een hele rist mensen te bedanken, van gidsen, over ploegmaats tot toevallige passanten. Allemaal hebben ze bijgedragen tot het welslagen van dit avontuur.

Marcel, hartelijk bedankt voor de begeleiding gedurende het lange avontuur: voor de aanmoedigingen wanneer het iets minder ging en het intomen wanneer ik op mijn adem dreigde te trappen. Je hebt me daarbij ook voldoende speelruimte gegeven om problemen zelfstandig (proberen) op te lossen. Ik zal ook trachten om in de toekomst het aantal beduidende tanden op de tandwielen correct weer te geven.

Jean-Michel, ook jij verdient een medaille. Terwijl Marcel zorgde voor een correcte techniek heb jij mee de weg uitgestippeld. Ik kon altijd op jou een beroep doen wanneer ik op een doodlopend spoor zat. Ik zal ook nooit je lessen over elektrofysiologie vergeten. Ze hebben me in staat gesteld om de elektrofysiologische kant van de glycine receptor te interpreteren en te waarderen.

Ik zou ook graag de jury willen bedanken voor het lezen en becommentariëren van mijn proefschrift.

Martin, jou ben ik ook veel dankbaarheid verschuldigd. In de eerste helft van mijn thesis heb je me van zeer nabij begeleid. Je hebt me gestimuleerd om zelf wat te proberen in imageJ en MATLAB, en dat heeft me achteraf geen windeieren gelegd. Maar ik wil je zeker ook bedanken voor de talrijke gesprekken van niet-wetenschappelijke aard.

Ellen, jouw enthousiasme voor het onderzoek gecombineerd met een grote dosis optimisme en chocolade werkten aanstekelijk. Ik was heel blij dat we samen naar de 1ste LFD workshop konden gaan, want als groentje was dat toch wel een grote stap (zowel letterlijk als figuurlijk). Ook bij jou kon ik terecht met problemen van allerlei aard en ik ben er zeker van je een aanwinst bent voor om het even welk team.

Ben, jij hebt de basis gelegd voor onze huidige RICS capaciteiten en dat verdient een pluim. Je bent ook altijd bereid moeilijke materie in klare taal uit te leggen en dat is essentieel voor een interdisciplinaire groep. Ik wens je heel veel succes toe met het verdere verloop van je doctoraat.

I also would like to thank Prof. Dr. Jochen Meier for kindly providing the required plasmids of the glycine receptor.

Ook zou ik graag prof. dr. Kevin Braeckmans willen bedanken. Onze samenwerking heeft me heel veel bijgebracht over FRAP. Prof. dr. Johan Hofkens en drs. Susana Rocha verdienen ook een woord van dank voor het beschikbaar stellen van een setup.

Kristof, jij zet de zaak verder en ik zie dat je dat goed doet. De weg is nog lang, maar je hebt ook nog een zee van tijd. En verder: *great minds think alike* ;-)

Daniel, jou wil bedanken om de patch-clamp metingen voor jou rekening te nemen.

Mijn (ex)bureaugenoten (voor zover ik ze nog niet allemaal vernoemd heb) wil ik ook bedanken voor de goede sfeer: Sheen, Katherine, Inge en Sarah

Ann, jou zal ik ook nooit vergeten. Ik herinner me nog hoe je mijn kraag hebt goed gelegd vlak voordat ik voor de IWT jury moest verschijnen. Het is een gouden actie gebleken.

En dan wil ik ook nog iedereen bedanken die rechtstreeks of onrechtstreeks heeft bijgedragen aan dit werk waaronder de oude garde (Sarah, Sandy, Koen, Jimmy en Roeland) en de nieuwe garde (Rik, Miha, Ariel, Nina, Quirine, Valerie en Ambily). Maar zeker ook het technisch personeel (Jo, Rosette, Patrick, Roland), prof. Paul Steel, prof. Emmy van Kerkhove, dr. Ilse Smets en waarschijnlijk nog een hele lijst.

Tot slot wil ik mijn familie bedanken. Mama, zus, nonkels en tantes, Elke, schoonbroers in spe, Gerda en Eddy: allemaal hartelijk bedankt voor de ondersteuning voor en tijdens mijn doctoraat. En natuurlijk wil ik ook iemand bedanken die een bijzondere plaats heeft in mijn hart. Iemand die mijn leven verrijkt heeft en me een schat van een dochter heeft bezorgt. Joke, ondanks de voorbije maanden als quasi alleenstaande moeder heb je het huishouden draaiende gehouden en Elise alle aandacht gegeven die ze nodig heeft. Ik ben er zeker van dat we met broertje op komst nog meer naar elkaar zullen toegroeien.

Hartelijk dank,

Nick

De transnationale Universiteit Limburg is een uniek samenwerkingsverband van twee universiteiten uit twee landen: de Universiteit Hasselt en Maastricht University.
De opleidingen informatica/kennistechnologie, statistiek en biomedische wetenschappen/moleculaire levenswetenschappen zijn reeds ondergebracht in dit samenwerkingsverband. De bacheloropleiding in de rechten is een gezamenlijk initiatief van de Universiteit Hasselt, Maastricht University en de K.U.Leuven. Ook in andere wetenschapsdomeinen wordt gezocht naar samenwerking met andere universiteiten.

www.unimaas.nl

Universiteit Maastricht
Postbus 616
NL-6200 MD Maastricht
Tel. 0031(0)43 388 222

www.uhasselt.be

Universiteit Hasselt | Campus Diepenbeek
Agoralaan | Gebouw D
BE-3590 Diepenbeek | België
Tel.: +32(0)11 26 81 11